MONTE CARLO SIMULATION OF STRUCTURAL AND MECHANICAL PROPERTIES OF CRYSTAL AND BICRYSTAL SYSTEMS AT FINITE TEMPERATURE

by

Reza Najafabadi Farahani

S.B., Sharif University of Technology, Iran
(1975)

S.M., Massachusetts Institute of Technology
(1980)

Nucl.Eng., Massachusetts Institute of Technology
(1980)

Submitted to the Department of
Nuclear Engineering
in Partial Fulfillment of the
Requirements of the
Degree of

DOCTOR OF PHILOSOPHY

at the

MASSACHUSETTS INSTITUTE OF TECHNOLOGY
January 1983

Signature of Author _____
Department of Nuclear Engineering, January 1983

Certified by _____
Thesis Supervisor

Accepted by _____
Chairman, Departmental Committee on Graduate Students

MONTE CARLO SIMULATION OF STRUCTURAL AND MECHANICAL PROPERTIES OF CRYSTAL AND BICRYSTAL SYSTEMS AT FINITE TEMPERATURE

by

Reza Najafabadi Farahani

Submitted to the Department of Nuclear Engineering

on January 24, 1983 in partial fulfillment of the

requirements for the degree of Doctor of Philosophy in

Nuclear Engineering

ABSTRACT

The Monte Carlo Simulation technique has been improved so that it can be used to simulate a system of a finite number of particles at thermal and mechanical equilibrium with its surroundings. The technique has been used to study structural and mechanical properties of argon and iron crystals, and also a two dimensional bicrystal with Lennard Jones interatomic potential. The behavior of impurity atoms and vacancies in the two dimensional bicrystal have been explored using the improved technique.

The martensitic transformations (bcc→fcc) and (fcc→bcc) under tension and compression at the temperature of 70°K, through the non-classical path, have been observed using a 32 particle system with Johnson I interatomic potential. The critical stresses at which the transformations occur are less than the values calculated by static method because of the thermal motion of particles. Johnson I potential overestimates the lattice constant in the fcc phase by 4.2% when the transformation takes place.

The static calculations of theoretical tensile strengths of α-iron, using Morse and Johnson I potential are $1.2*10^{10}$ and $9*10^{10}$ dyn/cm^2 respectively. These results reveal that Johnson I is a more realistic potential to be used to simulate mechanical properties of α-iron. Still the Johnson I potential does not give the theoretical strength greater than the experimental value that one would expect.

The fcc argon crystal has been studied under uniaxial loading at the temperature of 40°K (melting temperature $\sim$ 110°K) using 32 and 108 particle systems with Lennard Jones interatomic potential. The stress-strain relation is significantly different from that of static calculation (0°K) at high stresses. The temperature effects result in 12.8% decrease in C_{11} and 6.4% increase in C_{12} with respect to their values at 0°K. At the tension load of 600 bar the system fails whereas the static method prediction is 2100 bar. This discrepancy is

partly explained by the thermal motion of particles. At the compression load of 350 bar the fcc structure is transformed to an hcp structure by contraction along the load direction [001] and sliding of (010) planes.

The mechanical properties of a two dimensional bicrystal with $\Sigma=7$ has been investigated. The bicrystal is composed of 56 particles interacting through the Lennard Jones potential. The stress-strain of the bicrystal has been calculated when a load normal to the grain boundary plane is applied. the results show that the bicrystal deforms more than a single crystal with the same crystallographic orientation as one of the components of the bicrystal. Grain boundary sliding and migration has also been observed under shear loading.

The behavior study of impurity atoms in the bicrystal has shown that impurities with the size smaller than the host atom are absorbed by the grain boundary. Also it has been demonstrated that vacancies annihilate by the grain boundary.

Thesis Supervisor: Sidney Yip
Title: Professor of Nuclear Engineering

Thesis Reader: Gretchen Kalonji
Title: Assistant Professor of Materials Science and Engineering

Acknowledgements

It is a pleasure to acknowledge the understanding, guidance, encouragement, support and patience of my supervisor Professor Sidney Yip.

I would like to thank Professor Gretchen Kalonji as the reader of the thesis. I would like also to thank my colleague Jon Anderson for proofreading the thesis.

This work could not have been accomplished without the financial support provided by the Department of Nuclear Engineering and the Army Research Office in Durham, N.C. For their help I am grateful.

LIST OF FIGURES

List of Figures (cont'd)

List of Figures (cont'd)

Table of Contents

Table of Contents (cont'd)

Table of Contents (cont'd)

Chapter 1

Introduction

Computer simulation techniques are widely used to investigate properties of materials and to understand their behavior from an atomistic point of view. There are essentially two techniques that are used to simulate a system consisting of a finite number of particles at a given temperature provided that the interatomic interaction is known: the molecular dynamics method [W76] and the Monte Carlo Method [W68]. One of the limitations of these techniques was that they could be used to simulate a system under the condition of hydrostatic pressure only. Recently the molecular dynamics technique was improved [P81] such that it can be used to simulate a system under the condition of externally applied stresses. This corresponds to the study of a system in the (N, E, $\underline{\underline{S}}$) ensemble where N is the number of particles in the system, E is the total energy of the system, and $\underline{\underline{S}}$ the stress tensor applied on the system. This improvement opened up a whole new area of investigations, namely, the behavior of solids at non-zero temperature and high levels of external stress where crystal structural transformations and spontaneous defect generation become possible. Previously structural and mechanical studies were limited to absolute zero temperature using the static method [M71]. One of the objectives of this thesis was to improve the Monte Carlo technique such that it can also be used to simulate the behavior of solids at normal temperatures and high levels of external stress. The improved Monte Carlo technique simulates a system in the (N, T, $\underline{\underline{S}}$) ensemble where T is the temperature. This technique carries out the simulation isothermally whereas the improved molecular dynamics method does it adiabatically. Essentially

Monte Carlo is a method of efficiently evaluating multi-dimensional integrals in a stochastic way [W68]. In simulation studies these integrals are the ensemble averages.

Structural transformations in solids have been of interest both theoretically and experimentally [C65]. Among the structural transformations the Martensitic transformations which are common in iron, iron alloys and many other materials [B56[a]] are of special interest [081, 082]. The Martensitic transformation is a transformation in which the product structure and the parent structure can be related by a pure deformation. This transformation is believed to occur through either a classical or a non-classical path [081]. In the classical path theory a nucleus having the product structure is created whereas in a non-classical path theory the product is produced in a finite region through a continuous deformation of the parent structure. In this work, using the improved Monte Carlo technique, the martensitic transformations of iron through the non-classical path were investigated when a uniaxial stress was applied on the system. The simulations were carried out on a model system consisting of 32 particles interacting through the Johnson I potential [J64] commonly used for α iron. In these studies the flexible periodic border condition was used. This border condition allows the simulation cell to change its shape and dimensions as the simulation proceeds. Since the system used was small, investigations of the martensitic transformation through the classical path was not possible. It was found that at the temperature of 70°K the bcc iron structure transforms to the fcc structure at the critical tension load of $5.5*10^{10}$ dyn/cm^2 and the fcc structure transforms to the bcc

structure at the critical compression load of $6.0 * 10^{10}$ dyn/cm^2. These results are in general agreement with the results found using the static method. A similar study at 40°K was also carried out on a system of 32 particles interacting through the Lennard-Jones potential. The potential parameters were chosen to represent argon [H64] solid. The simulation results showed that the fcc argon structure fails at a critical tension load of 600 bar. At the critical compression load of 350 bar the fcc structure transformed to an hcp structure by a large contraction in the load direction and sliding of (010) planes. This transformation could not be predicted by the static calculations carried out on the same system because at zero temperature the sliding of the (010) planes was not possible. This transformation was also observed previously [P81] on a system model representing nickel. The isothermal elastic constants C_{11} and C_{12} were calculated from the simulated stress-strain curve. Comparing these elastic constants with those found by the static method (zero temperature) revealed that the temperature effect results in 12.8% decrease in C_{11} and 6.4% increase in C_{12}. The simulation results obtained for a 108 particle system of argon showed that the number dependence effects are insignificant.

Although most of the practical engineering material are in the form of polycrystals, it is much easier to investigate the grain boundary effects in a bicrystal [P75]. There has been relatively few simulation attempts [J70] so far to study the influence of grain boundaries on mechanical properties of a bicrystal. The experimental results [L77] show that when a bicrystal of β-brass is subjected to compressive loads along the grain boundary plane

it will deform less than the single crystal under the same conditions. It is believed [L77] that this change arises from elastic shear incompatibility [H72].

Simulations were carried out on a two dimensional coincidence site lattice grain boundary system composing of 56 particles interacting through a Lennard-Jones potential. The coupled sliding and migration of the grain boundary in this system was studied previously [B82[a], B82[b]]. Using the improved technique and flexible periodic border condition the stress-strain curve of the bicrystal was simulated when it was subjected to the compressive and tensive loads along the direction normal to the grain boundary plane. It was found that, in comparison with the stress-strain curve of the single crystal, at low temperature ($\sim \frac{1}{15}$ of melting temperature) the bicrystal deforms more than a single crystal along the compression or tension loadings. Also it was found that, at the same temperature, the grain boundary starts sliding and migration when a shear stress is applied on the bicrystals.

Although it is well known that the grain boundaries act as sources or sinks for point defects [B 79[a]], it was only recently that some attempts were made [B8 0[b], B81[b], H81] to study the structure of vacancy in several grain boundary systems employing computer simulation techniques. These studies showed that the vacancy introduced away from the boundary will lower the total energy of the systems if it is moved toward the grain boundary, but it remains at the boundary as a distinguishable missing atom in the grain boundary structure. In this thesis the behaviors of impurity and vacancy in

the above bicrystal were investigated using the improved technique and the flexible periodic border condition. It was found that impurities of a size smaller than the host atom are absorbed by the grain boundary whereas impurities with twice the size of the host atom tend to divide the system into clusters. Also it was found that the vacancies are absorbed by the grain boundary if the temperature is high enough to activate the grain boundary motion. In these simulations when the vacancy was absorbed by the grain boundary no "distinguishable missing atom" was observed.

Chapter 2

Monte Carlo Method

2.1 Introduction

Monte Carlo method is a well known technique in which, in general, many-dimensional integrals are evaluated by simply integrating over random sampling points instead of over a regular array of points as is done in finite element method. Detailed descriptions of this method are available in various reviews [B79[b], V77, W68].

Monte Carlo method has been used to study thermodynamic , structural, and even statistical properties of a sytem composed of a finite number of particles interacting through a known potential function. For example, applications have been made to solids [H70, B73], liquids [B71,B73], liquid mixture [T77[a], M72[a]], phase transitions [B81[a], T82, A80, T78, F72, H69,R74], grain boundaries [C81, C80], vacancies in solids [J80, S69[a]], surface tension [L80], magnetic systems [P80, B80[a], B76[c]], free energy calculations [N82, T77[b] , P76 , B76[b]], among others.

In Section 2 we discuss the calculation of thermodynamic properties as ensemble averages. The implementation of the Monte Carlo method is described in Section 3, and its applications to an isobar-isothermal ensemble are expained in Sec.4. In Section 5 the Monte Carlo technique is formulated for an "isostress-isothermal" ensemble.

2.2 Calculation of Thermodynamic Properties

Statistical mechanics provides a method of relating the thermodynamic properties of a macroscopic system to the statistical and mechanical properties of the particles which make up the microscopic system.

The microscopic state of a system, in classical physics, is

specified in terms of momenta and position coordinates of all its constituent particles. Thus a microscopic state of an M-dimensional system may be represented by the location of a point in the 2xMxN dimensional phase space (N is the number of particles) defined by MxN position coordinates and MxN momenta. From now on we use "state" to denote a microscopic state unless otherwise stated. The total energy, E, of any state of a 3-dimensional system is given by:

$$E = \sum_{i=1}^{N} \frac{1}{2m}\left[P_{xi}^2 + P_{yi}^2 + P_{zi}^2 \right] + U_T(x_1, y_1, z_1, \cdots x_N, y_N, z_N) \quad (2.1)$$

where m is the mass of a particle, P_{xi}, P_{yi}, and P_{zi} are the momenta of particle i, x_i, y_i, and z_i are the coordinates of particle i, and U_T is the total potential energy of the state.

In order to write the equations more concisely, we employ a vector notation as follows:

$$\begin{aligned} \vec{P} &= (P_{x1}, P_{y1}, P_{z1}, \ldots, P_{xN}, P_{yN}, P_{zN}) \\ \vec{r} &= (x_1, y_1, z_1, \ldots, x_N, y_N, z_N) \end{aligned} \quad (2.2)$$

and in this notation Eq. (2.1) becomes:

$$E(\vec{P}, \vec{r}) = \frac{\vec{P}^2}{2m} + U_T(\vec{r}) \quad (2.3)$$

In calculating thermodynamic properties one assumes the system being studied is in equilibrium. This requirement allows a time average (which would be used in a real measurement of a thermodynamic

variable) to be replaced by an average taken over a representative sample (generally called an ensemble) of states, which are assumed to exist concurrently. This equivalance is known as the ergodicity condition.

The average value (i.e. a macroscopically observable value) of any function, say $\phi(\vec{p}, \vec{r})$, is given by the integral that must be evaluated.

$$\langle \Phi \rangle = \int \Phi(\vec{p}, \vec{r}) f(\vec{p}, \vec{r}; \vec{x}) d\vec{r} d\vec{p} \qquad (2.4)$$

where the integral is taken over the entire phase space, and $f(\vec{p},\vec{r};\vec{x})$ is the probability density function. In other words $f(\vec{p},\vec{r};\vec{x})d\vec{p}d\vec{r}$ is the probability that, at a given instant, the state of the system is represented by a phase point lying in the elemental volume $d\vec{p}d\vec{r}$ centered on $(\vec{p},\vec{r})$. Thus

$$\int d\vec{p} d\vec{r} f(\vec{p}, \vec{r}; \vec{x}) = 1 \qquad (2.5)$$

In the above equations variables x are the thermodynamically independent external variables. These variables effectively restrict the integrals to be taken over a portion of the phase space. For example, they could be temperature (T), volume (V), and a number of particles (N) in the system corresponding NVT or canonical ensemble, or they could be T, N, and pressure (p) in the isobar-isothermal ensemble, or T, N, and stress tensor ($\underline{\underline{S}}$) in the "isostress -isothermal"ensemble. The probability density function $f(\vec{p},\vec{r};\vec{x})$ in general is given by Hill [H56].

In the following we will derive some of the thermodynamical properties of an isobar-isothermal ensemble for a closed system in mechanical and thermal equilibrium with its surroundings. They will be used in Chapter 3 to study thermodynamic properties of the argon crystal under constant pressure and temperature. One may easily derive the corresponding expressions for other ensembles by the appropriate $f(\vec{r},\vec{p};\ Pex;N;T)$.

The density distribution function, f, for the isobar-isothermal ensemble has the form [H56]:

$$f(\vec{r},\vec{p};P_{ex};N;T) = \text{Const.} * Exp\left\{-\frac{1}{kT}\left[E(\vec{p},\vec{r})+P_{ex}V(\vec{r})\right]\right\} \quad (2.6)$$

where Pex is the external hydrostatic pressure, not to be confused with momenta vector $\vec{p}$, V the volume of the state, and T absolute temperature of the system. The constant factor in Eq. (2.6) is the inverse of the partition function.

$$Q = \frac{1}{\text{Const.}} = \int d\vec{p}\, d\vec{r}\ Exp\left\{-\frac{1}{kT}\left[E(\vec{p},\vec{r}) + P_{ex}V(\vec{r})\right]\right\} \quad (2.7)$$

From Q all thermodynamic properties of a system can be derived; it is very difficult, except for some simple systems, to calculate this quantity. For this reason direct calculation of the property of interest is more appropriate. Some properties of interest in the present work are the following.

i) Total energy <E>

$$\langle E \rangle = \frac{1}{Q} \int d\vec{p}\, d\vec{r}\; E(\vec{p},\vec{r})\; Exp\left\{-\frac{1}{kT}\left[E(\vec{p},\vec{r}) + P_{ex} V(\vec{r})\right]\right\} \qquad (2.8)$$

since $\vec{p}$ and $\vec{r}$ are independent variables in classical systems, substituting Eq. (2.3) in Eq. (2.8) gives

$$\langle E \rangle = \frac{1}{Q_{kin.}} \int_{-\infty}^{+\infty} d\vec{p} \left[\frac{|\vec{p}|^2}{2m}\right] Exp\left[-\frac{\vec{p}^2}{2kMT}\right] + \frac{1}{Q_{conf.}} \int d\vec{r}\; U_T(\vec{r}) * \qquad (2.9)$$
$$Exp\left\{-\frac{1}{kT}\left[U_T(\vec{r}) + P_{ex} V(\vec{r})\right]\right\}$$

where (2.10)

$$Q_{kin.} = \int_{-\infty}^{+\infty} d\vec{p}\; Exp\left[-\frac{1}{kT} \cdot \frac{\vec{p}^2}{2m}\right]$$

and (2.11)

$$Q_{conf.} = \int d\vec{r}\; Exp\left\{-\frac{1}{kT}\left[U_T(\vec{r}) + P_{ex} V(\vec{r})\right]\right\}$$

It is easy to show that:

$$\frac{1}{Q_{kin.}} \int_{-\infty}^{+\infty} d\vec{p}\; \frac{|\vec{p}|^2}{2m}\; Exp\left[-\frac{1}{kT} \cdot \frac{\vec{p}^2}{2m}\right] = \frac{3N}{2} kT \qquad (2.12)$$

then

$$\langle E \rangle = \frac{3N}{2} kT + \frac{1}{Q_{conf.}} \int d\vec{r}\; U_T(\vec{r})\; Exp\left\{-\frac{1}{kT}\left[U_T(\vec{r}) + P_{ex} V(\vec{r})\right]\right\}$$

Notice that to calculate the second term in Eq. (2.12) one needs to work in a 3N dimensional phase position space, not 6N dimensional phase space.

ii) Volume <V>

Putting $V(\vec{r})$ for $\Phi(\vec{p},\vec{r})$ in Eq. (2 .4) the kinetic part cancels out and

$$\langle V \rangle = \frac{1}{Q_{conf.}} \int d\vec{r}\; V(\vec{r})\; Exp\left\{-\frac{1}{kT}\left[U_T(\vec{r}) + P_{ex} V(\vec{r})\right]\right\} \qquad (2.14)$$

iii) Internal pressure <Pin>

Using virial theorem [M25] one gets

$$\langle P_{in} \rangle = \frac{NkT}{\langle V \rangle} - \frac{1}{3\langle V \rangle} \cdot \frac{1}{Q_{conf.}} \int d\vec{r} \, \frac{\partial}{\partial |\vec{r}|} U_T(\vec{r}) * \exp\left\{ -\frac{1}{kT} [U_T(\vec{r}) + P_{ex} V(\vec{r})] \right\} \tag{2.15}$$

or in the more general case, the internal stress tensor $\langle \underline{\underline{S}}_{in} \rangle$:

$$\langle S_{in} \rangle_{ij} = \frac{NkT}{3\langle V \rangle} \cdot \delta_{ij} - \frac{1}{3\langle V \rangle} \cdot \frac{1}{Q_{conf.}} \int d\vec{r} \, \frac{\partial U_T(\vec{r})}{\partial |\vec{r}|} \cdot \frac{(\vec{r} \times \vec{r})_{ij}}{|\vec{r}|} * \exp\left\{ -\frac{1}{kT} [U_T(\vec{r}) + P_{ex} V(\vec{r})] \right\} \tag{2.16}$$

iv) Specific heat at constant pressure, c_p

$$C_p = \left. \frac{\partial \langle H \rangle}{\partial T} \right|_{P_{ex}} = \frac{3}{2} kT + \frac{1}{kT^2} \left\{ \langle U_T^2 \rangle - \langle U_T \rangle^2 \right\} + \frac{P_{ex}}{kT^2} \left\{ \langle V^2 \rangle - \langle V \rangle^2 \right\} \tag{2.17}$$

v) Isothermal compressibility, K_T

$$K_T = -\frac{1}{\langle V \rangle} \cdot \left. \frac{\partial \langle V \rangle}{\partial P_{ex}} \right|_T = -\frac{1}{\langle V \rangle} \cdot \frac{1}{kT} \left\{ \langle V^2 \rangle - \langle V \rangle^2 \right\} \tag{2.18}$$

Note that thermal bulk modulus B_T is $\frac{1}{K_T}$

vi) Thermal expansion coefficient α

$$\alpha = \frac{1}{\langle V \rangle} \cdot \left. \frac{\partial \langle V \rangle}{\partial T} \right|_{P_{ex}} = \frac{1}{\langle V \rangle^2} \cdot \frac{1}{kT^2} \left\{ P_{ex} [\langle V^2 \rangle - \langle V \rangle^2] + [\langle U_T V \rangle - \langle U_T \rangle \langle V \rangle] \right\} \tag{2.19}$$

2.3 Monte Carlo Method

The "conventional" Monte Carlo method is directly applicable to the evaluation of any integral, but it is very inefficient [M53] in evaluating the average quantity <A> of the form

$$\langle A \rangle = \frac{\int d\vec{r}\, f(\vec{r})\, A(\vec{r})}{\int d\vec{r}\, f(\vec{r})} \qquad (2.20)$$

$f(\vec{r})$ being Exp $\{-\frac{1}{T_K}[U_T(\vec{r}) + P_{ex}\, V(\vec{r})]\}$ or other density distribution functions. Here, we are not concerned with the general applications of the Monte Carlo method for which the reader is referred to the reference [C64]. Our interest lies in the special procedure developed by Metropolis et al. [M53] which is an efficient procedure, to be discussed later in this section, to calculate thermodynamic properties.

Eq. (2.20) can be considered as the expected value of the quantity $A(\vec{r})$ over the phase space with the unnormalized probability density $f(\vec{r})$. It can be written as:

$$\langle A \rangle \cong \frac{1}{n} \sum_{i=1}^{n} A(\vec{r}_i) = \bar{A} \qquad (2.21)$$

where, in the Metropolis procedure, points $\vec{r}_i$ in phase space are sampled with a probability proportional to $f(\vec{r}_i)$ so that the sampled states are pre-weighted. By contrast, in the "conventional" Monte Carlo procedure the states are sampled without any discrimination (the phase space is uniformly sampled), and then they are weighted by $f(\vec{r}_i)$. Since the weighting function $f(\vec{r})$ in ensemble averages varies from almost zero to almost infinity and most of the states in phase space have almost zero weighting function. For example, in the canonical ensemble $f(\vec{r})$ is Exp $[-\frac{1}{T_K} U_r(\vec{r})]$, where $U_T(\vec{r})$ is the total potential energy of the system and varies from a negative minimum value, say $\frac{1}{T_K} U_T(\vec{r}) \cong -800$ for a small size system of 32 particles, to zero when the particles are far apart. Then the conventional sampling procedure

will end up sampling those points in phase space which have virtually no contribution to the ensemble average most of the time.

In carrying out the Metropolis procedure a chain of states is generated such that the probability of getting to the ith state of the chain is explicitly dependent on the probability of the (i-1)th state. This type of sequence is called a Markov chain. The matrix describing the transition probabilities, p_{ij}, between all states of the system should be chosen so that the value of any function of state, averaged over all the states of the chain, tends towards the ensemble average defined in Eq. (2.20)' as the chain is extended indefinitely. The necessary and sufficient conditions [W68] for the convergence of the chain average Eq. (2.21) to the ensemble average Eq. (2. 20) are the following:

1. $$\sum_{j=1}^{n} p_{ij} = 1 \quad \text{and} \quad p_{ij} \geq 0 \quad \text{for all } i \text{ and } j \tag{2.22}$$

2. Ergodicity condition

If i and j are any two admissible states (states for which the probability of the system being in them is finite). Then for some finite k, which may depend on i and j, the k-step transition probability $p_{ij}^{(k)}$ is non-zero.

3. Steady state condition

$$\sum_{i=1}^{n} u_i p_{ij} = u_j \quad \text{for all } j \tag{2.23}$$

where u_i, the normalized probability of the system being at the state i, is given by:

$$u_i = \frac{f(\vec{r}_i)\, d\vec{r}}{\int d\vec{r}\, f(\vec{r}_i)} \tag{2.24}$$

Combining Eqs. (2.23) and (2.24) one gets

$$u_i p_{ij} = u_j p_{ji} \qquad \text{for all } i \text{ and } j \tag{2.25}$$

The desired stochastic convergence results essentially from the fact that under these conditions, the n-step transition probability $p_{ij}^{(n)} \longrightarrow u_j$ as $n \longrightarrow \infty$, and also limit theorem for Markov chain [D53] gives:

$$\lim_{n\to\infty} \mathcal{P}\left\{ \frac{1}{\sqrt{n}} \sum_{i=1}^{n} \left[A(\vec{r}_i) - \langle A \rangle \right] \leq \lambda \right\} = \frac{1}{\sigma_1 \sqrt{2\pi}} \int_{-\infty}^{\lambda} dy \exp\left(-\frac{y^2}{2\sigma_1^2}\right) \tag{2.26}$$

where P{} means the probability of the event {}. This means the realization average $\overline{A}$ given by Eq. (2.21) is asymptotically normally distributed with mean value <A> and variance $\sim \frac{\sigma_1^2}{n}$. The variance parameter in Eq. (2.26) is defined by the relation

$$\sigma_1^2 = \lim_{n\to\infty} \mathcal{E}\left\{ \frac{1}{\sqrt{n}} \sum_{i=1}^{n} \left[A(\vec{r}_i) - \langle A \rangle \right]^2 \right\} \tag{2.27}$$

in which $\mathcal{E}$ {} denotes the expectation of the quantity in the curly braces for the stochastic process in question.

In essence, then, the Monte Carlo procedure is simply to select a (p_{ij}) prescription which will satisfy the above conditions. In practice, it is essential to choose p_{ij} in such a fashion as to be non-zero only for states i and j which in some sense are near

neighbors of each other [W68].

The most commonly used prescription, often referred to as the asymmetrical procedure, is

$$p_{ij} = \begin{cases} 0 & \text{if } j \text{ not in } \eta(i) \\ \frac{1}{Z} & \text{if } j \in \eta(i) \; ; \; j \neq i \text{ and } u_j \geq u_i \\ \frac{u_j}{u_i} \cdot \frac{1}{Z} & \text{if } j \in \eta(i) \; ; \; j \neq i \text{ and } u_j < u_i \end{cases} \qquad (2.28)$$

$$p_{ii} = 1 - \sum_{i \neq j} p_{ij}$$

where $\eta(i)$ denote any specified set of Z neighbor states of state i, and Z is independent of i and also

$$\begin{aligned} & i \notin \eta(i) \\ & i \in \eta(j) \quad \text{if and only if } j \in \eta(i) \end{aligned} \qquad (2.29)$$

It is readily verified that (2.28) satisfies the necessary and sufficient conditions (1) to (3). There are other forms of (p_{ij}) [W68] which also satisfy the above conditions. Thus the path to get the ensemble averages of a system is not unique.

Notice that to carry out the Monte Carlo method with the above prescription of (p_{ij}) there is no need to know the exact values of u_i and u_j (to know them requires one to know the partition function), only u_i/u_j is required which can be evaluated easily.

In the next sections we have briefly indicated how one practically develops a realization of the Markov chain defined by Eq. (2.28) for two different ensembles.

2.4 Isobaric-Isothermal Ensemble Sampling

The unnormalized density distribution function for an isobar-isothermal ensemble was given in Eq. (2.6). To get the normalized u_i, Eq. (2.6) is substituted in Eq. (2. 14),

$$u_i = Exp\left\{-\frac{1}{kT}\left[U_T(\vec{r}) + P_{ex}V(\vec{r})\right]\right\} \Big/ \int d\vec{r}\, Exp\left\{-\frac{1}{kT}\left[U_T(\vec{r}) + P_{ex}V(\vec{r})\right]\right\}$$

$$= \frac{1}{Q_{conf.}} \cdot Exp\left\{-\frac{1}{kT}\left[U_T(\vec{r}) + P_{ex}V(\vec{r})\right]\right\} \qquad (2.30)$$

where P_{ex} is constant external hydrostatic pressure applied to the system, while the internal pressure P_{in} in Eq. (2.14) will fluctuate about P_{ex} The average of A(r) in the ensemble can be written in the form

$$\langle A\rangle = \frac{1}{Q_{conf.}} \int d\vec{r}\, A(\vec{r})\, Exp\left\{-\frac{1}{kT}\left[U_T(\vec{r}) + P_{ex}V(\vec{r})\right]\right\} \qquad (2.31)$$

where the integration $\int_{-\infty}^{+\infty} d\vec{r} = \int_{-\infty}^{+\infty} dx_1 dy_1 dz_1 \int_{-\infty}^{+\infty} \cdots \int_{-\infty}^{+\infty} dx_N dy_N dz_N$, should be carried out over the whole position space. One way to do this, in principle, is to replace the integral $\int_{-\infty}^{+\infty} d\vec{r}$ by

$$\int_0^\infty dV \int_V dx_1\, dy_1\, dz_1 \cdots \int_V dx_N\, dy_N\, dz_N \qquad (2.32)$$

So the sampling is done first in a fixed volume V, then the volume is changed and the sampling repeated till the entire space is covered. In this way the problem of defining the volume of each state is avoided, otherwise, it would be difficult to assign a volume to each point in position space in a simple way.

In practice the Markov chain is started from an initial state defined by $(V_i, \vec{r}_i)$. Then a trial state $(V,\vec{r}')$ is chosen randomly and uniformly (i.e., with equal probability $\frac{1}{Z}$ for any state which is considered a neighbor to state "i," $(V_i, \vec{r}_i)$ from the set of states $\eta(i)$. The set $\eta(i)$ consists of all those state "j" for which its V_j and the scaled coordinates of a randomly chosen particle "m" (S_x^m, S_y^m, S_z^m) lie in some interval $V_i + S_v$ and $(S_x^m \pm \delta, S_y^m \pm \delta, S_z^m \pm \delta)$ respectively, and all other particles (N-1) have the same scaled coordinates as they have in state $(V_i, \vec{r}_i)$.

The scaled coordinates refer to the coordinates of particles when the cubic volume is reduced to a unit cube. Then Eq. (2.32) may be written as:

$$\int_0^\infty dV\,[V]^N \int_{V=1} d\vec{s}_1 \cdots \int_{V=1} d\vec{s}_N \tag{2.33}$$

This conversion makes bookkeeping easier.

The trial state is chosen from the following relations:

$$\begin{aligned} V' &= V_i + \delta_V (1 - \xi_V) \\ m &= I\,[(N+1)\,\xi_m] \\ s_x'^m &= s_x^m + \delta\,(1 - \xi_x) \\ s_y'^m &= s_y^m + \delta\,(1 - \xi_y) \\ s_z'^m &= s_z^m + \delta\,(1 - \xi_z) \end{aligned} \tag{2.34}$$

where ξ_v, ξ_m, ξ_x, ξ_y, and ξ_z, denote independent random numbers uniformly distributed on the interval (0,1), δ and δ_v are parameters to

be discussed in section (2.6), and I[x] means integer part of x (particles are numbered from 1 to N). The mechanism of choosing the trial state is schematically shown in Fig. 2.1 for a 2-dimensional system. Once the trial state is chosen, the expression $h' = P_{ex} V' + U_T(\vec{r}') - N\ln(V')$ is evaluated. If $h' \leq h = P_{ex} V_i + U_T(\vec{r}_i) - N\ln(V_i)$ $(u' > u_i)$, the term $N\ln(V)$ comes from V^N in Eq. (2.33), then the new state is the trial state and the quantities of interest are evaluated for this state to be used to calculate the ensemble averages. But if $h' > h_i$ $(u' < u_i)$, then $\frac{u'}{u_i} = \text{Exp}\left[-\frac{1}{kT}(h'-h_i)\right]$ is evaluated and is compared with a random number ξ uniformly distributed on the interval (0,1). If $\frac{u'}{u_i} < \xi$ the new state is the trial state, otherwise, the trial state is rejected and the new state is the old one. The repetition of this process many times will produce the desired distribution of states [M53].

Note that the volume of the system at any state is the uniform expansion or contraction of the initial volume. This constraint on the system volume corresponds to subjecting the system to a particular value of hydrostatic pressure, and it will be used in Chapter 3. The constraint will be removed for the constant stress ensemble discussed in the next section. One may revise the above prescription in such a way that for a given volume a fixed number of trials should be made, equal to N the number of particles, for example. This means that once a state with a new volume is reached, in the next N trials the volume is to be kept constant. This will reduce the computational time because to calculate the total potential $U_T(\vec{r})$, which is the most time consuming part of the program, the program calculates

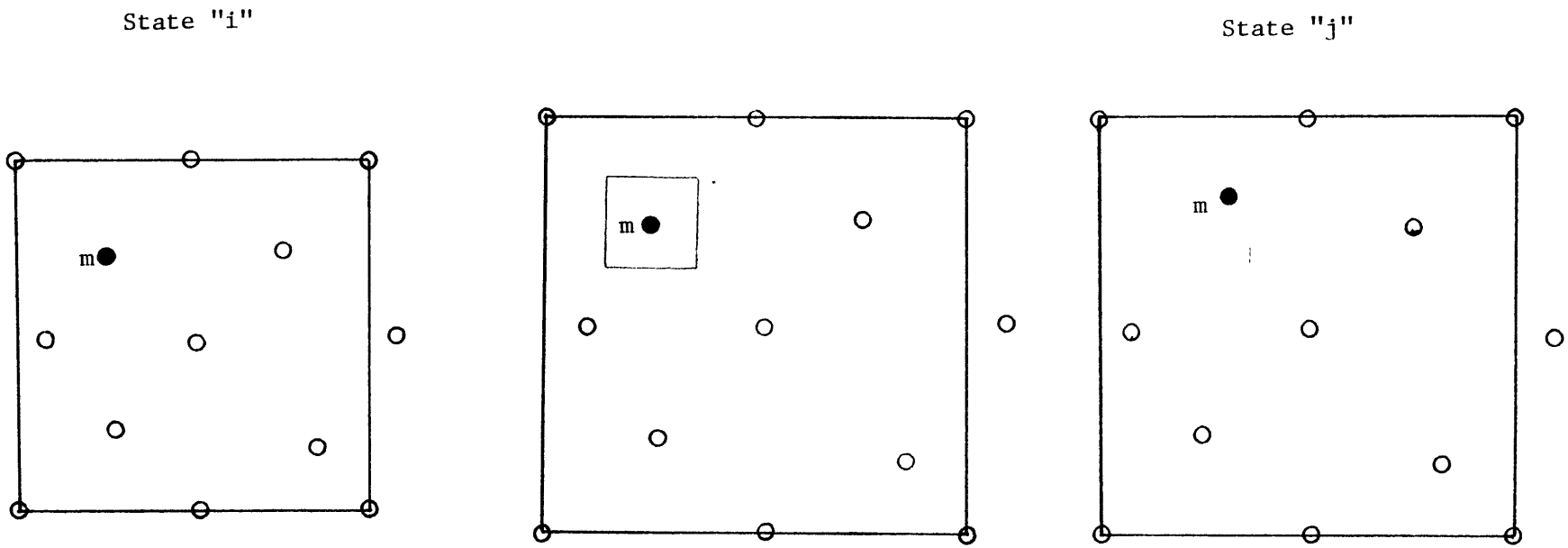

Fig. 2.1 A trial state "j" made from state "i" in a 2-dimensional system for isiobaric-isothermal ensemble sampling.

only those pair interactions which are affected by the movement of the particle "m".

2.5 "Isostress-Isothermal" Ensemble

2.5.1 Density Distribution Function

The probability density distribution function for a closed system in thermal and mechanical equilibrium with its surrounding (which we will call "isostress-isothermal" ensemble), in general is given [H56] by:

$$f(\vec{r}_i ; \vec{X}) = Exp\left\{-\frac{1}{kT}\left[\vec{X}\cdot\vec{x}_i + U_T(\vec{r}_i)\right]\right\} \Big/ \int d\vec{r}\, Exp\left\{-\frac{1}{kT}\left[\vec{X}\cdot\vec{x}_i + U_T(\vec{r}_i)\right]\right\} \tag{2.35}$$

where X is the vector of the generalized forces corresponding to the generalized coordinates x, and is defined by the thermodynamic equation [H56].

$$dE = TdS - \vec{X}\cdot d\vec{x} \tag{2.36}$$

In order to make explicit $\vec{X}$ and $\vec{x}$ we should find out an appropriate expression for the external work done on the system, namely the $\vec{X}.d\vec{x}$ term in Eq. (2.36) for a system under constant stresses.

In this ensemble the shape of the system is described by three vectors, $\vec{a}$, $\vec{b}$ and $\vec{c}$ that span the edges of the system, see Fig. 2.2. The vectors $\vec{a}$, $\vec{b}$ and $\vec{c}$ can have different lengths and arbitrary mutual orientations. Equivalantly the system can be described by a 3x3 matrix $\underline{\underline{h}}$ whose columns are the components of $\vec{a}$, $\vec{b}$ and $\vec{c}$ [P81]

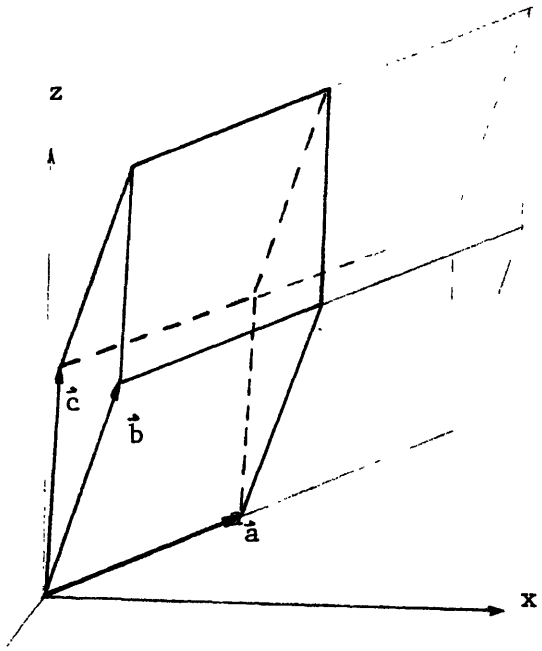

Fig. 2.2 Simulation cell made by three vectors a ,b and c, and one of its 26 images.

The work done on the system by the external stress tensor $\underline{\underline{\sigma}}$ is given [L61] by:

$$\delta W = V \sum_{ik} \left\{ \left[\left(\underline{\underline{h}}' \underline{\underline{h}}_0^{-1} \right)^t \right]^{-1} \right\}_{ik} d\epsilon_{ik} \tag{2.37}$$

where $\underline{\underline{h}}_o$ is the matrix describing the reference system and $\underline{\underline{h}}'$ the deformed system, $\underline{\underline{\epsilon}}$ is the Lagrangian strain defined [L59] in terms of $\underline{\underline{h}}'$ and $\underline{\underline{h}}_o$,

$$\underline{\underline{\epsilon}} = \frac{1}{2} \left[\underline{\underline{h}}_0^{-1} \cdot \underline{\underline{h}}'^t \cdot \underline{\underline{h}}' \cdot \underline{\underline{h}}_0^{-1} - 1 \right] \tag{2.38}$$

and V is the volume of the deformed system given by:

$$V = \sqrt{|\det (1 + \underline{\underline{\epsilon}})|} \cdot V_0 \tag{2.39}$$

with V_o being the reference system volume and superscript "t" stands for transpose. The above equations are valid for infinitesimal homgeneousdeformation. As a first approximation Eqs. (2.37) to (2.39) can be written as:

$$\begin{aligned} \delta W &= V_0 \, Tr \, \underline{\underline{\sigma}} \, d\underline{\underline{\epsilon}} \\ V &= V_0 \\ \underline{\underline{\epsilon}} &= \left[\underline{\underline{h}}' \underline{\underline{h}}_0^{-1} - 1 \right] \end{aligned} \tag{2.40}$$

where the new strain is called infinitesimal strain. Then the generalized force $\vec{X}$ in Eq. (2.36) has the form

$$(X)_{ik} = V_0 \sigma_{ik} \tag{2.41}$$

and Eq. (2.35) becomes:

$$f(\vec{r}_i ; \vec{x}) = Exp\left\{-\frac{1}{kT}\left[V_0 \, Tr \, \underline{\underline{\sigma}} \, \underline{\underline{\varepsilon}}_i + U_T(\vec{r}_i)\right]\right\} \Big/ \int d\vec{r} \; Exp\left\{-\frac{1}{kT}\left[V_0 \, Tr \, \underline{\underline{\sigma}} \, \underline{\underline{\varepsilon}} + U_T(\vec{r})\right]\right\} \tag{2.42}$$

Note that the term Vo Tr $\underline{\underline{\sigma}}$ $\underline{\underline{\varepsilon}}$ could be replaced by

$$V P_{ex} + V_0 \, Tr \, (\underline{\underline{\sigma}} - P_{ex} \underline{\underline{I}}) \, \underline{\underline{\varepsilon}}$$

2.5.2 "Isostress - Isothermal" Ensemble Sampling

The average quantity $A(\vec{r})$ in the ensemble may be written as:

$$\langle A \rangle = \int d\vec{r} \; A(\vec{r}) f(\vec{r}; \vec{x}) \Big/ \int d\vec{r} \, f(\vec{r}; \vec{x}) \tag{2.43}$$

and using Eq. (2.42) for $f(\vec{r};\vec{x})$. The integral $\int d\vec{r}$, as in Eq. (2.33) may be replaced by

$$\int_0^\infty dV \, (V)^N \int_{V=1} d\vec{s}_1 \cdots \int_{V=1} d\vec{s}_N \tag{2.44}$$

The volume V is defined by the matrix $\underline{\underline{h}}$. Since we are only concerned with pure deformation (no rigid body rotation), then the infinitesimal matrix strain $\underline{\underline{\varepsilon}}$ in Eq. (2.40) should be symmetric [B65] under symmetrical stress tensor. This means that if we start the Markov chain with:

$$\underline{\underline{h}}_i = \begin{bmatrix} h_{11i} & 0 & 0 \\ 0 & h_{22i} & 0 \\ 0 & 0 & h_{33i} \end{bmatrix} \tag{2.45}$$

then to avoid rotation during the Markov chain process, the following relations should hold between elements of $\underline{\underline{h}}$ matrix at all times:

$$\begin{aligned} h_{21} &= \frac{h_{11i}}{h_{22i}} \cdot h_{12} \\ h_{31} &= \frac{h_{11i}}{h_{33i}} \cdot h_{13} \\ h_{32} &= \frac{h_{22i}}{h_{33i}} \cdot h_{23} \end{aligned} \tag{2.46}$$

Eq. (2.46) reduces the 9 variables describing the volume to 6 independent variables. Now, the development of the Markov chain for this ensemble is the same as isobar-isothermal ensemble (the revised one) except that the volume of the trial state is described by some matrix $\underline{\underline{h}}$ whose elements are chosen as follows:

$$\begin{aligned} h'_{11} &= h_{11} + (1-\xi_{11})\,\delta^h_{11} \\ h'_{12} &= h_{12} + (1-\xi_{12})\,\delta^h_{12} \\ h'_{13} &= h_{13} + (1-\xi_{13})\,\delta^h_{13} \\ h'_{22} &= h_{22} + (1-\xi_{22})\,\delta^h_{22} \\ h'_{23} &= h_{23} + (1-\xi_{23})\,\delta^h_{23} \\ h'_{33} &= h_{33} + (1-\xi_{33})\,\delta^h_{33} \end{aligned} \tag{2.47}$$

where $\xi_{11},\ldots,\xi_{33}$ are random numbers distributed uniformly on the interval (0,1), and $\delta^h_{11},\ldots\delta^h_{33}$ are discussed in section (2.6) and the other three elements are calculated using Eq. (2.46), also replacing $P_{ex}V$ term in isobar-isothermal ensemble by $V.Tr\ \underline{\underline{\sigma}}\ \underline{\underline{\varepsilon}}$.

The prescription given in Eq. (2.47) to change the volume is one of the many ways that this could be done. For example, one may

change one of the elements of matrix $\underline{\underline{h}}$ at a time to get $\underline{\underline{h}}'$, or change one of the diagonal elements and one of the off-diagonal elements of $\underline{\underline{h}}$ at a time, or so on. We have tried the above two ways and the one described by Eq. (2.47)to change $\underline{\underline{h}}$. Qualitatively speaking, Eq. (2.47) gives a faster convergence.

As it was mentioned, Eq. (2.42) is not an exact equation and is valid only for small strains (compare to unity); then after many trials the strains of the state relative to the reference state $\underline{\underline{h}}_o$ may be large. To avoid this problem, the reference system can be updated after some trials, and Vo and $\underline{\underline{h}}_o$ in Eq. (2. 40) are replaced by the new values.

2.6 Determination of δ Parameters

The δ parameters in principle should be adjusted for optimum rate of convergence of the Markov chain. In a canonical ensemble where there is only one δ it is empirically found [W68] that a reasonable choice leads to about 50% rejection of the trial states. In our case there are more than one δ, thus there are many combinations of δ's that will produce 50% rejection rate. Throughout this work we have used the following method to determine δ parameters.

We assume all the δ parameters to be zero except one of them, then adjust the non-zero δ to have 50% rejection rate (the starting state should be quite close to equilibrium). The method is repeated for all δ's. The combination of the adjusted values, of course, does not lead to 50% rejection, therefore they are uniformly scaled to produce 50% rejection rate.

2.7 Flexible Periodic Border Condition

The number of particles in a simulation cell is limited by the computer size and time. To avoid the surface effects periodic border is used. The simulation cell is periodically repeated in all directions producing 26 image cells in 3-dimension. Usually the shape and the volume of the simulation cell are kept constant. In this case we call it conventional periodic border. In cases where the simulation cell is described by the three vectors, $\vec{a}$, $\vec{b}$ and $\vec{c}$ or equivalantly by the matrix $\underline{\underline{h}}$ and changing during the simulation we call it flexible periodic border condition.

Chapter 3

Thermodynamic Properties of Perfect Crystal

3.1 Introduction

Thermodynamic properties of rare gas solid argon have been well studied by Monte Carlo and molecular dynamics techniques. The Monte Carlo studies have for the most part confined to calculations in canonical ensemble or NVT ensemble. In this Chapter, potential energy, volume, bulk modulus, thermal expansion coefficient and specific heat of argon are simulated in the isobaric-isothermal or NPT ensemble described in Chapter 2. The Lennard Jones potential is used to describe the interatomic interaction. These results are used to calibrate our technique and to compare them with the experimental results.

3.2 Computational Details and Results

The calculations reported here have been made for 3-dimensional systems of 32 and 108 particles interacting through the Lennard Jone potential with the parameters $\varepsilon = 119.8°K$ and $\sigma = 3.405\text{Å}$ [H64] using the flexible periodic border condition and the isobaric-isothermal prescription of the Monte Carlo technique described in Chapter Two. The cut off range used is the midpoint between the second and third nearest neighbors (for discussions of the cut off range see 5.2), $r_c^2 = 4.95\ \sigma^2$. The long range interaction was approximated by assuming that beyond the cut off range the interatomic distances are those of the perfect fcc lattice.

As it is explained in Section 2.4, the trial state (S^t) in the simulation is found by changing the volume uniformly and dis-

placing one of the particles(m) in the system. In order to accept or reject the trial state as a new state, one needs to know the potential of the trial state. This potential energy calculation, in general, involves calculating all pair interactions. In this study the potential of a state (S') with the same volume v_o as the volume of the old state (S°) when the particle, m, is displaced is calculated. This calculation involves the interactions of the displaced particle and other particles. Now the potential of the trial state, which is the same as the state (S') except that its volume is changed uniformly to V_n, is given by

$$\Phi(S^t) = \phi_1 \left(\frac{v_o}{v_n}\right)^4 + \phi_2 \left(\frac{v_o}{v}\right)^2 \tag{3.1}$$

where

$$\phi_1 = 4\varepsilon\Sigma \left(\frac{1}{r}\right)^{12} \text{ and } \phi_2 = 4\varepsilon\Sigma\left(\frac{1}{r}\right)^6 \tag{3.2}$$

ϕ_1 and ϕ_2 are for the state (S').

All the simulations started from an ordered structure and continued for 20,000 to 25,000 steps/particle where the first 5000 steps/particle wre discarded as the transition period needed to get to the equilibrium.

In order to find out how fast the technique responds to a sudden pressure change, at the temperature of 40°K the simulation started with the external pressure being at 0. kbar then at 12,000 step / particle it was changed to 2.0 kbar and simulation proceeded

up to 29,000 step / particle . At this point the external pressure was again changed to 4.0 kbar, In Fig. 3.1a and b the program responses for the internal pressure and the volume of the 32 particle system are shown.

The simulation results at the temperature of 37.3°K and the pressure of 1.87 kbar are within the 0.1% agreement of the molecular dynamics results [D75]. The results for 32 and 108 particle systems shows no significant number dependence effects.

The simulation results of an isobar line in solid phase (P = 1.0 kbar) are shown in Fig. 3.2 along with experimental data [L74, A75, Z79] . The molar volume agreement with the experimental result is to within 0.5%, the bulk modulus is to within 2.0%, the specific heat at constant pressure to within 24.0% and thermal expansion coefficient to within 24.0%. The discrepancies are mainly due to the Lennard Jones potential where its long range interaction is in error by a factor of 2 [B76], although the quantum corrections may slightly change the results. The temperature was increased to the liquid phase in order to observe the melting of the system. It is seen from Fig. 3.3 that there are jumps in the range of 100-110°K in the potential energy and the volume of the system. The melting experimental value at 1 kbar is about 108°K [A75].

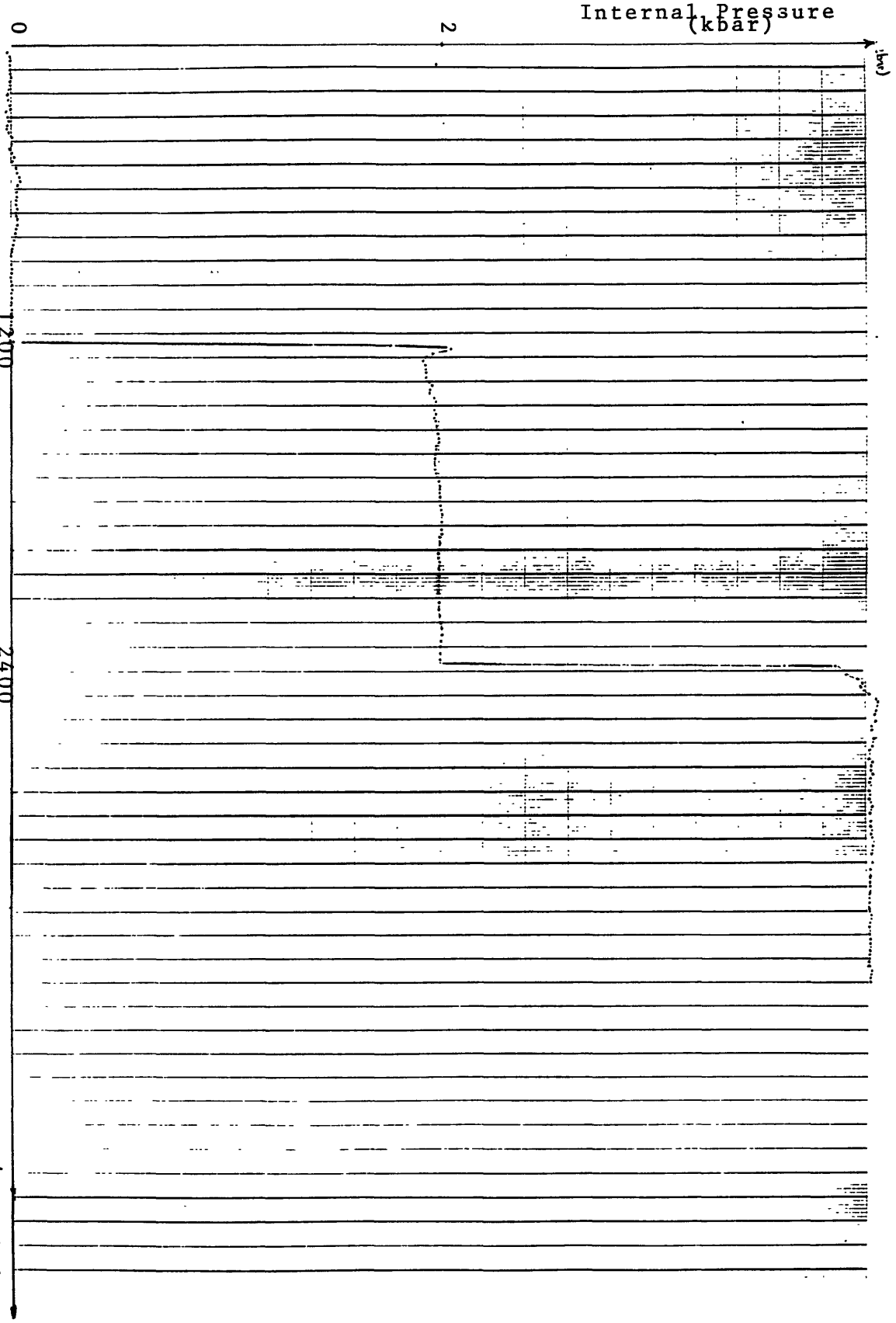

Fig. 3.1 a Internal pressure response of the technique to the external pressure changes as afunction of step/particle (argon at 40°K).

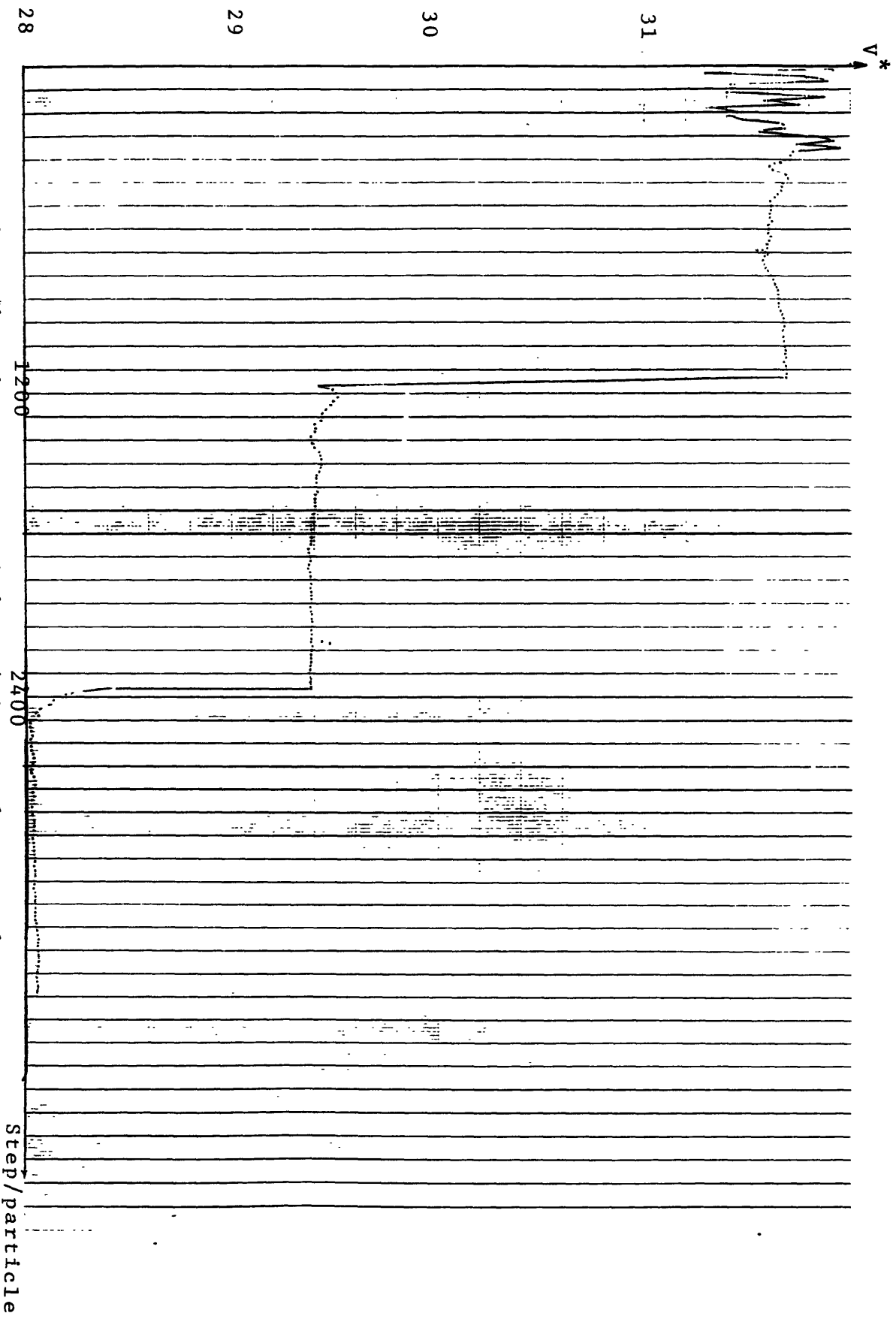

Fig. 3.1b Volume response of the technique to the external p-essure changes as afunction of step/particle (argon at 40°K).

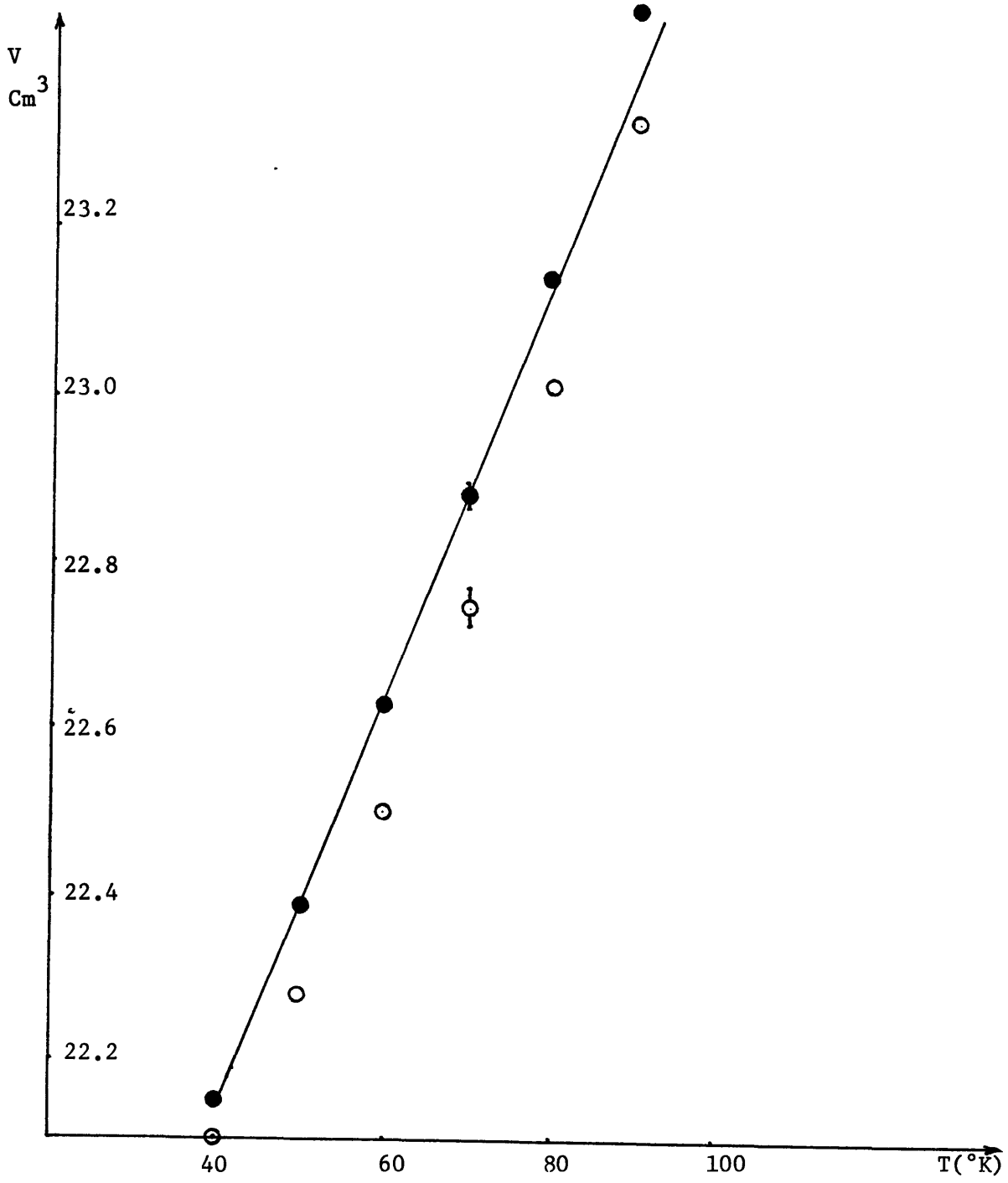

Fig. 3.2a Calculated (●) and experimental(○) molar volume of solid argon as a function of temperature at 1.0 kbar pressure.

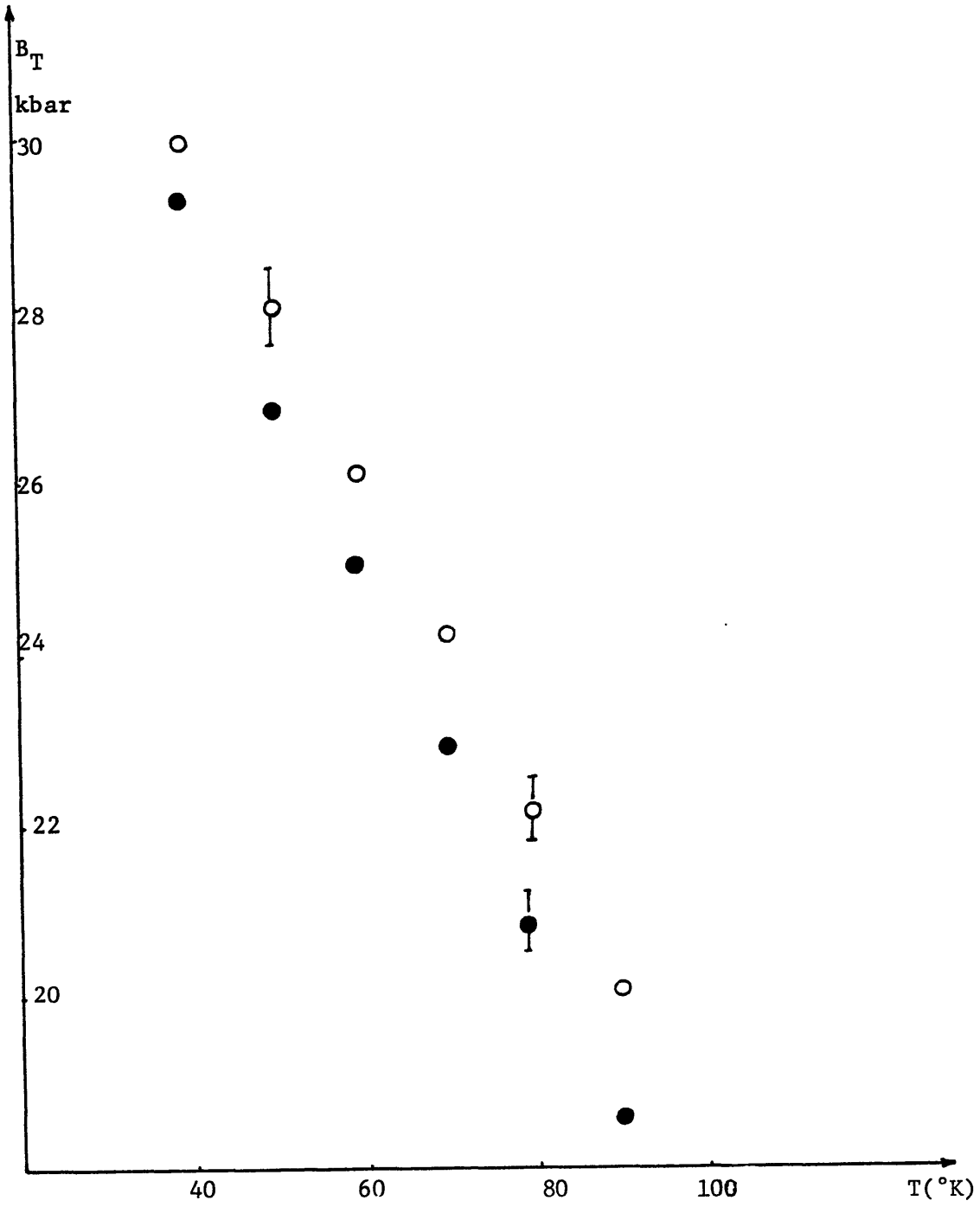

Fig. 3.2b Calculated (●) and experimental (O) bulk modulus of solid argon as a function temperature at 1.0 pressure.

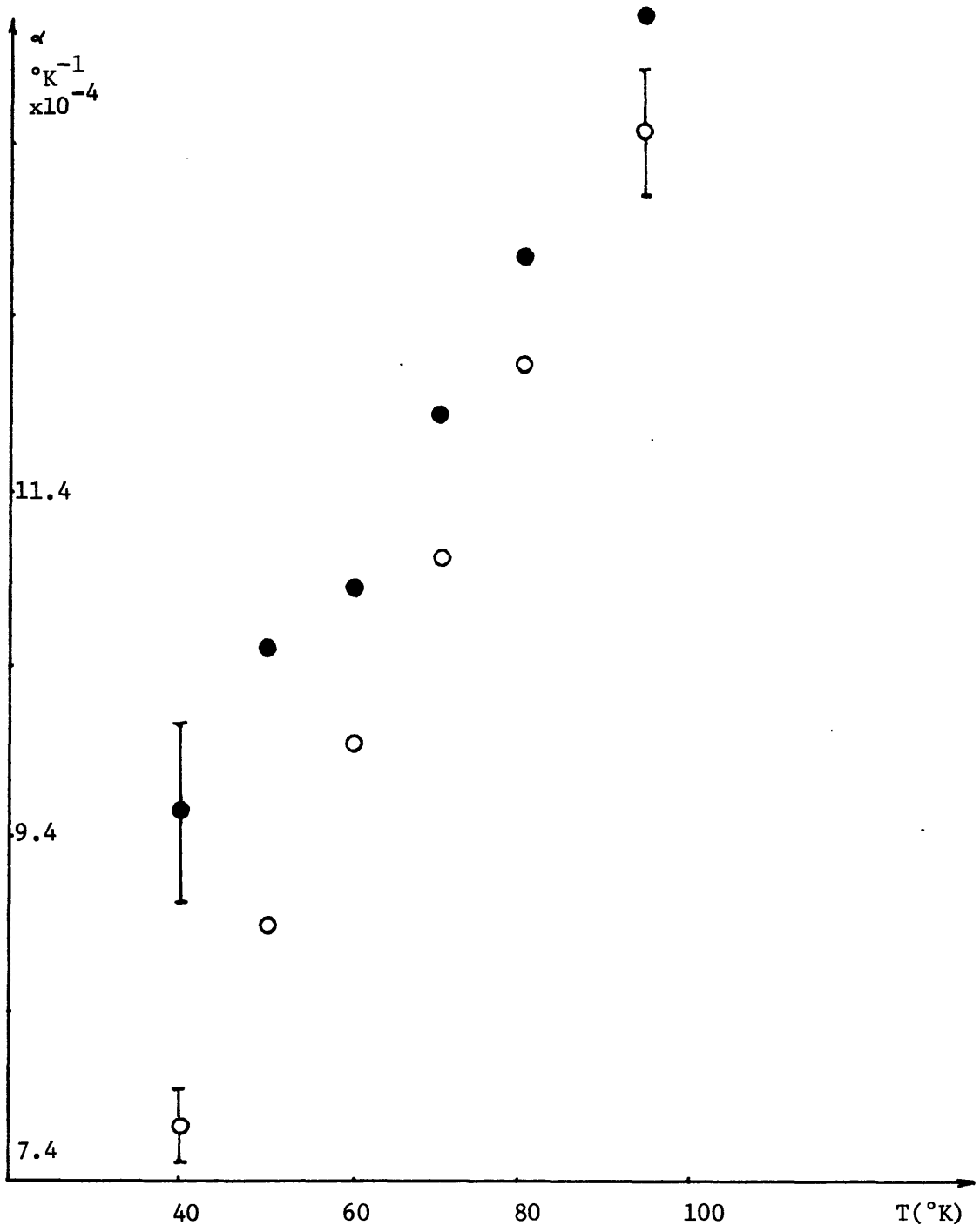

Fig. 3.2c Calculated (●) and experimental (○) thermal expansion coefficient of solid argon as a function of temperature at 1.0 kbar pressure.

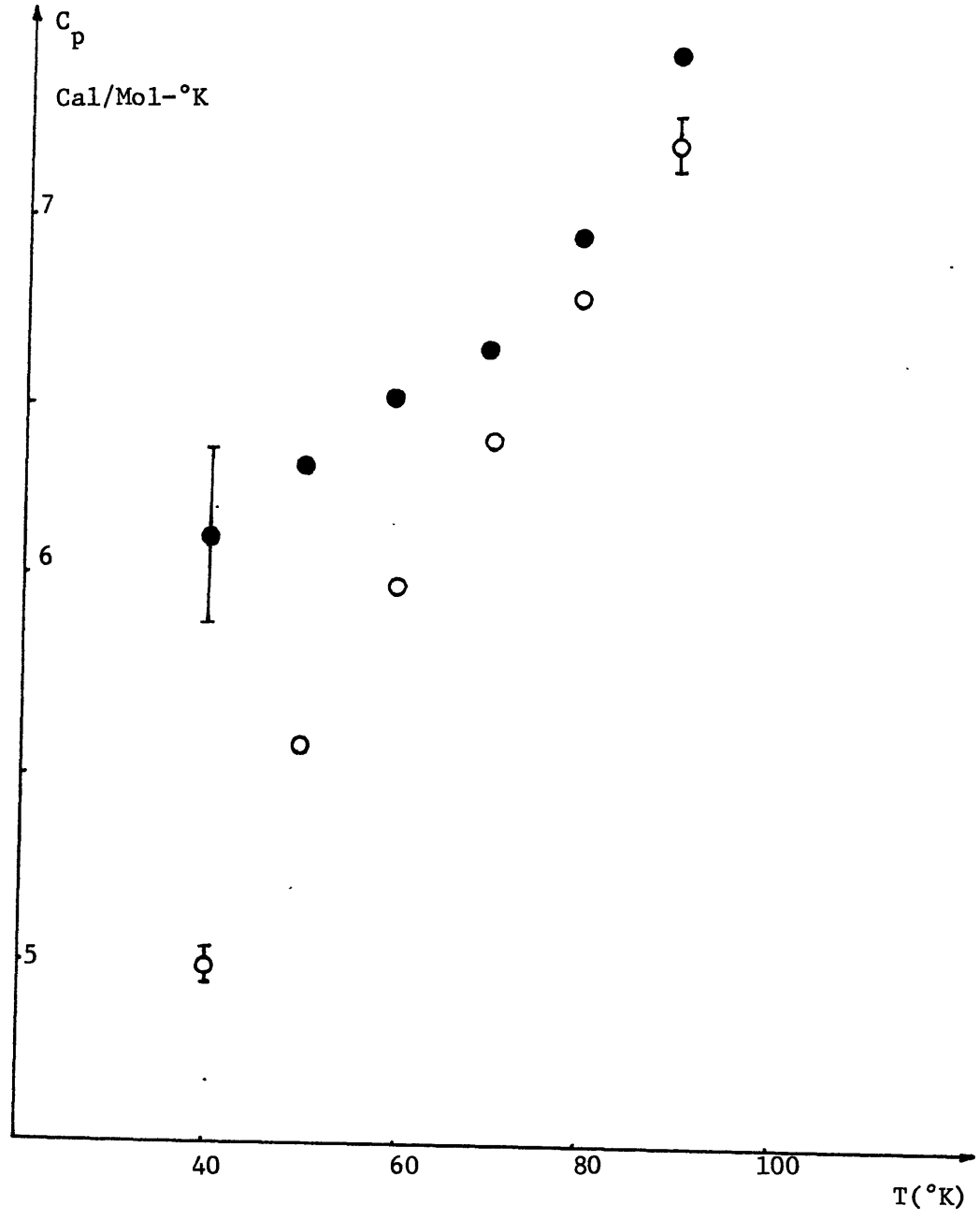

Fig. 3.2d Calculated (●) and experimental (○) specfic heat of solid argon as a function of temperature at 1.0 pressure.

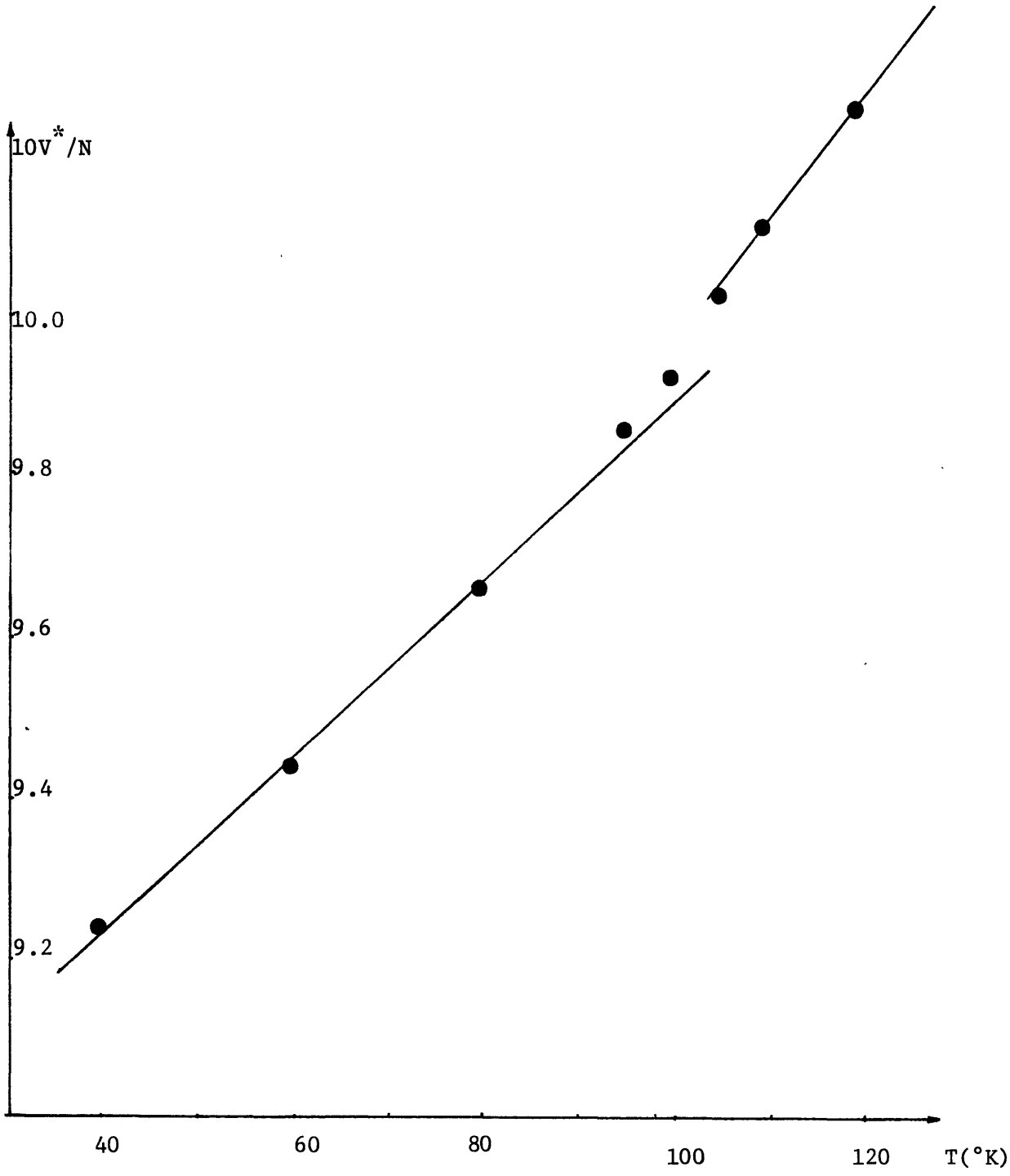

Fig. 3.3a Calculated volume of 108 particle system of argon as a function of temperature at 1.0 kbar pressure.

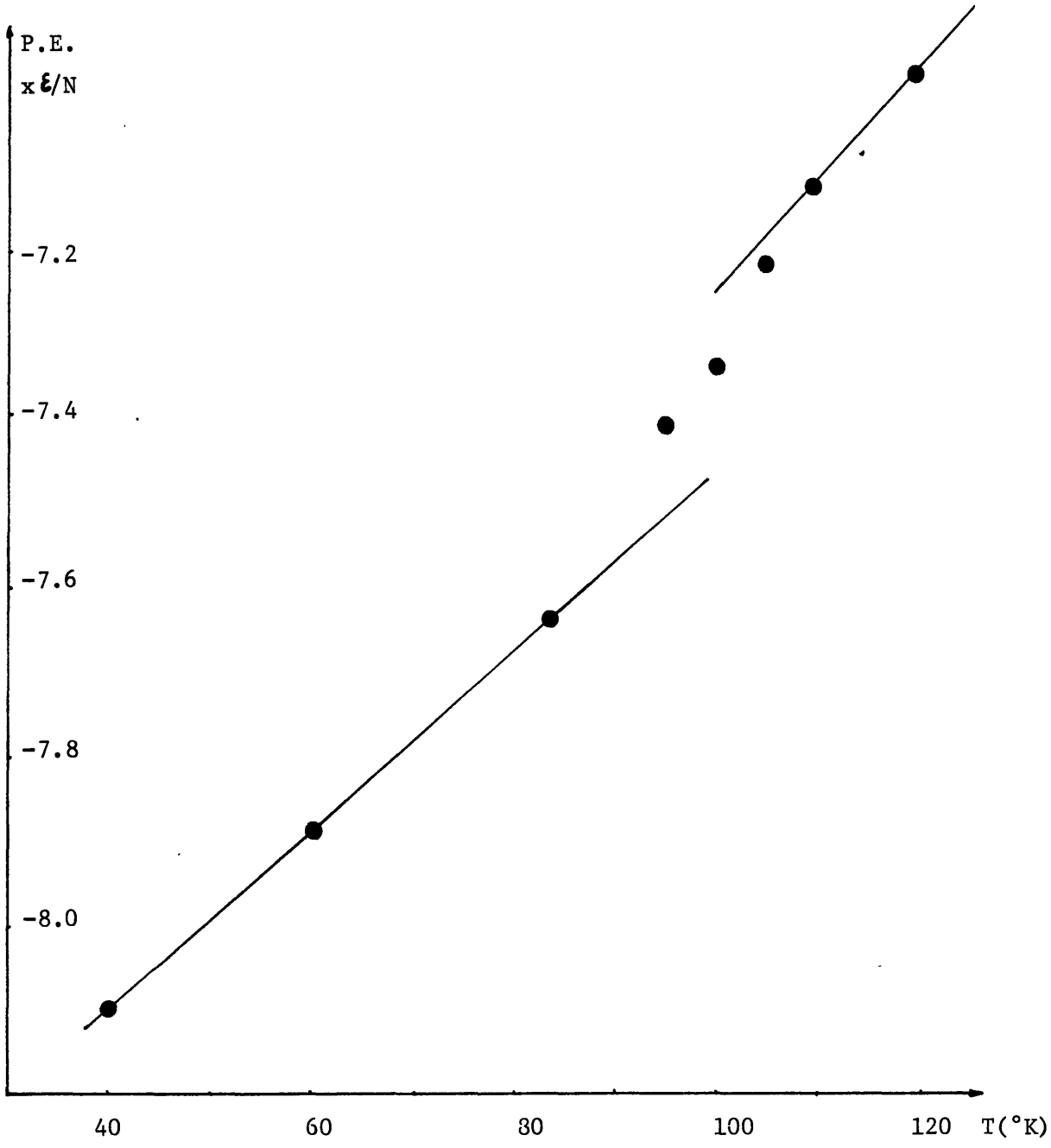

Fig. 3.3b Calculated potential energy of a 108 particle system of argon as a function of temperature at 1.0 kbar pressure.

Chapter 4

Structural and Mechanical Properties of Perfect Crystals

(Static Calculation)

4.1 Introduction

Necessary conditions for the thermodynamic stability of a perfect lattice are that the crystal be mechanically stable with respect to arbitrary small homogeneous deformations. Born [B54] derived the mathematical expressions for these stability requirements for cubic lattices of the Barvais type on the assumption of central faces of a very general form.

The Born stability criteria recently [M72[c],M71] have been applied to study the mechanical stability of cubic crystals which are deformed homogeneously under the application of external stresses. These studies are of interest because the values of stress and strain at which the crystals become mechanically unstable represent the "theoretical strength" of the crystal. These values are upper limits for corresponding values of a real crystal. These studies are also of interest because they provide a stress-strain curve for a crystal at absolute zero temperature which stress-strain curve is used as a reference for those calculated in Chapter IV for finite temperature.

A mathematical procedure is presented for applying the Born stability criteria to the determination of the mechanical stability of cubic crystals under applied stresses in section (4.2). In section (4.3) the calculations are carried out for (fcc) argon crystal using Lennard-Jones potential and for (bcc) iron crystal using Johnson I and Morse potentials. It turns out that the Johnson potential is a much more realistic potential to be used to study mechanical properties of iron. The "theoretical strength" of Morse potential is a factor of 7 lower than that of the experimental data [B56[b]] 9×10^{10} dyn/cm^2.

4.2 Theory

4.2.1 General Theory

For a cubic crystal lattice which is homogeneously deformed by the application of external forces, the internal energy may be expressed in terms of six independent variables that describe the unit cell. Figures (4.1a - 4.1c) respectively illustrate convenient unit cells for bcc and fcc crystals in the state of zero stress, and that of a bcc crystal with a normal stress applied parallel to an edge of the cube. The variables a_i, i=1, 2,...,6 describe the unit cell; a superscript "o" is used to denote the values of the lattice parameters in the absence of applied forces. The following notation [M71] is used to express the energy of unit cell of the lattice

$$U(a_1^k, a_2^k, \cdots, a_6^k) = U(a_i^k) \qquad (4.1)$$

In order for the lattice to be in mechanical equilibrium in the state (a_i^k), there must be an equilibrium of forces between the externally applied forces and the internal forces resulting from the mutual potential energy of the atoms. This equilibrium is identically satisfied [M71] if the "generalized forces," F_i^k, acting on the lattice in the state (a_i^k) are given by

$$F_i^k = -\frac{\partial U}{\partial a_i}\Big|_{(a_i^k)} \qquad (4.2)$$

where the F_i^k are defined such that the work involved is a small deformation of the lattice (δa_i^k in the state a_i^k). The $F_{i\,s}^k$ are

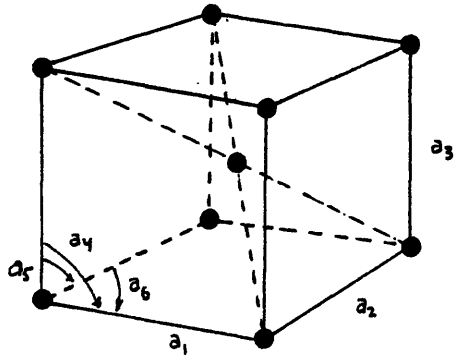

$a_1 = a_2 = a_3 = a_0$

$a_4 = a_5 = a_6 = 90°$

bcc

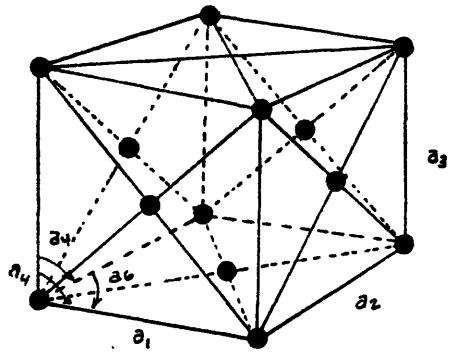

$a_1 = a_2 = a_3 = a_0$

$a_4 = a_5 = a_6 = 90°$

fcc

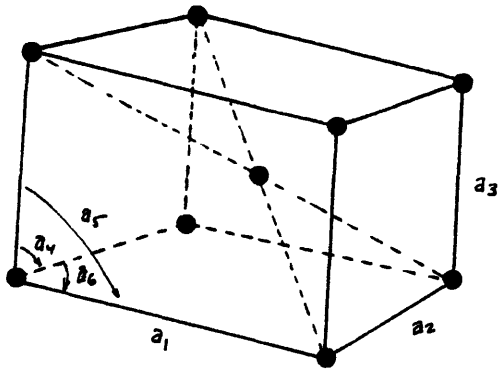

$a_1 = a_2 \neq a_3$

$a_4 = a_5 = a_6 = 90°$

bct

Fig. 4.1 Convenient unit cells for bcc and fcc crystals.

$$\delta W = \sum_{i=1}^{6} F_i^{\kappa} \delta a_i^{\kappa} \tag{4.3}$$

For the special case in which the edges of the unit cell a_i, i=1,2,3 are orthogonal, F_a may be related to the normal stress acting on the plane (of the unit cell) defined by the two edges a_b and a_c (i.e., the plane perpendicular to a_a) by

$$\sigma_a = \frac{F_a}{(a_b \cdot a_c)} \tag{4.4}$$

where a,b,c are permutations of 1,2.3. Thus, under the condition of equilibrium of forces, Eq. (4.2), the normal stress acting on a face of the unit cell when the cell edges are perpendicular to each other is given by

$$\sigma_a^{\kappa} = \frac{-1}{(a_c^{\kappa} \cdot a_b^{\kappa})} \left. \frac{\partial U}{\partial a_a} \right|_{(a_i^{\kappa})} \tag{4.5}$$

Equation (4.2) thus gives the conditions for the lattice to be in equilibrium with respect to internal and external forces. However, in order for the lattice to be in a stable equilibrium, there is an additional constraint, namely, that the total energy of the system consisting of the lattice in the presence of the applied forces must be at a minimum. In other words, if the state of the lattice specified by the six components (a_i^k) is one of the stable equilibrium, there must be required a positive expenditure of energy to go from state (a_i^k) to any nearby state (a_i). This energy expenditure is equal to

the difference in the internal potential energy between the state (a_i^k) and the state (a_i) plus the work done by the lattice on its surroundings (i.e., the negative of the work done by the external forces on the lattice). The difference in the internal potential energy between the states (a_i) and (a_i^k) is expressed in terms of a Taylor's series expansion

$$U(a_i^\ell) = U(a_i^\kappa) + \sum_{i=1}^{6} \left(\frac{\partial U}{\partial a_i}\right)_{(a_i^\kappa)} (a_i^\ell - a_i^\kappa) + \frac{1}{2} \sum_{i=1}^{6} \sum_{j=1}^{6} \left(\frac{\partial^2 U}{\partial a_i \partial a_j}\right)_{(a_i^\kappa)} (a_i^\ell - a_i^\kappa)(a_j^\ell - a_j^\kappa) \qquad (4.6)$$

The deformations ($a_i - a_i^k$) are taken to be small so the series is terminated after second-order terms. (Neither ($a_i - a_i^o$) nor ($a_i^k - a_i^o$) are necessarily small, however). In terms of the definition of equilibrium, the generalized forces acting on the lattice in the state (a_i^k) must be $\left(\frac{\partial U}{\partial a_i}\right)_{(a_i^\kappa)}$, therefore the first term on the right-hand side of Eq. (4.6) is seen to be identically equal to the work done by the external forces in going from state (a_i^k) to state (a_i^ℓ). Thus a positive expenditure of energy will be required for this transition if and only if the second term on the right-hand side of Eq. (4.6) is positive. For convenience, let

$$\left(\frac{\partial^2 U}{\partial a_i \partial a_j}\right)_{(a_i^\kappa)} = B_{ij}^{\kappa} \qquad (4.7)$$

The double sum in Eq. (4.6) will be positive for an arbitrary deformation [H52] ($a_i - a_i^k$) if and only if the principal minors of the

determinant $|B_{ij}^{k}|$ are all positive. Thus, the condition for stable equilibrium is that the determinant of the matrices of successive orders as marked out below (principal minors) are all positive.

$$[B]^{K} = \begin{bmatrix} B_{11} & B_{12} & B_{13} & B_{14} & B_{15} & B_{16} \\ B_{21} & B_{22} & B_{23} & B_{24} & B_{25} & B_{26} \\ B_{31} & B_{32} & B_{33} & B_{34} & B_{35} & B_{36} \\ B_{41} & B_{42} & B_{43} & B_{44} & B_{45} & B_{46} \\ B_{51} & B_{52} & B_{53} & B_{54} & B_{55} & B_{56} \\ B_{61} & B_{62} & B_{63} & B_{64} & B_{65} & B_{66} \end{bmatrix}^{K} \tag{4.8}$$

Rewriting Eq. (4.6) in terms of F_i^{k} and B_{ij}^{k} as

$$U(a_i^{l}) = U(a_i^{K}) + \sum_{i=1}^{6} F_i^{K}(a_i^{l} - a_i^{K}) + \frac{1}{2}\sum_{i=1}^{6}\sum_{j=1}^{6} B_{ij}^{K}(a_i^{l} - a_i^{K})(a_j^{l} - a_j^{K}) \tag{4.9}$$

and differentiating the above equation with respect to a_i gives

$$F_i^{l} = -\left(\frac{\partial U}{\partial a_i}\right)_{(a_i^{l})} = F_i^{K} + \sum_{j=1}^{6} B_{ij}^{K}(a_j^{l} - a_j^{K}) \qquad i = 1, 2, \ldots, 6 \tag{4.10}$$

For application of the above formalism to a specific crystal, in general, the reader may refer to the discussion by Milstein [M71]. A specific application is given in the following section.

4.2.2 Crystal Under Uniaxial Force

For a cubic crystal with a uniaxial force applied perpendicular to one of its faces, parallel to, say the edge a_1, and in the absence of applied shear stresses, the components a_4,a_5 and a_6 will retain their initial values of $\pi/2$ (at least up until failure occurs). For a tensile force, the edge a_1 will elongate and the edges a_2 and a_3 will contract. By symmetry it is seen that the relation $a_2=a_3$ will be maintained. (The deformed crystal will possess tetragonal symmetry).

An equilibrium state (a_i^k) must satisfy the conditons of force equilibrium

$$\left.\frac{\partial U}{\partial a_i}\right|_{(a_i^\kappa)} = 0 \qquad i \neq 1 \tag{4.11}$$

and

$$-\left.\frac{\partial U}{\partial a_1}\right|_{(a_i^\kappa)} = F_1^\kappa \tag{4.12}$$

where

$$a_2^\kappa = a_3^\kappa \quad \text{and} \quad a_4^\kappa = a_5^\kappa = a_6^\kappa = \pi/2 \tag{4.13}$$

and F_1^k is the applied load. The normal stress in the a_1 direction is simply

$$\sigma_1^\kappa = \frac{F_1^\kappa}{(a_2^\kappa)^2} \tag{4.14}$$

As a result of the symmetry of the crystal structure, for i=4,5,6 the equations summarized in Eq. (4.11) are identically satisfied

and for i=2,3 these equations are identical to each other. Hence, the relations (4.11) will be satisfied if

$$\left.\frac{\partial U}{\partial a_2}\right|_{(a_i^\ell)} = 0 \qquad (4.15)$$

Furthermore, the special symmetry of the crystal in this case also greatly simplifies the matrix elements B_{ij} [M71].

$$\begin{bmatrix} B_{11} & B_{12} & B_{12} & 0 & 0 & 0 \\ B_{12} & B_{22} & B_{23} & 0 & 0 & 0 \\ B_{12} & B_{23} & B_{22} & 0 & 0 & 0 \\ 0 & 0 & 0 & B_{44} & 0 & 0 \\ 0 & 0 & 0 & 0 & B_{55} & 0 \\ 0 & 0 & 0 & 0 & 0 & B_{55} \end{bmatrix} \qquad (4.16)$$

The principal minors in the determinant of the above matrix for a lattice with central pairwise interatomic forces will be [M71] positive if

$$\begin{aligned} &B_{12} > 0 \\ &B_{23} > 0 \\ &B_{22} - B_{23} > 0 \\ \text{and}\quad &B_{11}(B_{22}+B_{23}) - 2(B_{12})^2 > 0 \end{aligned} \qquad (4.17)$$

and Eqs. (4.9 and 4.10) become

$$F_1^\ell = F_1^\kappa + B_{11}^\kappa (a_1^\ell - a_1^\kappa) + 2 B_{12}^\kappa (a_2^\ell - a_2^\kappa)$$

$$F_2^{\ell} = 0 = 0 + B_{12}^{\kappa}(a_1^{\ell} - a_1^{\kappa}) + (B_{22}^{\kappa} + B_{23}^{\kappa}) \cdot (a_2^{\ell} - a_2^{\kappa}) \qquad (4.18)$$

Rearranging Eq. (4.18) gives

$$(a_2^{\ell} - a_2^{\kappa}) = -[B_{12}^{\kappa}/(B_{22}^{\kappa} + B_{23}^{\kappa})](a_1^{\ell} - a_1^{\kappa}) \qquad (4.19a)$$

$$F_1^{\ell} = F_1^{\kappa} + [B_{11}^{\kappa} - 2((B_{12}^{\kappa})^2/(B_{22}^{\kappa} + B_{23}^{\kappa}))](a_1^{\ell} - a_1^{\kappa}) \qquad (4.19b)$$

Therefore the iteration process may begin with the known values of the lattice parameters $a_1^k = a_2^k = a_1^o$ for which all $F_i^k = 0$. After calculating the values of B_{ij}^k, the lattice parameter a_1 is elongated by a small amount $(a_1 - a_1^k)$. The value of a_2^k (for which $F_2 = 0$) is then found from Eq. (4.19a), and the value F_1 (which results in elongation $(a_1 - a_1^k)$) may be determined from Eq. 4.19b). The values of B_{ij} are evaluated for these values of lattice parameters and the iteration process is repeated until one of the stability relations is violated. The value of $F_1^f/(a_2^f)^2$ at which the instability occurs is the theoretical strength (stress) of the crystal and $(a_1^f - a_1^o)/a_1^o$ is the theoretical uniaxial strain.

4.2.3 Numerical Results

In the previous section, it has been assumed implicitly that for a given set of lattice parameters (a_i) the quantities F_i and B_{ij} can be calculated.

For a cubic crystal in which the atoms interact in a central pairwise potential, $\phi(1)$. The internal energy per unit cell is

written as

$$U = \frac{1}{2} n \sum \phi(r_j) \Big|_{(a_i)} \tag{4.20}$$

where n is the number of atoms per unit cell and r_j is the distance from an arbitrary atom in the lattice (chosen as the origin) to the j^{th} atom. This distance in a bcc or fcc crystal lattice which is subject to uniform deformations may be written as

$$\vec{r}_i = \frac{1}{2} \sum_{i=1}^{3} l_i a_i \hat{a}_i \tag{4.21}$$

where $\hat{a}_i$ are unit vectors in the direction of the cell edges a_i, and all the l_i are integers.

The quantities F_i and B_{ij} are given [M71] as

$$F_i = \frac{1}{4} n a_i \sum_{l_1,l_2,l_3} l_i^2 \frac{\partial \phi}{\partial (r^2)} \qquad i = 1, 2, 3 \tag{4.22a}$$

$$B_{11} = \frac{1}{8} n a_1^2 \sum_{l_1,l_2,l_3} l_1^4 \frac{\partial^2 \phi}{\partial^2 (r^2)} + \frac{1}{4} n \sum_{l_1,l_2,l_3} l_1^2 \frac{\partial \phi}{\partial (r^2)} \tag{4.22b}$$

$$B_{12} = \frac{1}{8} n a_1 a_2 \sum_{l_1,l_2,l_3} l_1^2 l_2^2 \frac{\partial^2 \phi}{\partial^2 (r^2)} \tag{4.22c}$$

The remaining B_{ij} may be found by switching subscripts in the above equations. For example, to find B_{22}, a_1 and l_1 are changed to a_2 and l_2 in Eq. (4.22b).

The static calculation method described above was used to investigate the response of a crystal to a uniaxially applied external

force along the (001) direction at zero temperature. The results are used as references to the corresponding results simulated for the same systems at finite temperature in Chapter 5. The following potential functions were used to describe the interatomic interaction between the atoms in the crystal:

i) Lennard-Jones

$$\phi(r) = 4\varepsilon \left[\left(\frac{\sigma}{r}\right)^{12} - \left(\frac{\sigma}{r}\right)^{6} \right] \tag{4.23}$$

The parameters ε and σ are chosen such that the potential represents an Argon crystal, the same value used in Chapter 3. The potential was truncated at the distance $r_c^2 = 4.95\ \sigma^2$, again the same value used in Chapters 3 and 5. The results are summarized in Fig. 4.2. It is seen that the static method predicts there is only one stable structure under condition of no stress for this truncated Lennard-Jones potential and it is the fcc structure with the lattice constant of 1.573σ ($a_1=a_2=a_3=1.573\sigma$ and $a_4=a_5=a_6=0$). The body centered tetragonal ($a_1=1.193\sigma$, $a_2=a_3=1.853$ and $a_4=a_5=a_6=0$) structures are unstable. It also predicts that at the tensile load greater than 2100 bar and the compressive load greater than 1000 bar there is no stable structure; in other words the system at these loads fails. Those values are the tensile and compressive theoretical strengths respectively. The discontinuities in the stress - strain curve are due to the discontinuity in the potential used.

ii) Morse Potential

$$\phi(r) = D\left[\exp\{-2\alpha(r-r_0) - 2\exp\{-\alpha(r-r_0)\}\right] \tag{4.24}$$

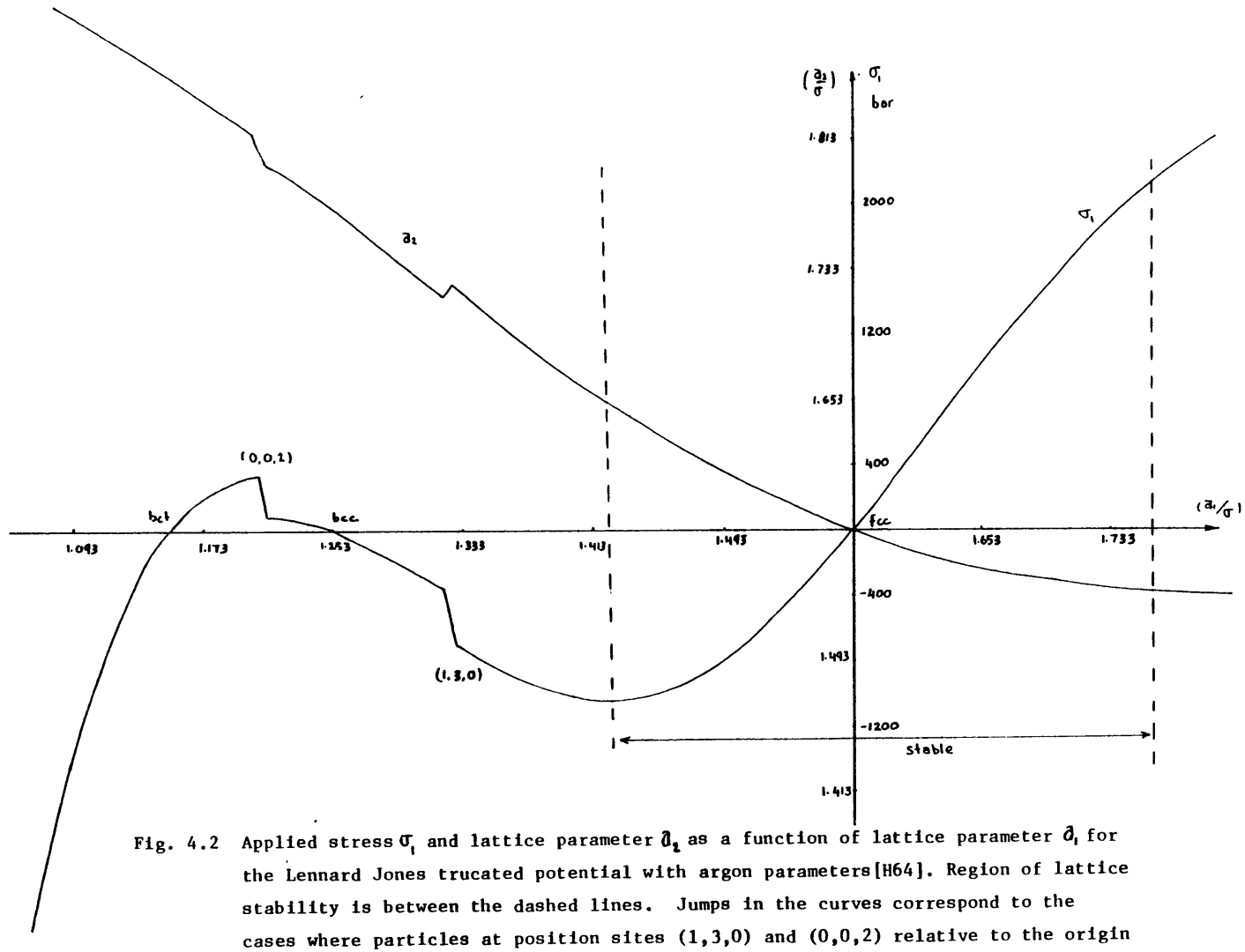

Fig. 4.2 Applied stress σ_1 and lattice parameter a_2 as a function of lattice parameter a_1 for the Lennard Jones trucated potential with argon parameters[H64]. Region of lattice stability is between the dashed lines. Jumps in the curves correspond to the cases where particles at position sites (1,3,0) and (0,0,2) relative to the origin are moving out of the interaction range.

The values of the potential parameters used in the present calculation are those given for the bcc iron [G53]. The potential was truncated at a distance of 14.76 A°. This is long enough to ignore the long range interaction effect. The results are shown in Fig. 4.3, as it is seen there are two stable structures at no stress condition which are bcc and fcc structures with lattice constant of 2.86 and 3.606 A° respectively. At the tensile load of $1.21*10^{10} dyn/cm^2$ the bcc structure become unstable. This value is the theoretical tensile strength which is almost an order of magnitude smaller than the experimental value of $13x10^{10}$ dyn/cm^2 [B56b]. On the basis of this result we conclude that the Morse potential will not lead to a sufficiently realistic simulation of the mechanical properties of bcc iron.

iii) Johnson Potential [J64]

The empirical Johnson potential is shown in Fig. 5.8 The results obtained using this potential are summarized in Fig. 4.4.

The results are markedly different from the corresponding results of the Morse potential. Again these are bcc and fcc stable structures under the condition of no stress with the lattice constant of 2.86 and 3.70 A° respectively. The correct prediction of bcc lattice constant by both Morse and Johnson potential is expected because the bcc lattice constant is one of the properties used to construct both potentials. The calculated fcc lattice constant is greater than the experimental value of 3.55 A°[L61] by 2% and 4.2% for Morse and Johnson potential respectively. In the figure 4.6 the transformation from deformed bcc to deformed fcc under tension is shown by A→A'

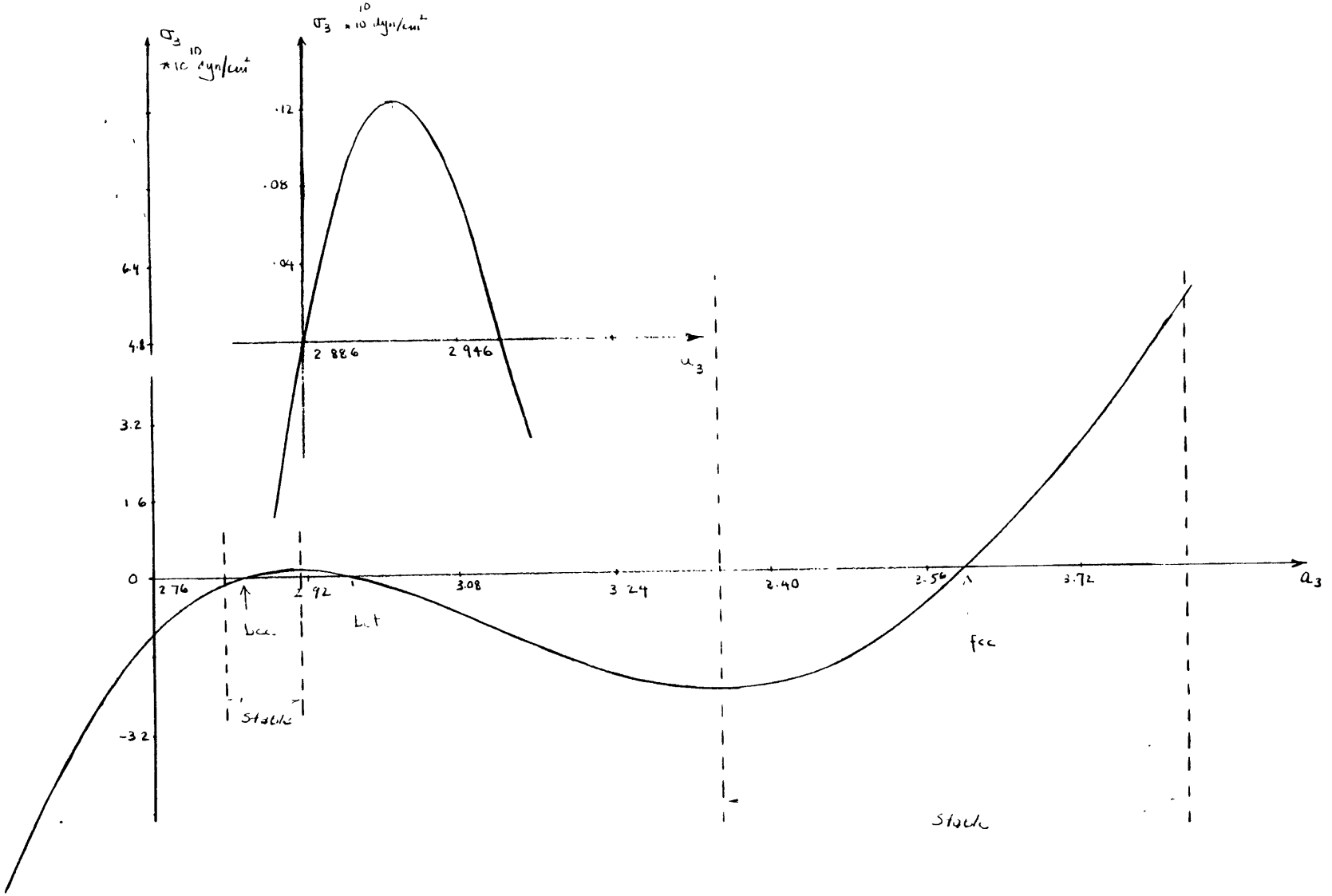

Fig. 4.3 Applied stress along the [001] direction as a function of lattice parameter in the [001] direction for Morse potential with the bcc iron parameters [G53].

and transformation from deformed fcc to deformed bcc under compression is shown by B'→B. The calculated theoretical tensile strength is $9*10^{10}$ dyn/cm^2 for the bcc structure which is off by 35% from the experimental value of $13*10^{10}$ dyn/cm^2. One would expect that the calculated theoretical strength to be greater than the experimental value because, Althoughthe experimental value is measured for fine iron whisters, it is not 100% pure and single crystal iron. The overall conclusion is that the Johnson I is a more reasonable potential than the Morse potential to be used in simulating the mechanical properties of fcc iron.

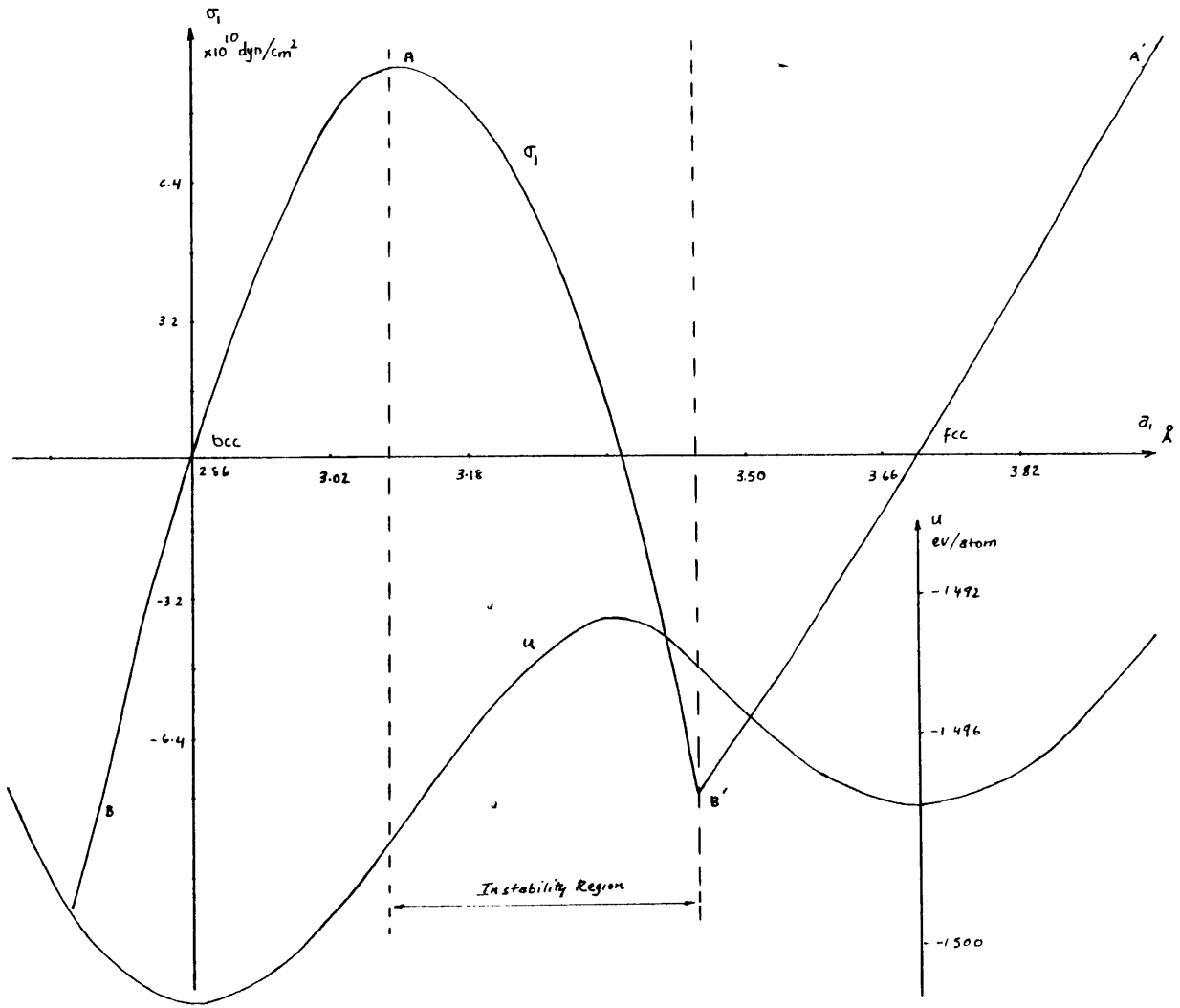

Fig. 4.4 Applied stress and internal energy as a function of lattice parameter along the stress direction for Johnson I potential[J64]. bcc under tension at point A transforms to a deformed fcc (point A') and fcc under compression at point B' transforms to a deformed bcc (point B).

Chapter 5

Structural and Mechanical Properties of Crystals

5.1 Introduction

The behavior of solids under the combined effects of external stress and of temperature has considerable practical relevence. Yet even in the idealized case of a perfect crystal, a detailed microscopic picture of such effects is still lacking. Most of the theoretical studies [H77, M72b, M71, M80] have been confined to conditions at zero temperature, in addition a perfect prefixed crystalline arrangement of the atoms has been assumed. These two assumptions may lead to useful insights for relatively small values of the stress and temperature. However, it is obviously desirable to be able to study the behavior of solids at normal temperatures and high levels of external stress. In particular, at high values of the stress spontaneous defect generation and/or crystal structure transformation become possible. This makes the assumption of a perfect, even if elastically distorted crystalline arrangement untenable. Furthermore, the stresses where these processes occur are dependent on the temperature.

In the first part of this chapter the work done based on the improved Monte Carlo method is presented. The model system which has been used is a system of classical particles interacting through a pairwise additive potential of the Lennard-Jones type. The parameters of potential have been determined [H64] to represent argon systems, the values being the same as those used in Chapter 3. This model of argon was used in this study primarily for two reasons. First, Macmillan and Kelly [M72c, b] have made static calculations of stress-strain relation using this model of argon. Also Squire et al. [S69b] have calculated elastic constants of argon at different temperatures.

These calculations provide convenient checks for our method of calculation. Secondly, isothermal bulk modulus have been measured for argon [P65]. So direct comparison between model calculation and experiment is possible.

The fcc crystal of argon was studied under uniform uniaxial load along [001] at 40 $\mathring{K}$. As the load was increased, the crystal homogeneously deformed and maintained its face centered tetragonal symmetry all the time. Beyond a value of 600 bar tension the system failed. It turns out that it is much smaller than the theoretical value of 3700 bar previously reported [M72b]. As the compression load increased beyond a value of 350 bar the system transformed to an hcp structure by a combination of large deformation and relative sliding of the (100) planes. The transformation fcc→hcp under compression loading has been observed by Parrinello and Rahman [P81] in a molecular dynamics simulation using a 500 particle system with a Morse potential describing the interaction between nickel atoms. On the basis of the two above fcc→hcp transformations, the fact that there is no bcc stable structure for the two above potentials, and the observation that the fcc→bcc transformation does occur for Johnson I potential as discussed in the second part of the chapter, one can conclude that the fcc→hcp transformation is more a manifestation of those potentials that will not stablize a bcc structure.

The calculated strain-stress curve for argon system at 40 $\mathring{K}$ is compared with that of the static calculation (Chapter 4) and the published results [M72b]. The effect of temperature on the stress-

strain curve at high stresses is significant, see Fig. 5.6. Temperature effects on the elastic constants result in a 12.8% decrease in c_{11} and 6.4% increase in c_{12} relative to their zero temperature values respectively. The calculated isothermal bulk modulus of 16.75 kbar is 22% lower than the experimental value [P65].

There exists a class of structural transformations in solids called the martensitic transformations which are common in iron, iron alloy, and many other materials [B56a]. This transformation, which occurs rapidly with a velocity approaching that of sound wave in the crystals [C65], is believed to occur through either a classical or a non-classical path [081, 082]. In classical path theory a nucleus having the product structure is created, whereas in a non-classical path the product is produced in a finite region through a continuous deformation of the parent structure. An example of non-classical martensitic transformations is the transformation predicted theoretically by Bain [B24] who suggested that under a compressive load one should be able to observe an fcc to bcc transformation, as is shown in Fig. 5.1. Such a transformation has been observed experimentally when fcc iron is quenched [Z65].

Martensitic transformations are defined as a subset of diffusionless displacive transformations, with sufficiently large lattice-distortive shear displacements that the transformation kinetics and product morphology are dominated by strain energy [082].

In the second part of this chapter we present the mechanical and structural properties of a model system of iron crystal where the Johnson I potential [J64] is used to describe the interatomic

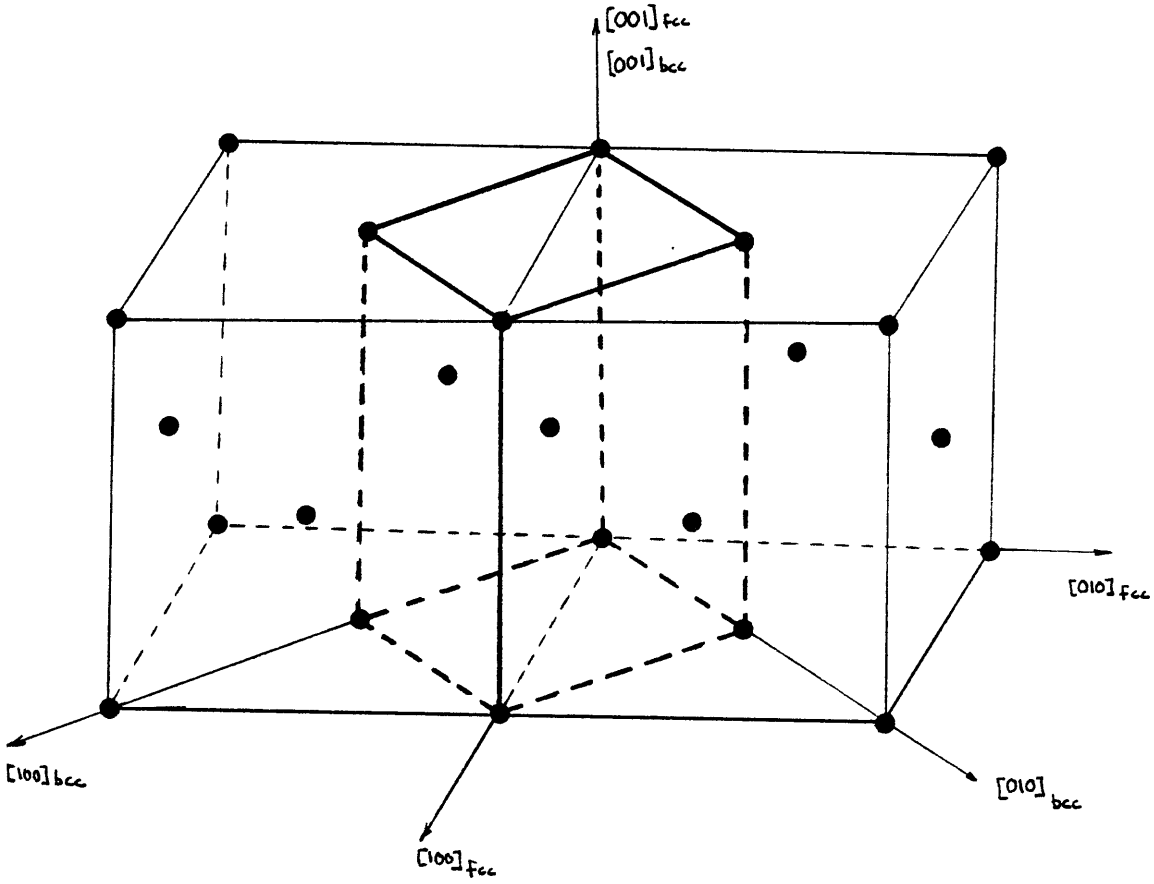

Fig. 5.1 The fcc lattice with a body centered tetragonal cell picked out of it.

interaction. The bcc iron behavior under the uniaxial tensile load along the [001] direction was studied using the improved Monte Carlo method described in Section 2.5. The system under tensile load deformed homogeneously by expanding in [001] direction and contracting in the [010] and [100] directions (by the same amount). The deformed structure was always body centered tetragonal. At the tensile load of $6*10^{10}$ dyn/cm^2 the system transformed to a deformed fcc structure. The fcc structure then was studied under the compressive load. Up to $5.5*10^{10}$ dyn/cm^2 the system behaved normally like the fcc argon under the compressive load. At the $5.5*10^{10}$ dyn/cm^2 load the fcc structure transformed to a new structure which was found to be the bcc structure when the load was removed. These non-classical Martensitic transformations, the bcc→fcc and fcc→bcc under the uniaxial tensile and compressive load respectively, can not be explained by the thermal activation energy concept for two reasons. First, they can occur even at zero temperature as it is shown in the stress-strain curve calculated using the static method in Chapter 4. Secondly, in the case of the bcc→fcc transformation the total energy of the system is increased (the total energy is the same as the free energy of the system at zero temperature). At the transformation points the parent structure is mechanically unstable, therefore the system transforms to a structure at which it is mechanically stable. Thus these transformations are not induced by the temperature, although the stresses at which they occur are dependent on the temperature. For example, the bcc→fcc occurs at $9*10^{10}$ and $6*10^{10}$

dyn/cm^2 for the system at 0 and 70 $\overset{\circ}{K}$ respectively, and also the fcc→bcc occurs at $7.7*10^{10}$ and $5.5*10^{10}$ dyn/cm^2 for the system at zero and 70 $\overset{\circ}{K}$ respectively.

The calculated stress-strain curve for the system at 70 $\overset{\circ}{K}$ is in good agreement with that obtained using the static method described in Chapter 4. The stress-strain for α iron under tensile load is also in agreement with the stress-strain curve measured for α iron whiskers [B56] to within 12% error. This latter agreement confirms that the Johnson I potential is a more realistic potential for simulating mechanical properties of α iron than the Morse potential (See Chapter 4).

In the section 5.3 we describe the system and the simulated results obtained for the iron crystal.

5.2 Study of Argon Crystal Under Uniaxial Load

The simulations were carried out on a perfect 3-dimensional fcc system consisting of particles interacting through the truncated Lennard-Jones 12-6 potential with the flexible periodic border condition described in Chapter 2 to avoid surface problems. Although most of the simulations were carried out on a 32 particles system, some simulations were also carried out on a 108 particle system to confirm firstly the number dependence effects on the quantities calculated here, for example strains, is negligible, and secondly and more importantly, the transformation is not an artifact of the small system of simulation. It was found out that the results for the 108 particle system were the same as those of the 32 particles system within the statistical uncertainty of the results. The Lennard-Jones potential used was truncated at the midpoint between the second and the third neighbor for the system under no stress at 40 $\overset{\circ}{K}$, i.e. the cut off range was chosen to be $r_c^2 = 4.95\ \sigma^2$. Usually the cut off range should be chosen to be less than half of the simulation cell size in order to avoid the unphysical interaction between a particle and its own images. Although our cut off range does not satisfy this criterion in the case of the 32 particle system, the results for the 108 particles system showed that the effect is not significant, at least at the rather low temperature of 40 $\overset{\circ}{K}$ (melting point of argon system is about 110 $\overset{\circ}{K}$).

The simulations started with a perfect fcc lattice configuration i.e., the particles were placed on the lattice sites and the $\underline{\underline{h}}$ matrix describing the unit cell for 32 particle system was:

$$\underline{\underline{h}} = \begin{bmatrix} 3.222 & 0 & 0 \\ 0 & 3.222 & 0 \\ 0 & 0 & 3.222 \end{bmatrix} \qquad (5.1)$$

The values of the elements of matrix $\underline{\underline{h}}$ are the values found for the perfect system at 40 $\overset{\circ}{K}$ and zero external pressure in Chapter 3. These initial values do not have to be exactly the equilibrium values. In general, they could be any values if all the interaction neighbors are considered in evaluating the total potential energy of the system. In cases where the interaction potential between the particles is truncated at some distance or there are discontinuities in the potential function, as it is the case in all the dynamical simulation studies, these values must be close to or smaller than that of the equilibrium values so that the number of particles which are neighbors to each particle in the system with the initial $\underline{\underline{h}}$ is more than or equal to the corresponding number in the equilibrium condition. The bookkeeping of neighbor particles as simulation goes on is made by the method described by Deutsch [D75].

The δ parameters defined in Section 2.7 throughout the simulations were:

$$\underline{\underline{\delta}}^{h} = \begin{bmatrix} .03\sigma & .03\sigma & .03\sigma \\ & .03\sigma & .03\sigma \\ & & .03\sigma \end{bmatrix} \qquad (5.2)$$

$$\delta = .28\sigma$$

where σ is the Lennard-Jones parameter. Throughout the simulations the internal stresses were calculated in order to monitor the equilibrium between internal and external stresses. Also the pair correlation function and snapshots of the particles were calculated to confirm the crystal structure which in the first place was predicted from the relationship between the unit cell dimensions.

5.2.1 System Under Compressive Load

A uniaxial compressive stress along [001] direction was applied on the system. Under the action of such a load the matrix $\underline{\underline{h}}$ started to change in a well-defined manner, as expected, by a contraction in the [001] direction and expansion in the [100] and [010] directions, while deforming homogeneously and preserving its face centered tetragonal structure ($h_{22}=h_{33}$ and $h_{12}=h_{13}=h_{23}=0$) to a high degree of accuracy. All runs were made for 5000-7000 steps/particle where the first 1000 steps/particles were discarded as the equilibrium period. This was long enough to let the system reach equilibrium as could be seen from the variation, say, of $\underline{\underline{h}}$, as the simulation proceeds. The ensemble averages were calculated over the last 4800-6000 steps/particle. One could get a better statistical error by averaging over a longer time. The standard deviation of the element h_{11} of the matrix $\underline{\underline{h}}$ at the compressive stress of 200 bar was 0.15%.

The responses of the 32 particles system at 40 $\overset{\circ}{K}$ to the compressive load 150, 200, and 300 bar were calculated. The simulation for the system under 300 bar was also carried out on the 108 particle system and as it was mentioned earlier, no significant difference between the 32 and 108 particles system was observed (for example at the

compression of 200 bar $\frac{h11}{2}$ was 1.54 (1 $\pm$ 0.15%) for the 32 particles system and $\frac{h11}{3}$ was 1.54 (1 $\pm$ 0.12%) for the 108 particle system). At the300 bar load, after 6000 steps/particles, the load on the 32 particle system was reduced to 200 bar. The results were the same as those of 200 bar previously found, and then after another 4000 steps/particle the 200 bar load was removed the system went back to its original fcc structure. The 300 bar load was also removed from the 108 particle system and it also went back to its original fcc structure. The results are shown in Figs. 5.6 and 5.7.

5.2.2 Structure Transformation Under Compression (fcc→hcp)

When the compressive load was increased to 400 bar, the system behavior changed markedly. In the new structural equilibrium the system was not tetragonal any more, and a careful analysis of the snapshots showed that the new structure was a deformed hcp. When the load was removed either suddenly or in two steps, the system did not return to the fcc structure, instead the hcp structure was obtained. The $\underline{\underline{h}}$ for the hcp structure was

$$\underline{\underline{h}} = \begin{bmatrix} 3.732 & 0 & 0 \\ 0 & 3.952 & 0 \\ 0 & 0 & 2.260 \end{bmatrix} \qquad (5.3)$$

which corresponds to an hcp structure whose closed packed planes (0001) are parallel to the (010) planes of the fcc structures. The [0001] axis in this case was parallel to the load direction. An hcp structure with the above orientation has the dimensions:

$$h_{11} = c = \sqrt{\frac{8}{3}}\ a$$
$$h_{22} = \sqrt{3}\ a \qquad (5.4)$$
$$H_{33} = a$$
$$h_{ij} = 0 \quad i = j$$

where a is the nearest neighbor distance of the perfect hcp system at 40 °K. The changes in size and shape associated with this transformation are shown in Fig. 5.2

The $\underline{\underline{h}}$ matrix found for 350 bar was used as initial value to study the response of the hcp structure as the load is increased. The results of the system under 450, 550, and 600 bar are shown in Fig. 5.6 and 5.7. As it can be seen from Fig. 5.6, the new structure is very hard to compress. This is expected since the load direction and closed packed planes are parallel.

The transformation mechanism [P81] is depicted in Fig. 5.3. Two adjacent planes (010) of the perfect fcc system in Fig. 5.3a is deformed to that of Fig. 5.3b as the compressive load is increased, beyond 300bar the structure changes to that shown in Fig. 5.3c. This change is accomplished by the sliding of the alternative planes (010). After the transformation has occurred, the dimensions of the unit cell in the directions [010] and [100] were not the same as they were before the transformation. Notice that this fcc→hcp transformation is not the one that can be found by shuffling of closed packed planes. In the

(-A-B-C-A-B-C-) is transformed to the hcp structure (-A-B-A-B-) such

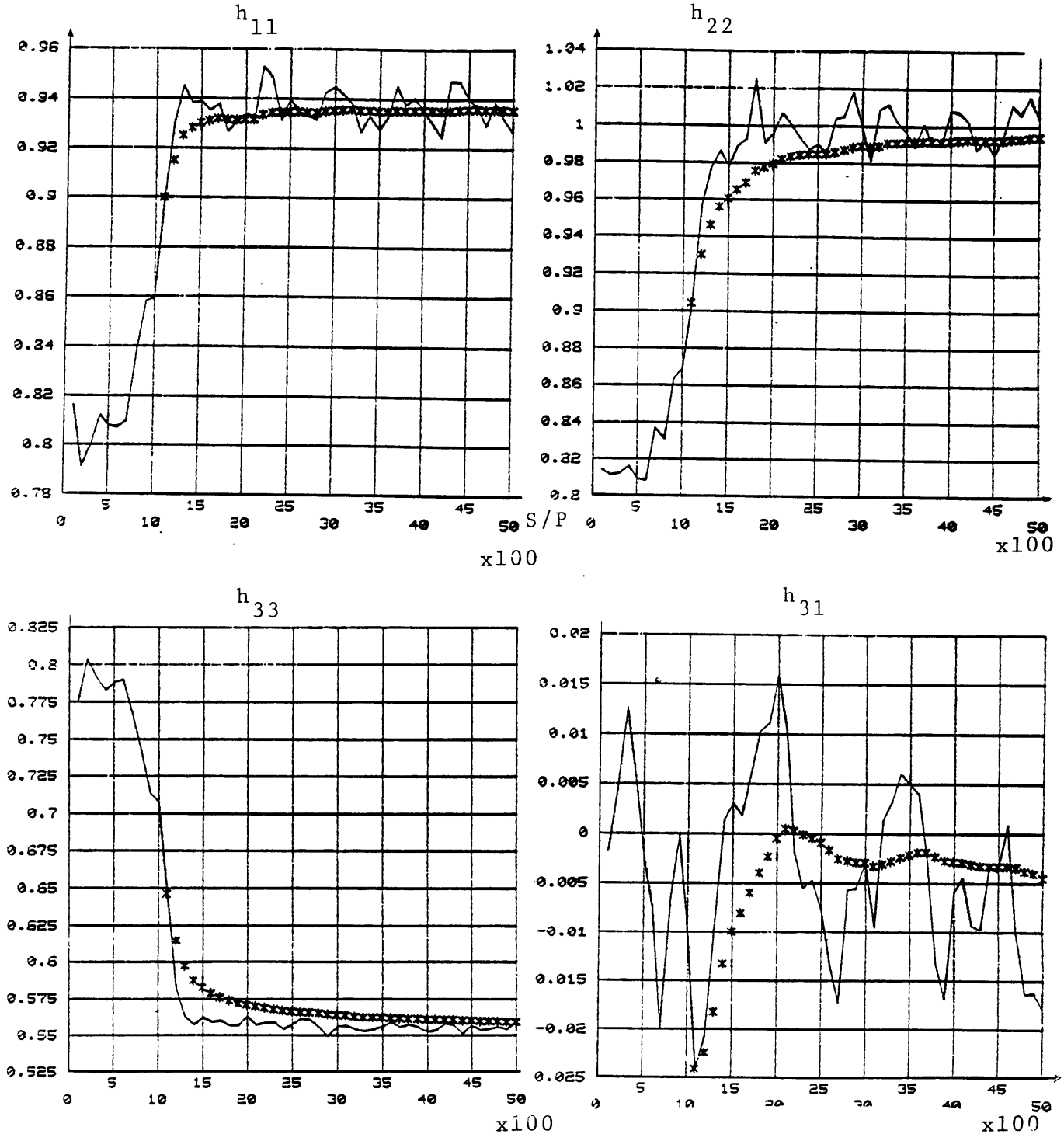

Fig. 5.2 Components of matrix $\underline{\underline{h}}$ as afunction step/particle under the critical compressive load of 350 bar and the temerature of 40 °K (fcc→ hcp). solid line shows instantaneous value and * shows average value of $\underline{\underline{h}}$ components.

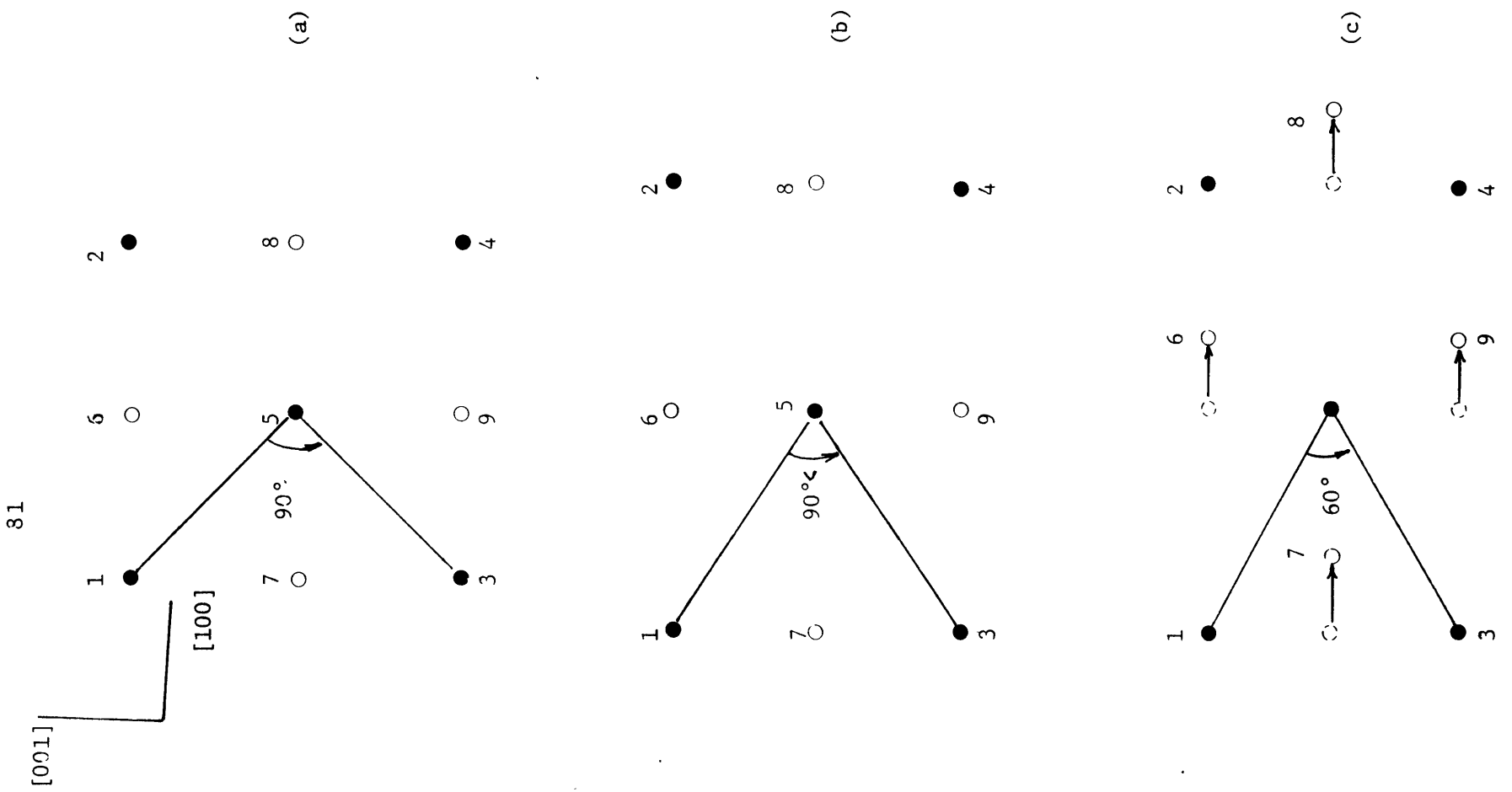

Fig. 5.3 Two plane of an fcc structure perpendicular to [001] direction are showen by open and closed circles respectively. (a)-(b) shows how the face centered square structure changes to a triangular lattice on suitable compression in the [001]. (b)-(c) shows the necessary translation of the ○ plane to achieve hcp ordering.

that the closed packed planes have the same orientation in both structures. In the transformation observed here the closed packed planes in fcc structure are normal to the [111] direction and those of hcp are normal to the [010] direction.

5.2.3 System Under Tensile Load

The uniaxial tensile load along the [001] direction was applied to the system to study its behavior under tension. The simulation again started with the perfect fcc configuration and tensile loads of 100, 200, 400, 500, and 600 bar were applied on the 32 particle system and 100, 500, and 600 bar on the 108 particle system. Again the results for both systems were the same within the statistical uncertainty. The system behavior was, as it is expected, elongation in the [001] direction and contraction in the [010] and [100] directions. Under this range of stress the structure was face centered tetragonal to within high accuracy; for example, at the tensile load of 400 bar the average values of the elements of $\underline{\underline{h}}$ were $h_{11} = 3.324\ (1 \pm .15\%)$, $h_{22} = h_{33} = 3.188\ (1 \pm .15\%)$ and $h_{12} = h_{13} = h_{23} = 3.22\ (0 \pm .2\%)$.

As the tensile load was increased beyond 600 bar the system was not able to maintain a stable configuration. The elements of matrix $\underline{\underline{h}}$, which describes the shape of the system, were diverging as the simulation proceded. shown in Fig. 5.4. We can conclude that the theoretical tensile strength of the argon system at the temperature 40 $\overset{\circ}{K}$ is 600 bar. This value of the critical load is much smaller than the reported static calculation value of 3700 [M72][b] and 2100 bar found in Chapter 4. by static calculation. Therefore, heating

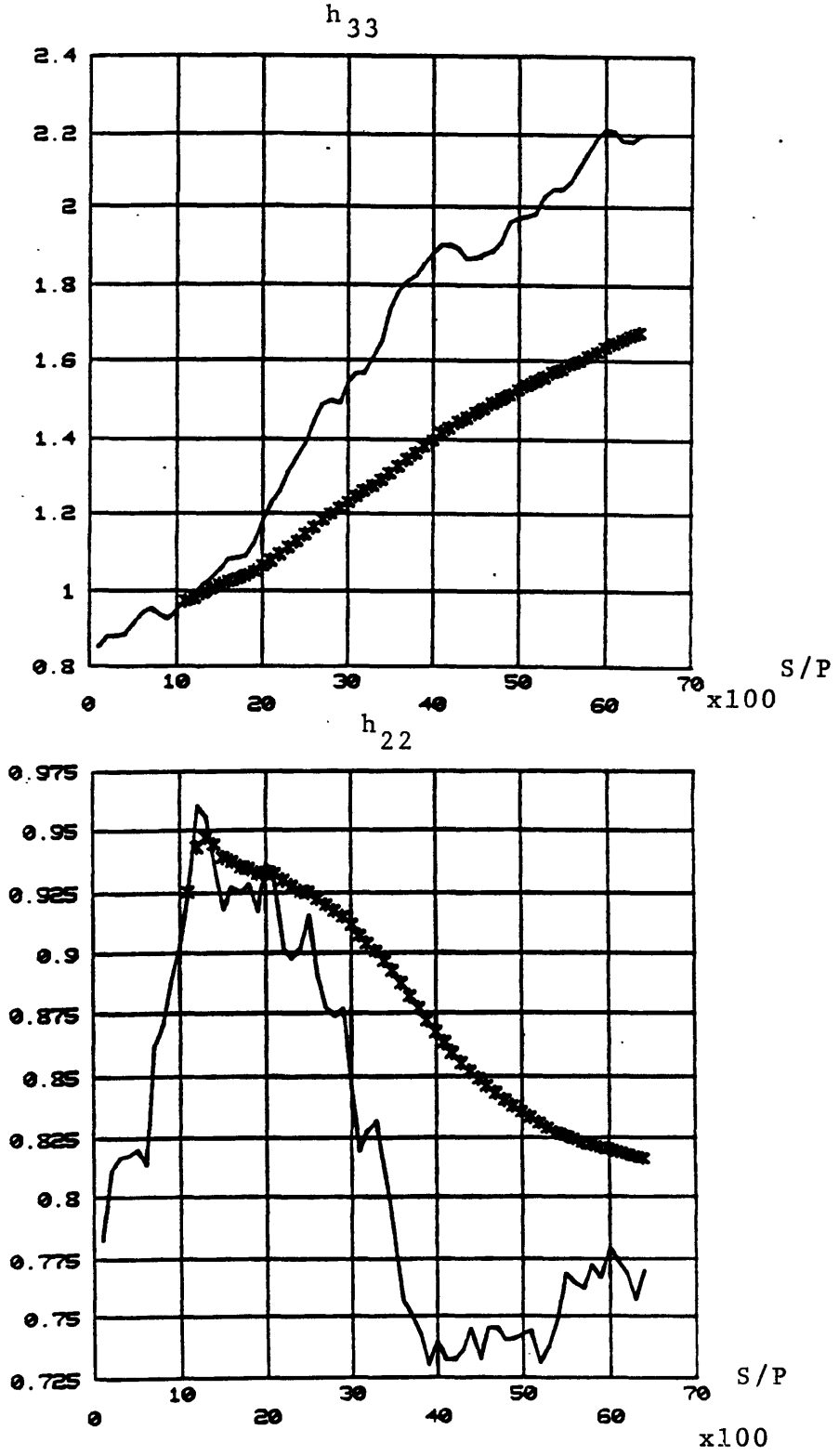

Fig. 5.4 Components of matrix $\underline{\underline{h}}$ as a function of step/particle under the critical tensile load of 650 bar at 40 °K for argon crystal. solid line shows instantaneous $\underline{\underline{h}}$ and * shows average $\underline{\underline{h}}$. Divergances of $\underline{\underline{h}}$ components show system failure.

Fig. 5.4 (cont'd)

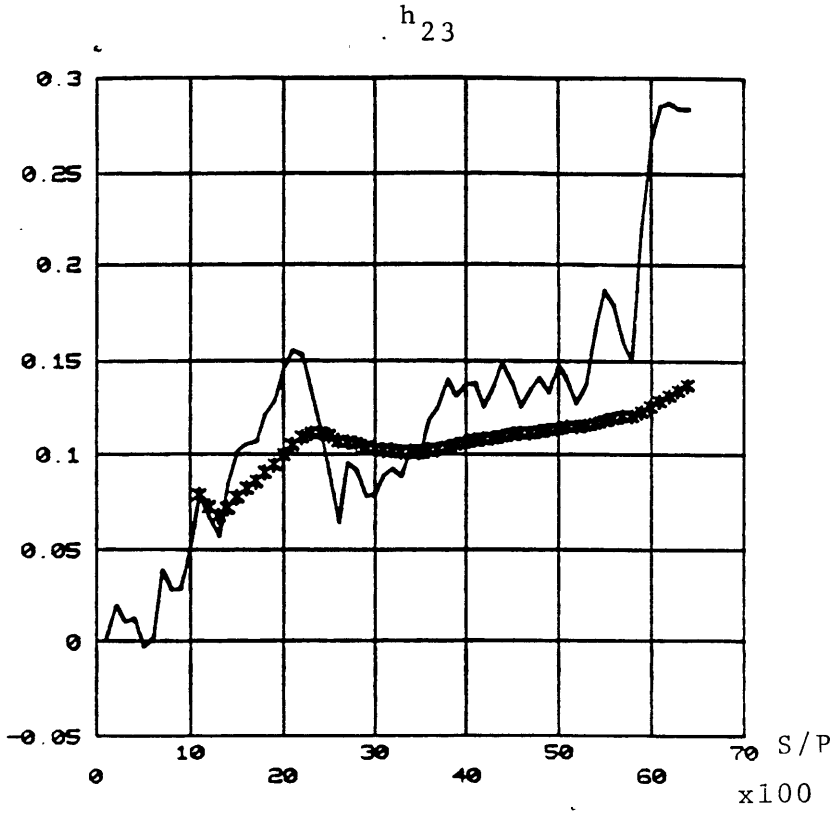
h_{23}
0.3
0.25
0.2
0.15
0.1
0.05
0
-0.05
0
10
20
30
40
50
60
70
S/P
x100

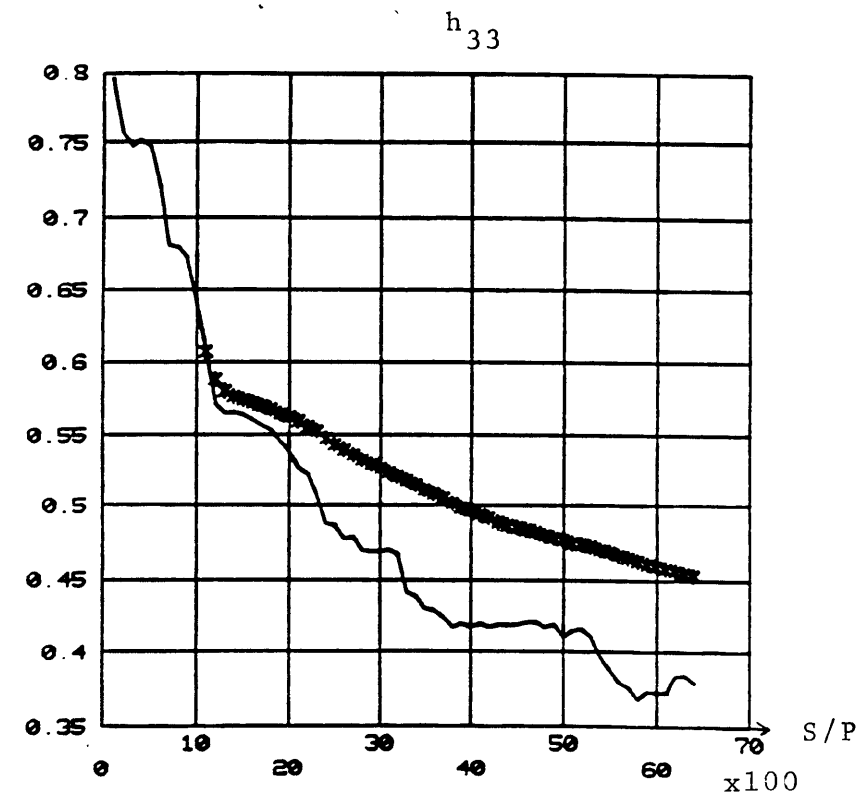
h_{33}
0.8
0.75
0.7
0.65
0.6
0.55
0.5
0.45
0.4
0.35
0
10
20
30
40
50
60
70
S/P
x100

up the argon system from zero temperature to 40 $\overset{\circ}{K}$ apparently causes the theoretical tensile strength to drop about by a factor of 3.5. The lattice constants at zero and 40 $\overset{\circ}{K}$ are 1.573σ (Chapter 4) and 1.611 σ respectively. This means that at 40 $\overset{\circ}{K}$ the thermal strain is 2.42%. Notice that this is only the average strains while the instantaneous strain is fluctuating about this value. The system fails when the instantaneous strain along the load direction [001] becomes greater than the critical strain value. If we assume the critical strain value is the one found in Chapter 4 by static calculation, i.e. 11.5%, then the difference of the theoretical tensile strength at 0 and 40 $\overset{\circ}{K}$ could be explained partly because at 40 $\overset{\circ}{K}$ there is an additional 2.42% average thermal strain. This means for the same total average strain the system at 40 $\overset{\circ}{K}$ is under lower stress, and partly because the system fails when the instantaneous strain value is greater than critical strain no matter if the average strain is not greater than the critical value.

5.2.4 Stable Structure Under No Stress

It has been predicted [B24] that an fcc to bcc transformation is possible under compression. Since such a transformation was not observed in our simulation, it is important to determine if the reason was because the fcc→hcp transition occurs first or the fcc→bcc transformation does not occur at all. A simulation was started with the corresponding size of a bcc structure under no stress, i.e. the initial matrix $\underline{\underline{h}}$ was:

$$\underline{\underline{h}} = \begin{bmatrix} 3.617 & 0 & 0 \\ 0 & 3.617 & 0 \\ 0 & 0 & 2.557 \end{bmatrix} \qquad (5.5)$$

The system was unstable and quickly went to the fcc structure. This observation confirms the static calculation result of Chapter 4 that predicts there is no bcc structure which could be stabilized by the Lennard-Jones potential.

5.2.5 Stress-Strain Curve

The strain as a function of applied stress for the argon system is shown in Fig. 5.5 along with the Macmillan's static calculation [M72] and the one also calculated by the static method in Chapter 4. As it is seen from the Fig. 5.5,the effect of the temperature is small at low stress ($\leq \pm 100$ bar) but it becomes significant at higher stresses. This shows that the static calculation, which is valid at zero temperature, is a good approximation at low stresses for the system at finite temperature.

At low stresses the stress-strain relationship is $\sigma = \underline{\underline{c}}\ \underline{\varepsilon}$ where

$$\underline{\sigma} = \begin{bmatrix} \sigma_{xx} \\ \sigma_{yy} \\ \sigma_{zz} \\ \sigma_{xy} \\ \sigma_{xz} \\ \sigma_{yz} \end{bmatrix} \qquad \underline{\varepsilon} = \begin{bmatrix} \epsilon_{xx} \\ \epsilon_{yy} \\ \epsilon_{zz} \\ \epsilon_{xy} \\ \epsilon_{xz} \\ \epsilon_{yz} \end{bmatrix} \qquad (5.6)$$

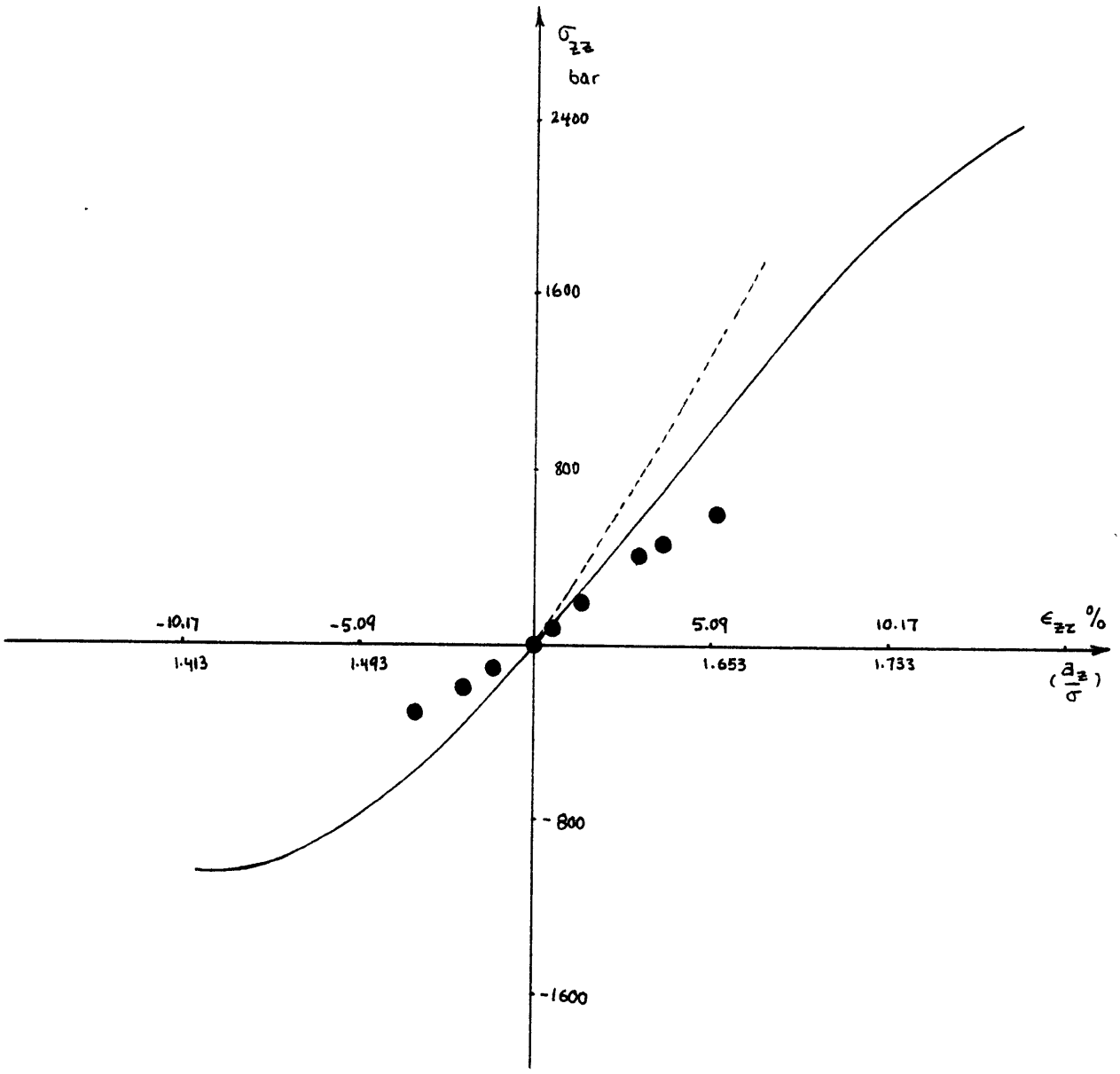

Fig. 5.5 Stress-strain under uniaxial load for truncated Lennard Jones potential. Solid line is the static calculation, the dashed line is Macmillan's results and closed circles are Monte Carlo results at T=40°K.

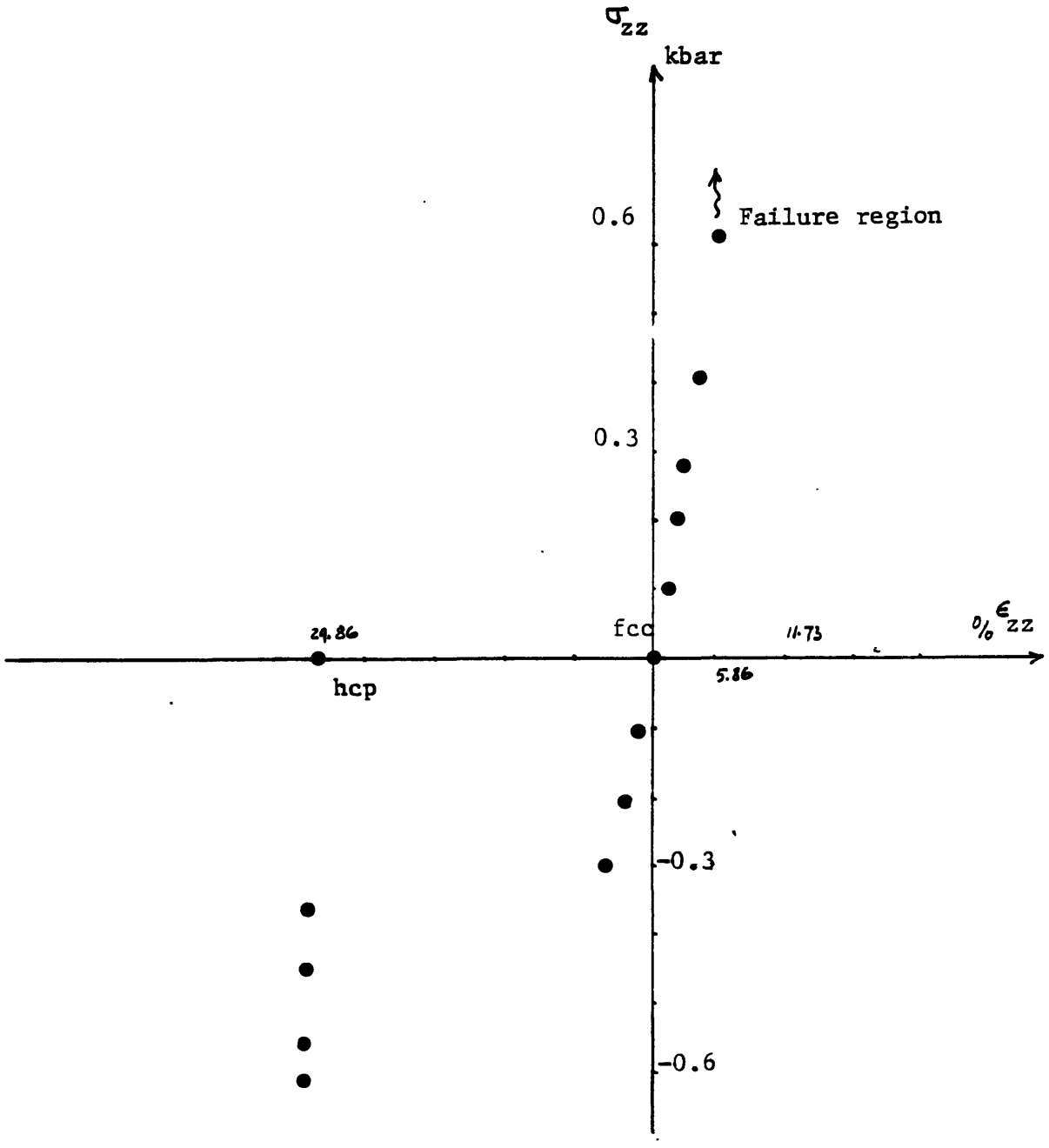

Fig. 5.6 Calculated strain ϵ_{zz} as a function of applied stress σ_{zz} for the fcc structure of argon at 40 °K. The jump in strain under compression corresponds to (fcc→hcp) transformation(the reference is fcc under no stress).

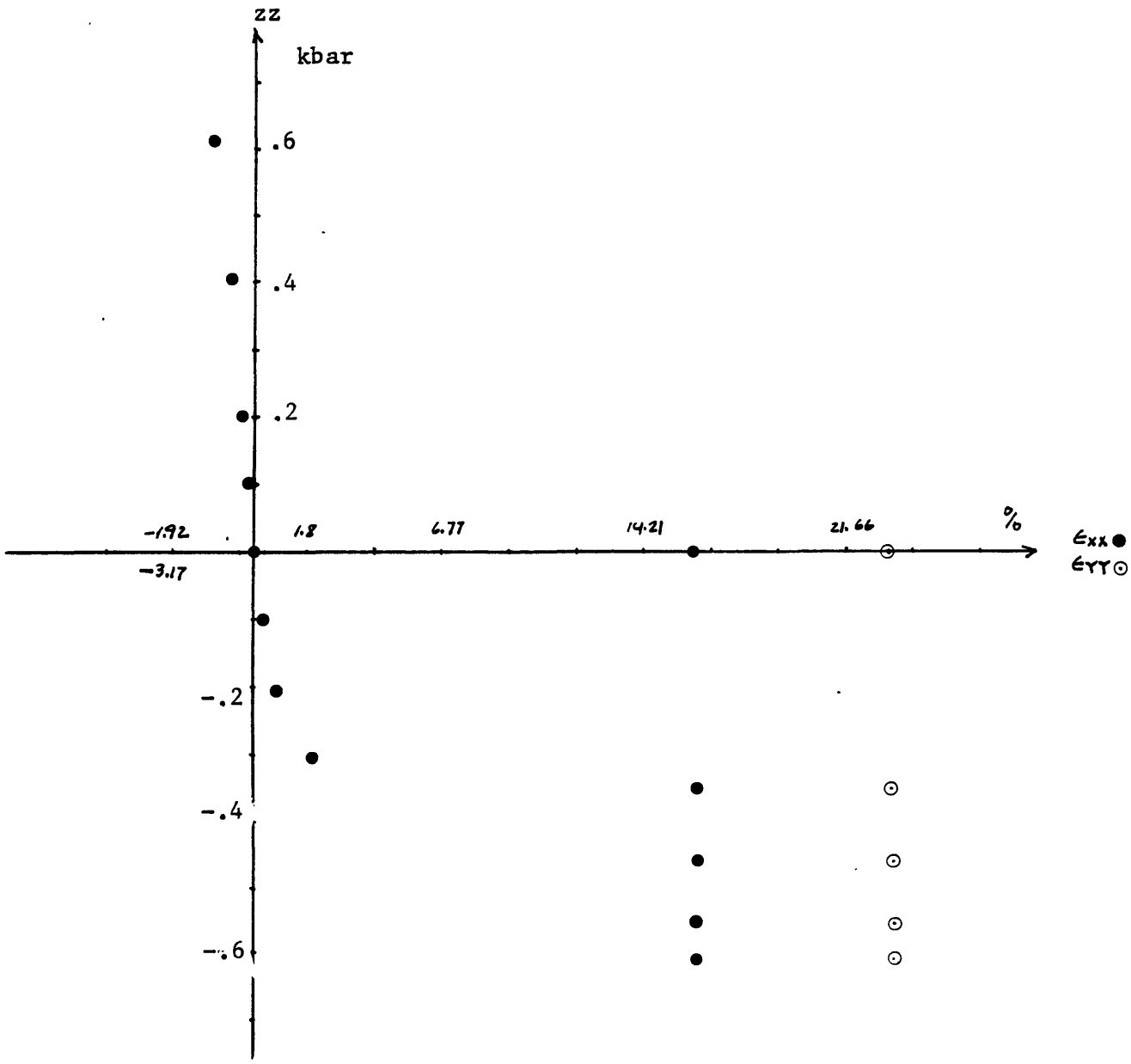

Fig. 5.7 Calculated strains ϵ_{xx} and ϵ_{yy} as a function of applied stress σ_{zz} for the fcc structure of argon at 40 °K. The strains ϵ_{xx} and ϵ_{yy} are the same in deformed fcc while they are different in deformed hcp(reference system is fcc under no stress).

For a cubic system the elastic constant matrix $\underline{\underline{c}}$ is:

$$\underline{\underline{C}} = \begin{bmatrix} C_{11} & C_{12} & C_{12} & 0 & 0 & 0 \\ C_{12} & C_{11} & C_{12} & 0 & 0 & 0 \\ C_{12} & C_{12} & C_{11} & 0 & 0 & 0 \\ 0 & 0 & 0 & C_{44} & 0 & 0 \\ 0 & 0 & 0 & 0 & C_{44} & 0 \\ 0 & 0 & 0 & 0 & 0 & C_{44} \end{bmatrix} \tag{5.7}$$

In the fcc system under uniaxial load i.e.,

$$\sigma_{xx} = \sigma_{yy} = 0 \quad , \quad \sigma_{33} = \sigma_0$$
$$\sigma_{xy} = \sigma_{x3} = \sigma_{y3} = 0 \tag{5.8}$$

the structure was always face centered tetragonal i.e.

$$\epsilon_{xx} = \epsilon_{yy} = \epsilon_1 \quad ; \quad \epsilon_{33} = \epsilon_0$$
$$\epsilon_{xy} = \epsilon_{xy} = \epsilon_{y3} = 0 \tag{5.9}$$

Substituting Eqs. (5.8) and (5.9) into $\underline{\sigma} = \underline{\underline{c}}\ \underline{\epsilon}$ one obtains:

$$\frac{\sigma_0}{\epsilon_0} = (C_{11} - C_{12})(C_{11} + 2C_{12}) \Big/ (C_{11} + C_{12})$$

$$\frac{\sigma_0}{\epsilon_1} = -(C_{11} - C_{12})(C_{11} + 2C_{12}) \Big/ C_{12} \tag{5.10}$$

The right hand sides of Eq. (5.10) are the slopes of strain-stress curves. Substituting these slopes into Eq. (5.10) the elastic constants for the simulation and static calculation were calculated. The elastic constants c_{11} and c_{12} calculated by different methods are given in Table 5.1

	c_{11} (kbar)	c_{12} (kbar)
MacMillan's	33.28	15.66
Squire's	28.4	16.1
Static Cal.	33.23	19.98
Simulation	28.99	21.26

Table 5.1 Elastic Constants Calculated by Different Methods

The Macmillan's elastic constants are for the Lennard-Jones potential and the Squire's are the conventional Monte Carlo results for 108 particles system at 40 $^{\circ}$K with the Lennard-Jones potential [to within a good approximation], while the last two rows in Table 5.1 are the results for a truncated Lennard-Jones potential. Therefore the temperature effect could be seen from the changes in elastic constants in row 1 to row 2 and in row 3 to row 4 in Table 5.1 which is a decrease of 17.7 to 12.8% in c_{11} and an increase of 2.8 to 6.4% in c_{12}. Also the effect of cutting off the potential at some distance can be seen by comparing row 1 with row 3 and row 2 with row 4 which is significant in the elastic constant c_{12} and negligible in the elastic constant c_{11}.

The isothermal bulk modulus can be written [S69] as

$$B^T = \frac{1}{3} (C_{11} + 2 C_{12}) \qquad (5.11)$$

which is valid only at zero pressure. Then the B^T for our simulation results in 16.75 kbar whereas the experimental value at 40 $^{\circ}$K is

21.74. units. The calculated B^T is lower by 6%. This means that including long range interaction improves the results. There are no experimental values for the isothermal elastic constants [S69[b]], so a direct comparison between calculated and experimental isothermal elastic constants for the argon system is not possible at this point.

5.3 Study of Iron Crystal Under Uniaxial Load

5.3.1 Simulation Model

The system used to carry out the calculations consisted of 32 classical particles in a perfect 3-dimensional crystal lattice with the flexible border condition described in Chapter 2. The particles interact through a short range, empirical potential called Johnson I shown in Fig. 5.8. As can be seen from Fig. 5.1, the [100], [010], and [001] directions for the fcc structure are taken to be along the coordinate axes. The [100], [010] and [001] directions for the bcc structure are the [100], [010] and [001] directions for rotated by 45° in the xy plane.

The optimized matrix $\delta\underline{\underline{h}}$ and δm determined by the method described in Section (2.6) have the following values:

$$\underline{\underline{\delta}}^4 = \begin{bmatrix} 0.036 & 0.009 & 0.009 \\ & 0.036 & 0.009 \\ & & 0.036 \end{bmatrix}, \quad \delta_m = .020 \qquad (5.12)$$

Throughout the simulations the temperature and pressure were kept at 70 °K and zero respectively. The internal stresses were calculated to monitor their balance with the externally applied stresses.

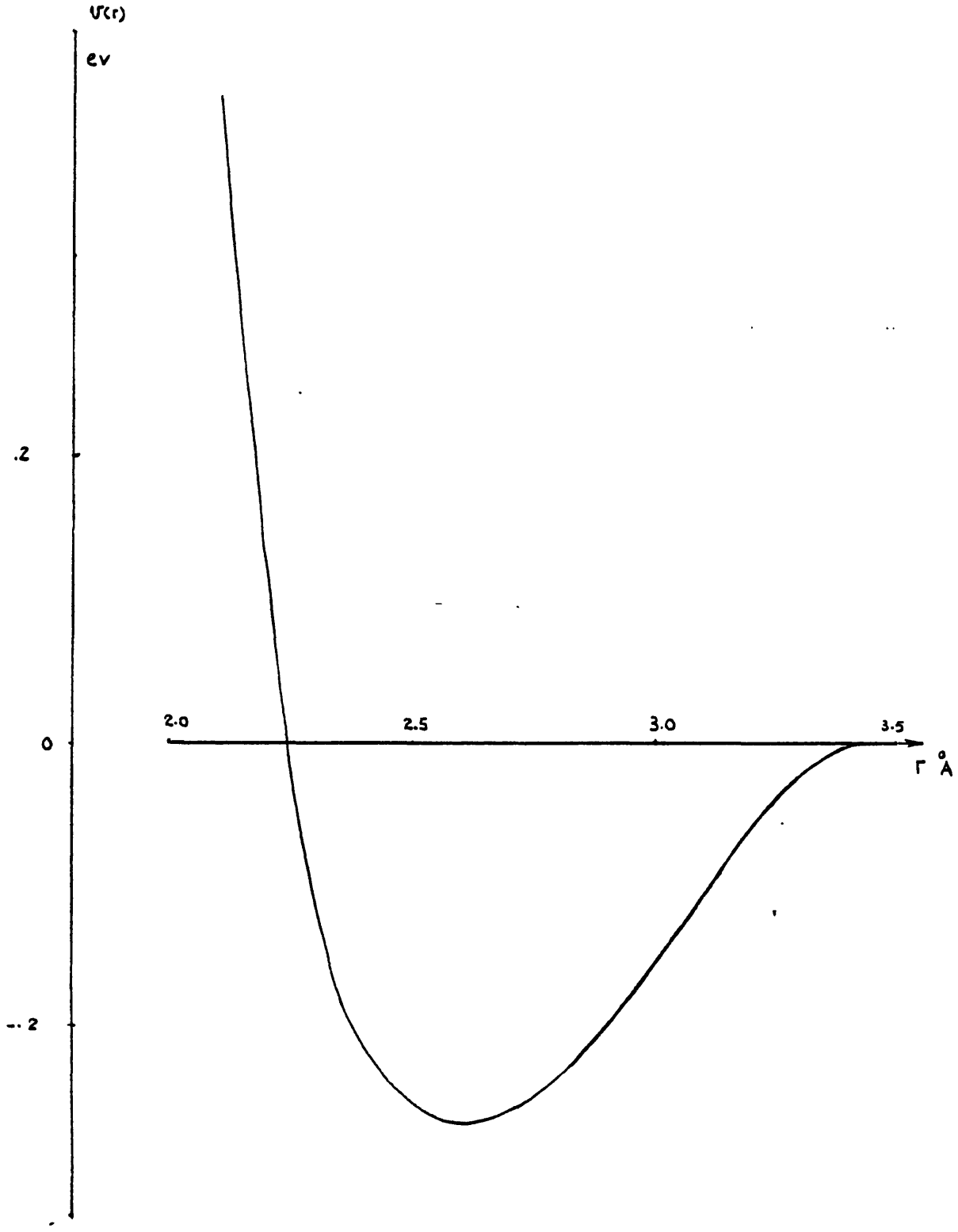

Fig. 5.8 Johnson potential; potential energy as a function of interatomic distance.

The pair correlation function and snapshots of particles were also calculated to confirm the structure of the system found from the equilibrium value of matrix $\underline{\underline{h}}$.

5.3.2 BCC Crystal Under Uniaxial Load

The simulation started with the system in a perfect lattice configuration. The corresponding matrix $\underline{\underline{h}}$ describing the simulation cell of 32 particles being:

$$\underline{\underline{h}} = \begin{bmatrix} 8.09 & 0 & 0 \\ 0 & 8.09 & 0 \\ 0 & 0 & 5.72 \end{bmatrix} \text{ Å} \qquad (5.13)$$

where this corresponds to a bcc structure with lattice constant 2.86Å found in Chapter 4. The system responses to uniaxial compressive and tensile loads applied along the [001] direction up to $5.5 * 10^{10}$ dyn/cm^2 and $6.0*10^{10}$ dyn/cm^2 were calculated respectively. As the tensile (compressive) load was increased the bcc structure expanded (contracted) in the [001] direction and contracted (expanded) in the [010] and [100] directions (by the same amount) such that the angles between the a, b, and c vectors (see Section 2.2) remained at 90° to within an accuracy of $\pm$.01°. The results are summarized in Fig. 5.9.

The simulation results at the relatively low temperature of 70°K are in good agreement with the static calculation of Chapter 4, see Fig. 5.10. Also the results are in good agreement with the experimental

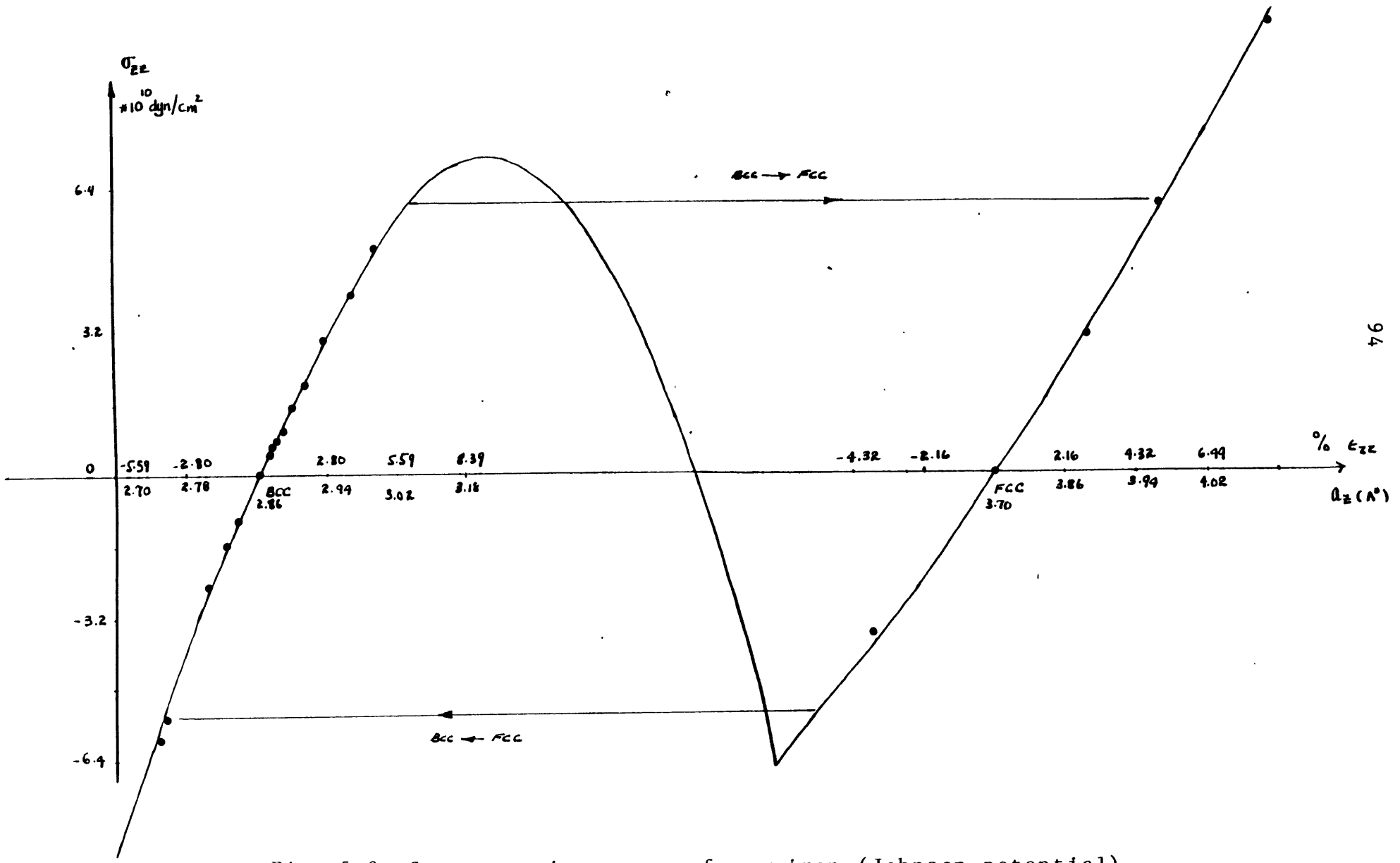

Fig. 5.9 Stress-strian curves for ∝ iron (Johnson potential). Solid line is the static calculation and points indicate Monte Carlo simulation results at 70° K. Transformations (bcc→fcc) and (fcc→bcc) under uniaxial loads are shown on the curve for T=70°K.

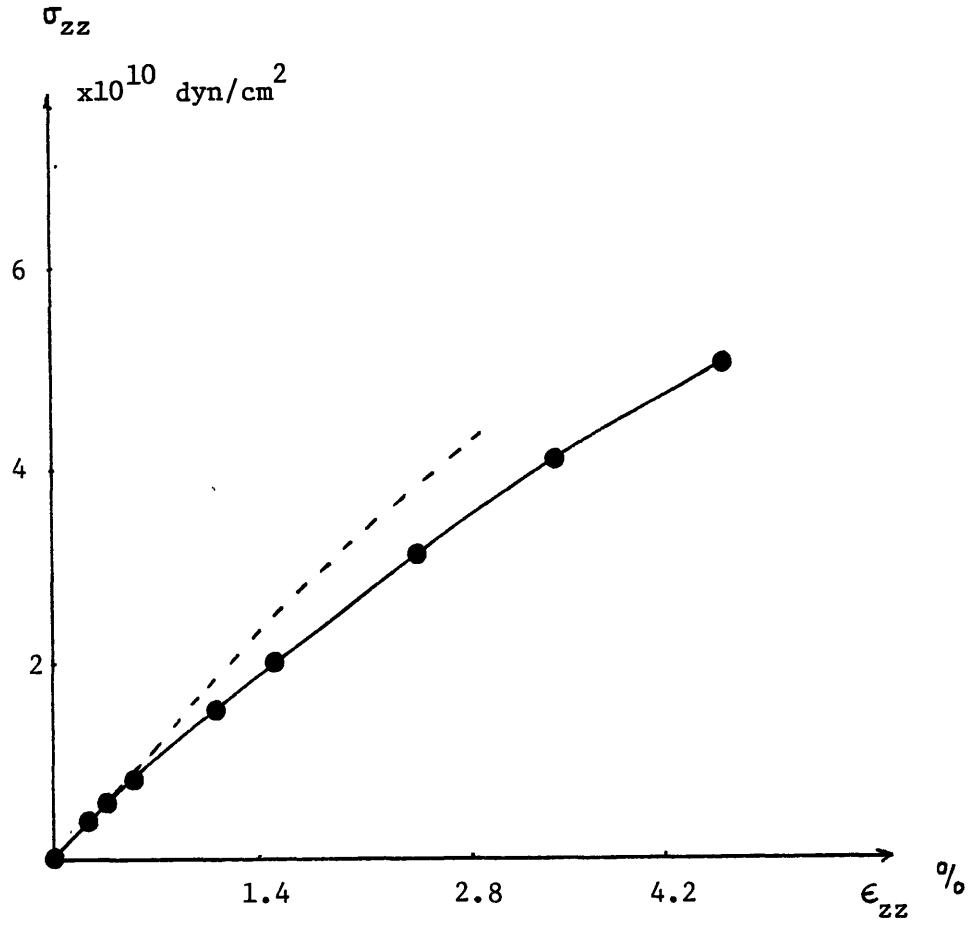

Fig. 5.10 Calculated and experimental stress-strain curves for ∝ iron (Johnson potential). Solid line is static results, is Monte Carlo results and dashed line is the experimental results.

data [B56]^{b} of a 3.8μ diameter whisker of α iron up to $1.0*10^{10}$ dyn/cm^2. The experimental data is at room temperature (∿300K°). The temperature difference between experimental and simulated data will lower further than the $1.0*10^{10}$ dyn/cm^2 stress because of thermal motions, as it was explained in the case of the argon system. Above the $1.0*10^{10}$dyn/cm^2 tensile stress the discrepancy rises as the stress increases and at $4.0*10^{10}$ dyn/cm^2 the calculated strain is larger than the experimental value by 12% (not including the temperature difference effect), see Fig. 5.10.

5.3.3 Structural Transformation Under Tension (bcc→fcc)

At a tensile load of $6*10^{10}$dyn/cm^2 the bcc structure transformed into a deformed fcc (face centered tetragonal). The load was then decreased to $3*10^{10}$dyn/cm^2 and then to zero. At zero load the system was found to be a perfect fcc structure. This first was seen from the matrix $\underline{\underline{h}}$ given in Eq. (5.13) and was confirmed by the snapshots of the particles.

$$\underline{\underline{h}} = \begin{bmatrix} 7.4 & 0 & 0 \\ 0 & 7.4 & 0 \\ 0 & 0 & 7.4 \end{bmatrix} \quad A° \qquad (5.14)$$

This corresponded to a fcc structure with the lattice constants of 3.70A°. This value turned out to be greater than the experimental value[L61] of 3.55A° by 4.2%. The difference is due to the potential used to describe the interatomic interaction, because the Johnson I potential is originally being constructed from the experimental lattice constant and elastic constants of (bcc) iron.

The critical loading of $6.0*10^{10}$dyn/cm^2 at which the bcc→fcc transformation occurs is less than that given by the static calculation, $9*10^{10}$dyn/cm^2 in Chapter 4. The reason for such a difference is explained in terms of thermal contribution to the total strain and the fact that the transformation occurs when the instantaneous strain is greater than the critical strain. This was described in the case of the argon system failure in Section 5.2.2. The potential energy or enthalpy of the system (the pressure is zero) in this transformation is increased from -48.46 to -47.66ev (in zero temperature from -48.4 to -47.53ev), see Fig. 5.12. Therefore this transformation cannot be explained in terms of the free energy concept. What happens is that the bcc structure cannot at the same time keep its body centered tetragonal symmetry and also match the internal and external stresses, or in other words, there is no body centered tetragonal structure that could have internal stress of $6*10^{10}$ at 70°K ($9*10^{10}$dyn/cm^2 at zero temperature) along [001] direction. Thus the system at the critical stress is mechanically unstable and it will seek another structure, in this case a face centered tetragonal, which could have such an internal stress regardless of the potential energy being increased. In Fig. 5.11 potential, internal stress along the load direction and some elements of matrix $\underline{\underline{h}}$ are shown as the transformation occurs.

5.3.4 Structural Transformation Under Compression

The fcc structure found in Section 5.3.3 was subjected to tensile and compressive loads and the results are summarized in Fig. 5.9.

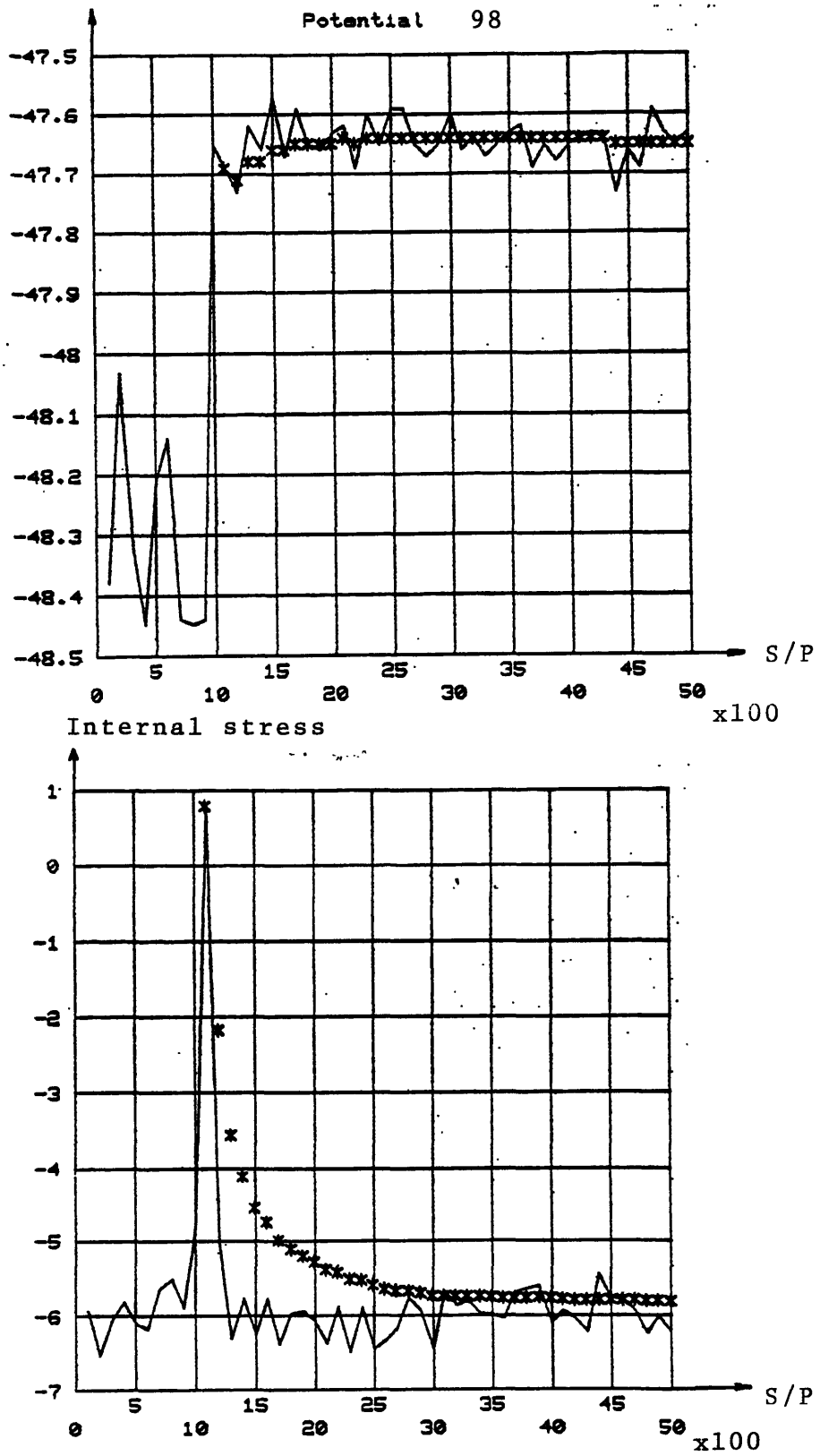

Fig. 5.11 Potential energy (a), Internal stress along the load (b) and diagonal elements of $\underline{\underline{h}}$ (c-e) as a function of step/particle for a system of 32 particles with Johnson I potetial at T=70°K and σ_{zz} =6*10^{10} dyn/cm^2 (tension) at which bcc→fcc transformation occurs. Solid line shows instanyaneous and * shows average value.

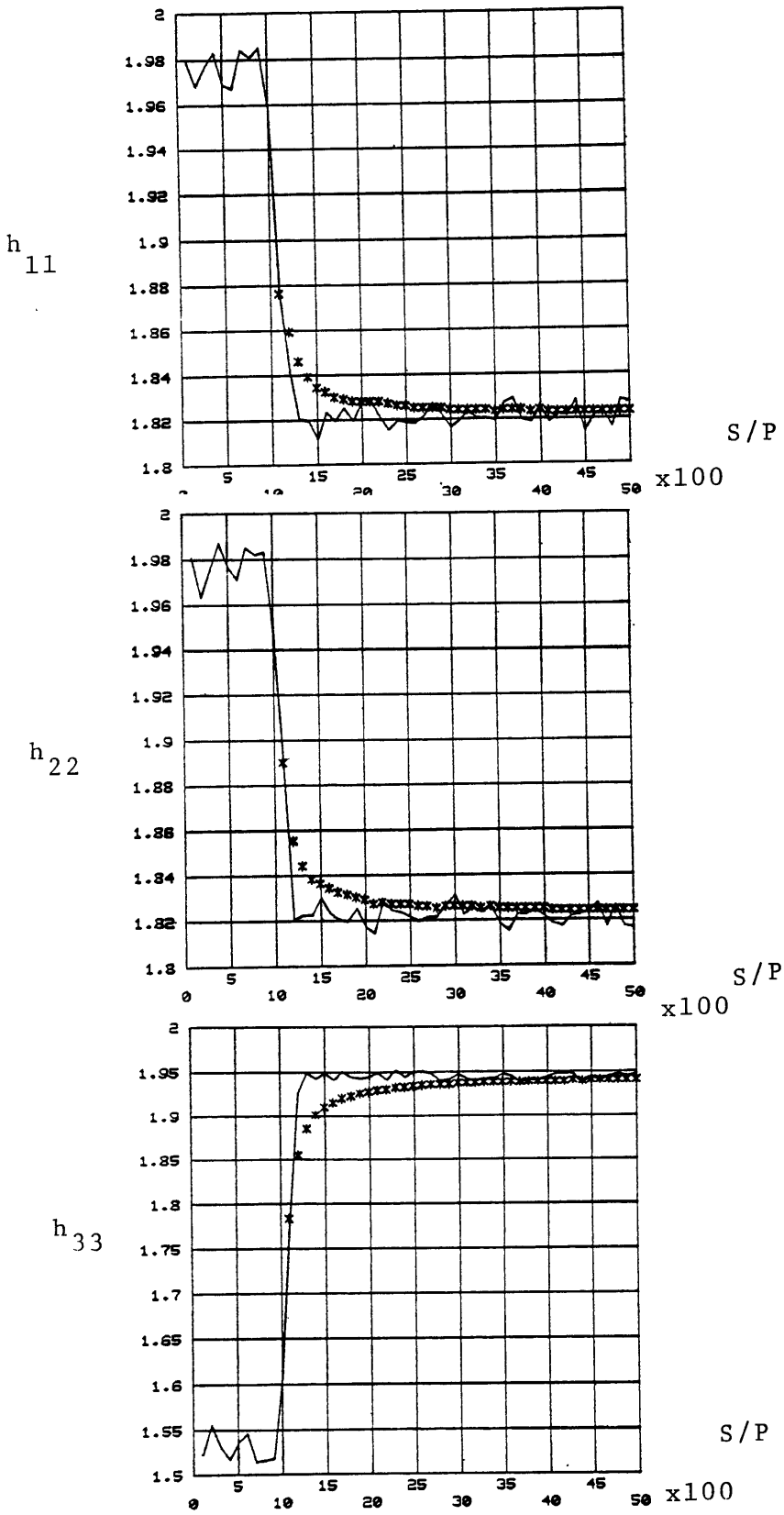

Fig. 5.11 (cont'd)

At compressive load of $5.5*10^{10}$dyn/cm^2 the fcc system transformed to a deformed bcc structure (body centered tetragonal structure). The load was then removed and the system went to a perfect bcc structure. Again the critical stress was smaller than the value of $7.74*10^{10}$dyn/cm^2 predicted by the static calculation in Chapter 4. Our explanation of this difference is also the thermal motion effect which was described in Section 5.2.2. In this transformation fcc→bcc at the critical stress the potential energy is decreased, in contrast to the bcc→fcc, from -47.53 to -48.65ev (from -47.65 to -48.93ev at zero temperature), see Fig. 5.12. Although in this case the transformation is energetically favorable, it is the mechanical instability, as explained in Section 5.3.3, that starts the transformation and the temperature effect that cause the critical stress to be reduced.

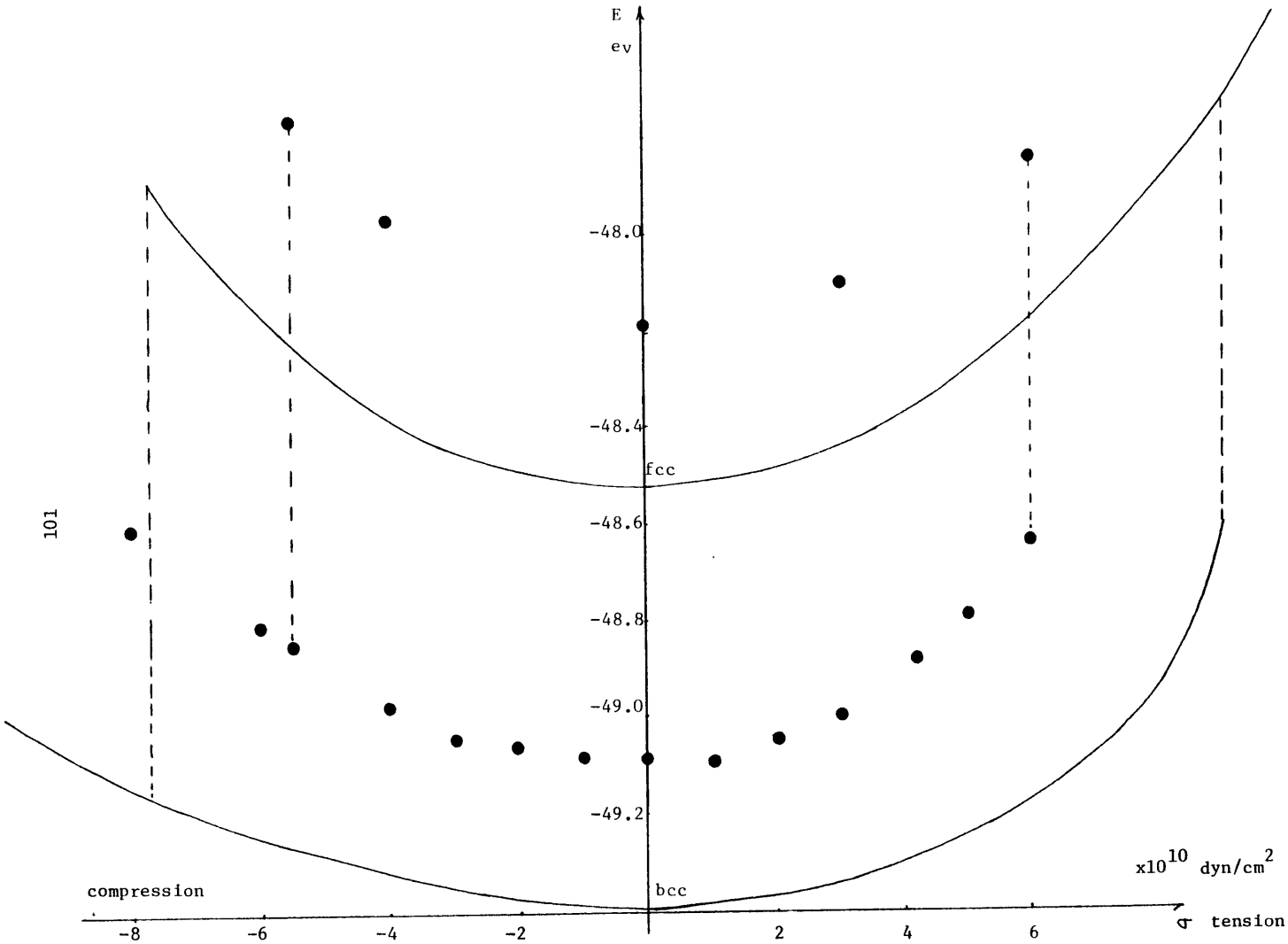

Fig. 5.12 Internal energy as a function of applied stress for iron. solid line is the static results and are Monte Carlo results at T= 70°K.

Chapter 6

Structure and Mechanical Responses of Bicrystals

6.1 Introduction

Most of the practical engineering materials are in the form of polycrystals; however, because of the simplicity of investigation and interpretation of results, scientific research is more widely conducted on single crystals. As might be expected, the properties of polycrystals are not always the same as those of single crystals of identical chemical composition and structure. The difference in properties arises from [P 75]:

(i) Factors that are inherent in the properties of individual grains, such as size and shape, and in the relationship between grains such as mutual orientation. Plastic properties of materials are especially sensitive to these factors.

(ii) Factors that are intrinsic properties of the boundary surfaces between individual grains, i.e., of the grain boundaries of polycrystalline materials. The basis of these properties is the fact that a grain boundary is essentially a region physically distinct from the grains that it binds. This region gives rise to such phenomena as grain boundary segregation, enhanced diffusion along the grain boundary, etc.

In general, the effects from the two contributions are difficult to distinguish, especially in the case of materials having complicated grain boundaries. It is much easier to distinguish between the effects due to the grain boundary itself and the effects due to interaction between grains when there are only two grains to deal with. For this reason, it is appropriate to study the behavior of bicrystals, i.e., two similar single crystals of arbitrary relative orientation bounded

together by a simple grain boundary.

Much progress has been made in the detailed understanding of low-angle grain boundaries. The dislocations model for a low-angle grain boundary is now well established [P75]. Knowledge of the properties of high-angle grain boundaries, however, remains to some extent incomplete. A large number of atomistic studies of grain boundaries (mostly high-angle) have been made in recent years and they are now one of the principal sources of our understanding of grain boundary properties, for reviews see [H76, V80]. The majority of atomistic studies has been carried out for coincidence site lattice boundaries. The coincidence site lattice grain boundary has a lower energy state than those non-coincidence boundaries with almost the same misorientation angle and also structural units of the boundary are inherently small in size and contain such a small number of atoms that the atomistic configuration in these units could be calculated by computer simulation more realistically than the non-coincidence site lattice grain boundary [W71].

There has been relatively few attempts [J70] so far to study the mechanical responses of a bicrystal to a uniaxial loading, and there is no study of the mechanical responses of a bicrystal to a shear loading. The experimental work has shown [L77] that the behavior of bicrystals under compression is significantly different from that of single crystals.

In this work we are interested in the mechanical behavior of a two dimensional bicrystal under uniaxial and shear loading. In the next section the system and the border condition used are described. It was found in section 6.3 that the bicrystal deforms more than the single crystal under unixial tensile and compressive loads normal

to the grain boundary plane (line). In section 6.4 the grain boundary movement was observed under shear loading when the load was greater than the critical value of 0.2 (dimensionless).

6.2 Bicrystal System and Border Conditions

The grain boundary system chosen for simulation study by our improved MC was a symmetric-tilt coincidence grain boundary with the reciprocal density of coincidence sites $\Sigma=7$, as is shown in Fig. 6.1. The thermodynamic properties of this system have been previously studied by molecular dynamics simulation [K78, C82]. The 56 particles in the system interact through the Lennard-Jones 12-6 potential with its cut off range being the midpoint between the second and third nearest neighbors. From the Fig. 6.1 it can be seen that the configuration is not a minimum energy configuration because the particles "2" and "56", and also "28" and "30" are too close to each other in the grain boundary core. The system therefore needs to be allowed to relax. There are different ways of relaxation [B82]. In this work we always started the simulations with the relaxed configuration found by Kwok [K78] for the same system. Ideally, when modeling a grain boundary a perfectly flexible border condition should be applied in every direction and it should act to give the same results as if the small grain boundary system were embedded in a large system, thus avoiding surface effects to as large an extent as possible. Among the variety of border conditions used in atomistic computer simulation the periodic border condition is commonly used for the small system size such as the one used here. However, the periodic border

in our system introduces an interesting artifact, namely, a second grain boundary at the border[B8$\hat{2}$]. This second boundary is crystallographically identical to the first one, but of opposite rotational sense [B8$\hat{2}$]. In conventional periodic border the shape and the dimensions of the simulation cell are predetermined and kept fixed throughout the simulation. This border condition is reasonable for simulating a perfect system, because the equilibrium shape and the dimensions of the system under any condition are known to a good extent. When simulating a system with defects in it, the equilibrium shape and dimensions of the system under any condition are not known in advance, for example in the grain boundary system sutdied here one may argue that the equilibrium simulation cell should have a rectangular shape due to the symmetry in the simulation cell. The simulation cell will end up being under an unknown stress field when the conventional border condition is used unless the right shape and dimensions are chosen. The flexible periodic border condition we have used here does not have such a problem. As it was mentioned in section (2.7), the simulation cell is described by three vectors (here two vectors). This border condition allows the simulation cell dimensions to expand or contract independently in different directions and even have a different shape. Of course these shapes are still constrained to be described by the two vectors. Another advantage of this border condition is that when the grain boundaries annihilate or when a particle is replaced by an impurity or is removed (see Chapter 7) the excess free area produced is removed from the simulation cell by adjusting the shape and the dimensions of the simulation cell whereas

in the conventional periodic border condition this free area, in the best case, is uniformly distributed throughout the simulation cell.

Starting with the relaxed configuration given by Kwok [K78] we first made two runs at tempertures of $T^* = 0.44$ and $T^* = .496$ ($T^* = \frac{T}{\varepsilon}$) and hydrostatic pressure of $p^* = 1.9744$ ($p^* = \frac{P\sigma^2}{\varepsilon}$) on a 112 particle system to check our results against those recently calculated using new molecular dynamics technique [C82]. It turned out that the potential energy, enthalpy, and area of the system were the same within 0.9% error. The grain boundary sliding and migration were observed at these temperatures, and a snapshot of the system at $T^* = 476$ is shown in Fig. 6.2. At the same temperatures and pressure the boundaries in a 56 particle system shows annihilation. To avoid thermally activated grain boundary motion in the 56 particle system the temperature was lowered to $T^* = .044$ at which point no grain boundary motion was observed.

6.3 Responses of Bicrystal to Uniaxial Loading

The mechanical responses of the 56 particles bicrystal under a uniaxial stress applied along the [010] direction were calculated. The load direction is normal to the grain boundary direction. The simulations were carried out at constant temperature of $T^* = 0.044$ so that thermal activation could not induce grain boundary sliding and migration at this low temperature (the melting temperature of the system is about $T^* \sim .64$ [C82]). In order to find out the grain boundary effects on the mechanical properties of the bicrystal, another "computer experiment" were carried out under the same conditions on a 28 particle perfect crystal system with the same

crystallographic orientation as the top crystal in the bicrystal system. Since the coordinate axes of the single crystal shown in Fig. 6.3 do not coincide with its principal axes, a uniform loading will produce a shear stress as well; in other words, the single crystal undergoes strains ε_{ij} given by:

$$\epsilon_{ij} = S_{ij22}\sigma_{22} \tag{6.1}$$

where the off diagonal elements of matrix S are not zero. It turned out that shear strain produced is negligible because, firstly the coordinate axes is close to the principal axes (less that 20° rotation along [001] direction) which causes the off diagonal elements of $\underline{S}$ to be small, and secondly the range of applied load from $\sigma^* = 1.6$ tension to $\sigma^* = 4.5$ compression is not wide enough to produce significant shear strain (beyond this range the grain boundaries started moving toward each other). Thus, from the macroscopic point of view the incompatibility caused by shear strain [H72] is not an important factor. The stress-strain curves for the bicrystal and the single crystal are shown in Fig. 6.4. The results show that the bicrystal suffers a larger deformation than the single crystal under the same load. From the snapshots of the particles in the bicrystal, qualitatively speaking it seems that the grain boundary region under the load has grown, for example see the system at the compression load of $\sigma^* = 4.5$ in Fig. 6.5. This expanded grain boundary is a rather disordered region relative to the bulk region and causes the region to become softer. Thus the overall strain of the bicrystal is larger because the bulk region response is the same as that of

the single crystal.

As it was mentioned above, beyond the range of applied stress shown in stress-strain curves in Fig. 6.4, the grain boundaries started moving and as the simulation proceeded they eventually were annihilated.

6.4 Responses of Bicrystal to Shear Loading

The behavior of the 56 particle bicrystal under shear stress was monitored by taking snapshots of the particles as the simulation proceeded. In order to avoid the rotation of the whole system the net torque applied on the system should be zero. This was achieved by applying symmetric shear stresses i.e, σ_{xy} and σ_{yx} had the same magnitude. At the low temperature of $T^* = 0.044$ and pressure of $P^* = 1.9744$ the shear stress was increased up to a critical shear stress of $\sigma^*_{xy} = \sigma^*_{yx} = 0.2$,no grain boundary motion was observed. Beyond this critical value the grain boundaries started moving by sliding and migration mechanism [B82],then as the simulation proceeded they annihilated and left behind a single crystal. Although the sliding and migration under shear loading has been suggested [B82], this is the first computer observation. In Fig. 6 the initial and a snapshot configuration of the system at shear stress of $\sigma^*_{xy} = \sigma^*_{yx} = 0.4$ are shown.

Fig. 6.1 Structure of the symmetric-tilt coincidence grain boundary with the reciprocal density of coincidence site $\Sigma=7$, (a) unrelaxed configuration (b) relaxed configuration. Circles with number are the particles and without number are 2 images of the particles in X direction.

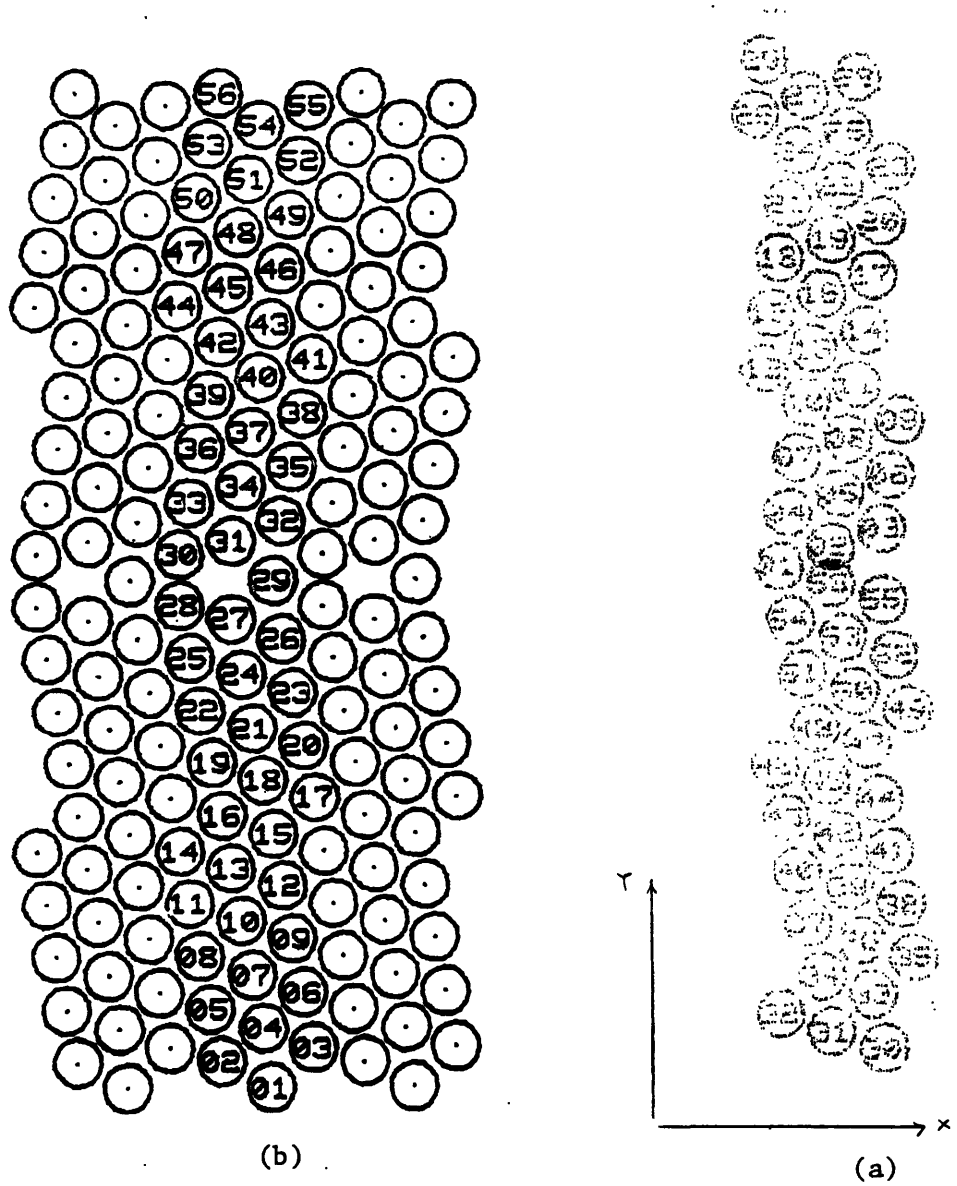

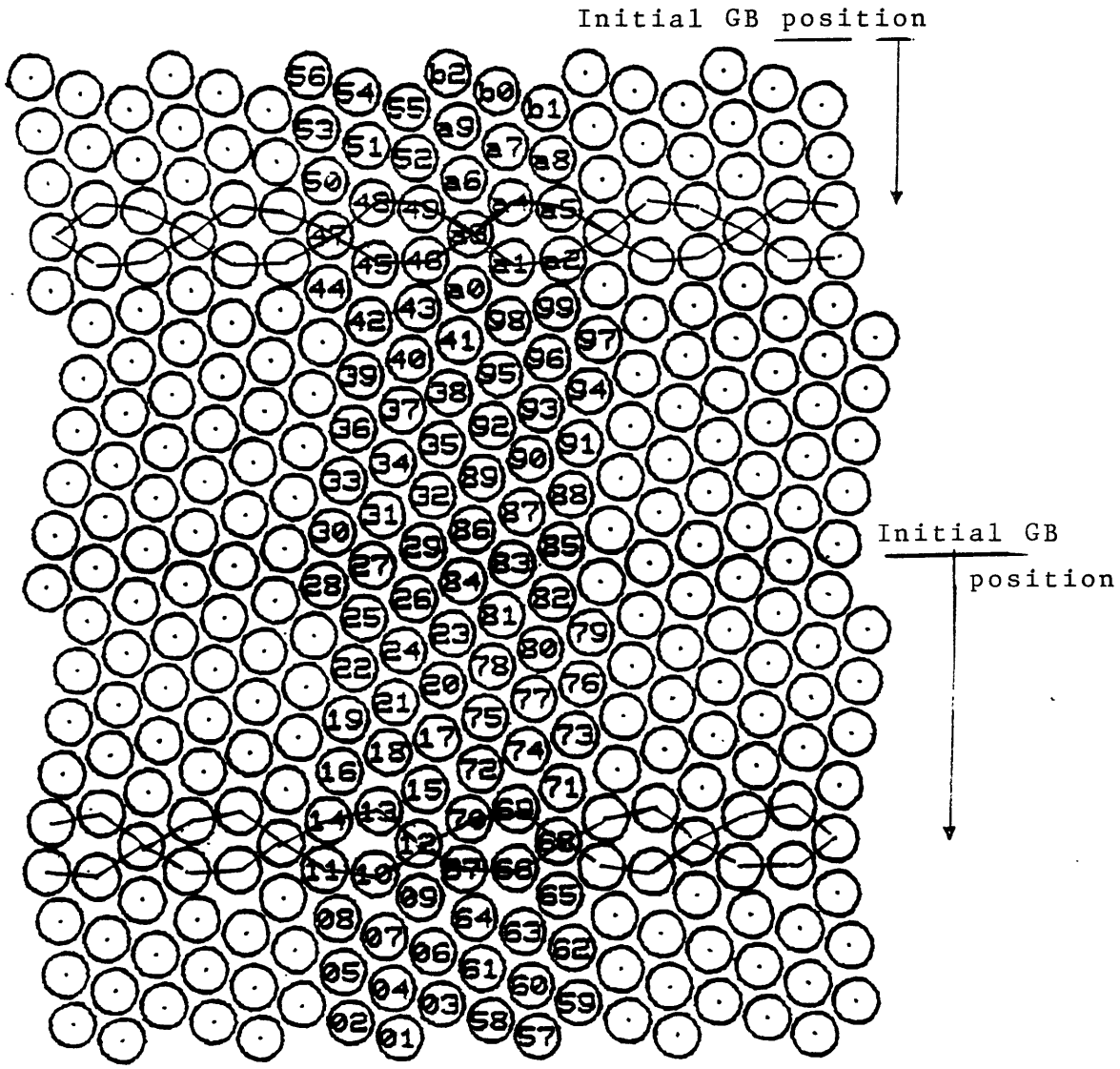

Fig. 6.2 Snapshot of the 112 particle bicrystal at T^{*}=0.496 and P^{*}=1.9744. The distances that the grain boudaries have moved are shown. The circles with numer indicate particle and without number are images.

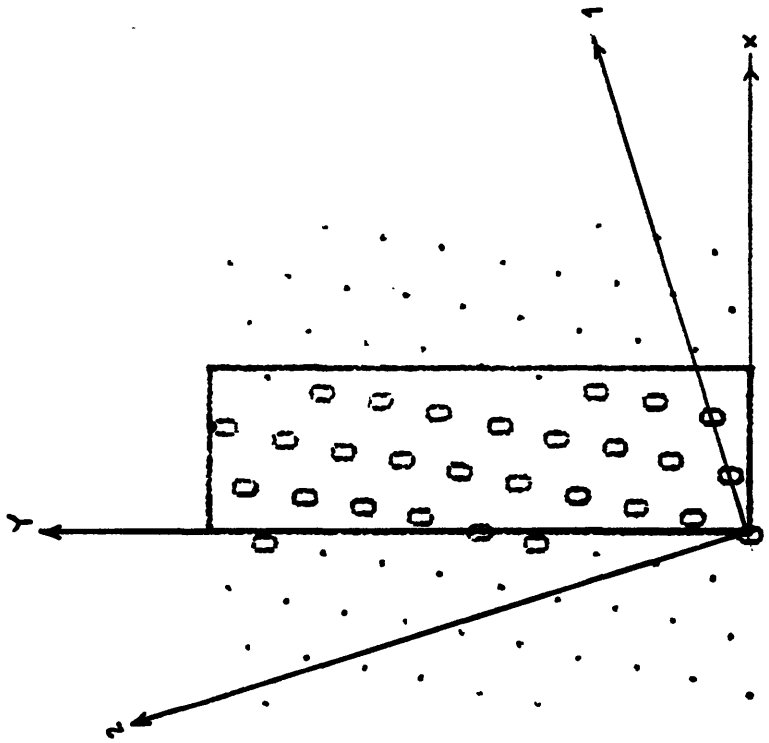

Fig. 6.3 The coordinate axes and one set of the principal axes of the single crystal are shown. O's indicate particles and .'s indicate their images in X direction.

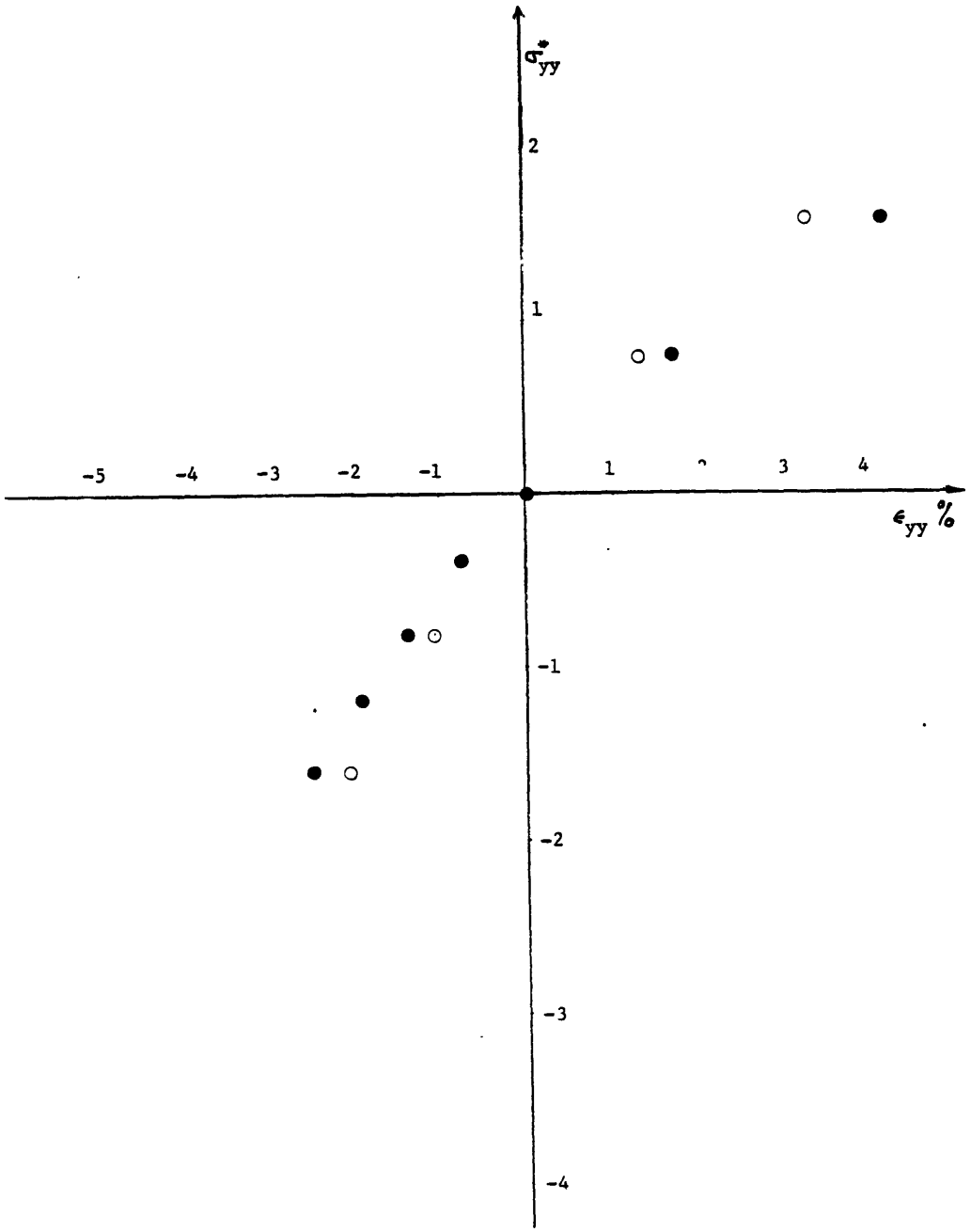

Fig. 6.4a Stress-strain curves of bicrystal and single crystal at T^*=.044. open circles are single crystal results and closed circles are bicrystal results.

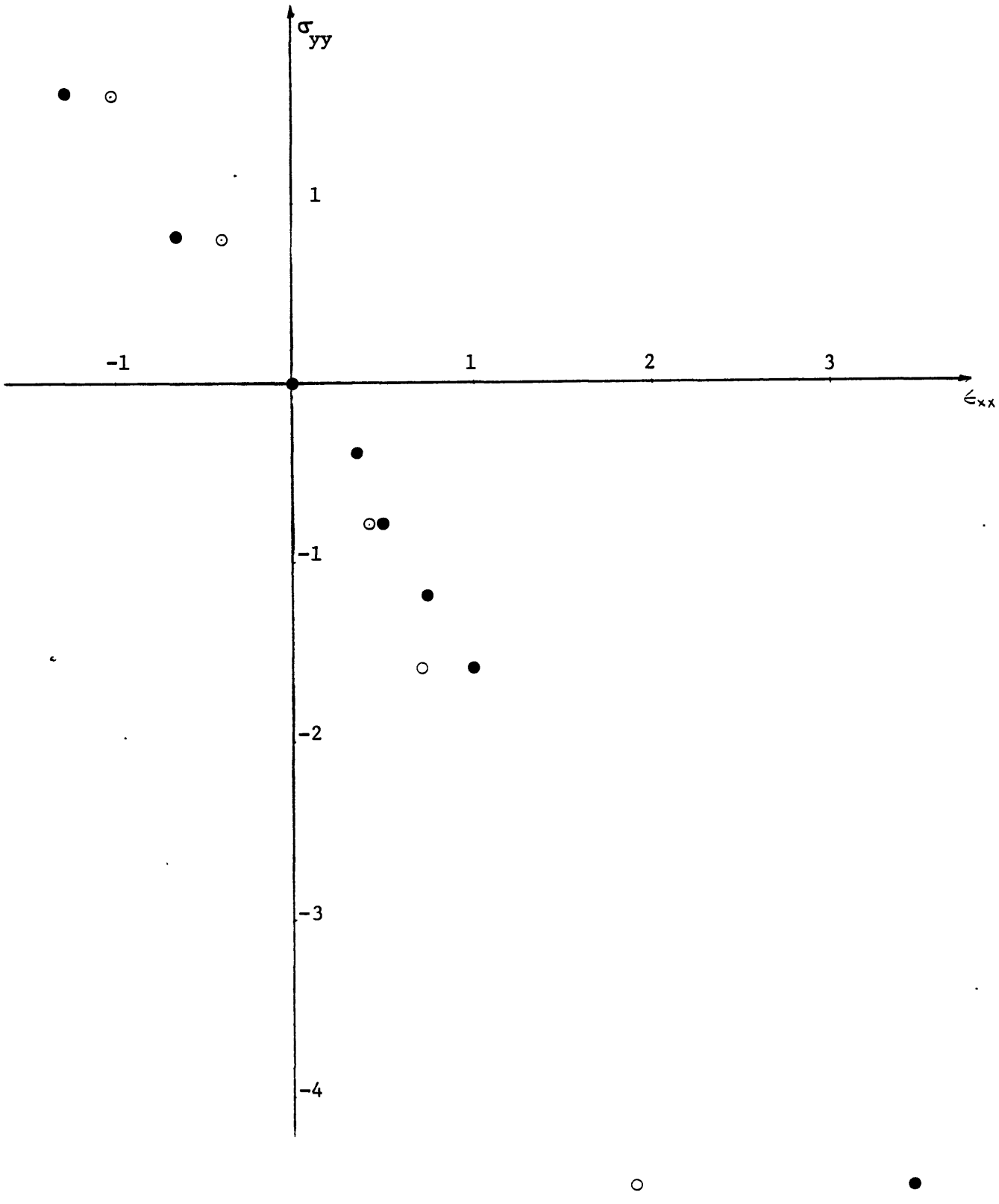

Fig. 6.4b Stress-strain curves of crystal and bicrystal.

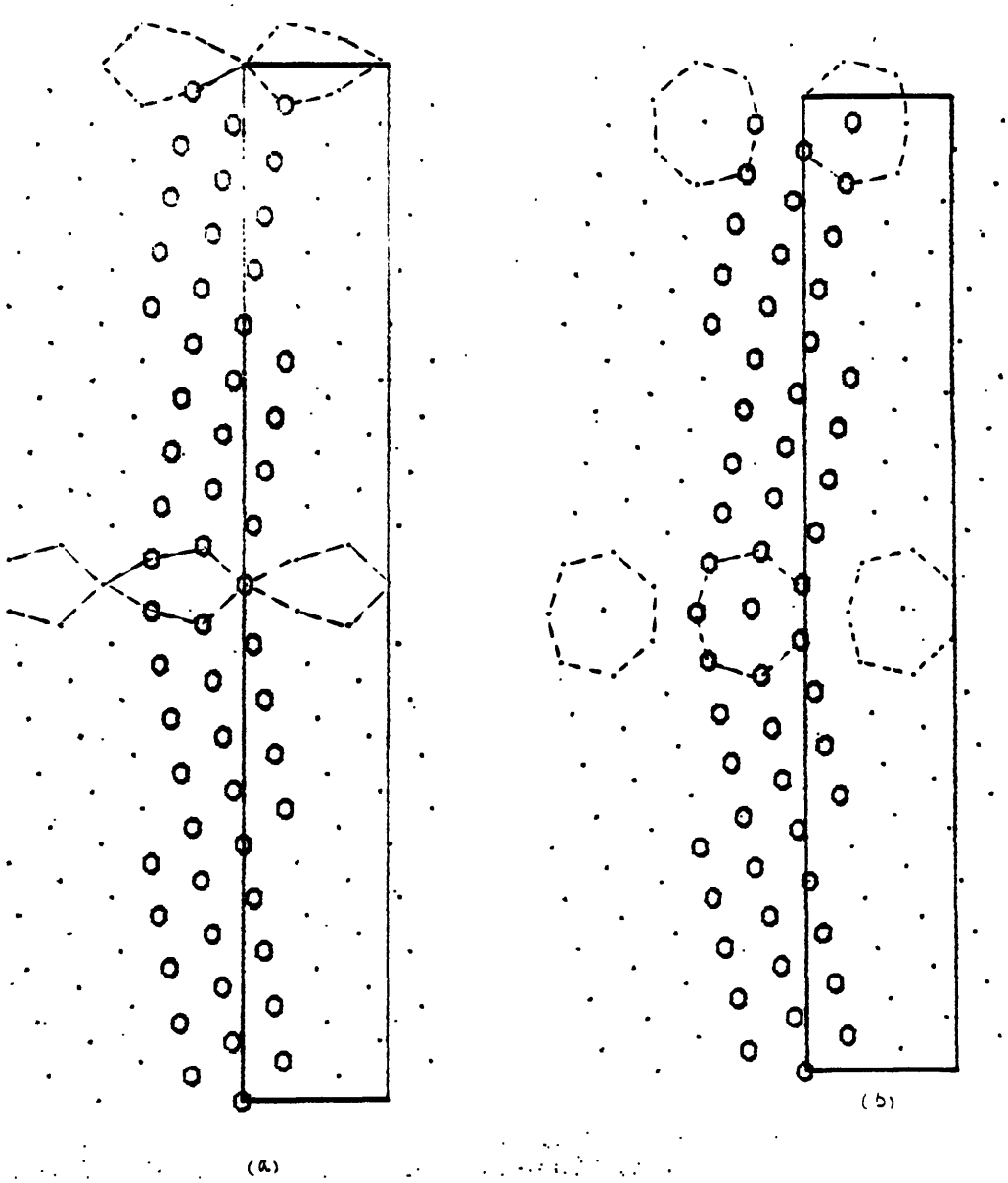

Fig. 6.5

Initial (a) and final (b) configuration of bicrystal at the compressive load of σ^*_{yy}=4.5. dashed lines show the grain boundary cores an solid lines show the dimensions of simulation cell. Open circles are partices and dots are their images in x direction.

Chapter 7

Grain Boundary-Point Defect Interactions

7.1 Introduction

It is well known that grain boundaries act as sources or sinks for point defects [B 79[a]]. Recently some attempts were made [B81[b], H81] to study the structure of vacancy in several grain boundary systems employing computer simulation techniques. In these studies it was found that the vacancy moves toward the grain boundary in order to lower the total energy of the system when it is introducted away from the boundary, but it remains localized at the boundary as a distinguishable missing atom in the grain boundary structure. In all of these studies either conventional periodic border conditions or a combination of periodic and fixed border conditions were used and were carried out at zero temperature. In the hard-sphere two-dimensional dynamic model [B8 0[b]] it was observed that the vacancy becomes delocalized, in contrast to being a distinguishable missing atom, after entering the boundary. This process was eventually followed by an annihilation process which restored the boundary to its original state and transferred the excess volume out to the model surface. Obviously in this case the border was free to have any shape and volume.

In this work we studied the behavior of impurities and vacancies in a two dimensional bicrystal system used in Chapter 6 using the improved MC method and the flexible periodic border condition. Our results clearly demonstrated that vacancies and impurities tend to go into the grain boundary when the temperature is high enough to initiate the movement. In all cases that vacancies or impurities

were absorbed by the grain boundary, it was the boundary that moved toward the defect. The vacancy results are similar to that found by hard-sphere dynamic model. Clearly, as it has been pointed out [B80^b], to have realistic results one should make the simulation cell bigger to include more grain boundary periods.

7.2 Impurities in Bicrystal

The atoms in the bicrystal were interacting through the Lennard-Jones potential with the parameters ε_a and σ_a of Argon given in Chapter 3. To study the behavior of impurities in the system one also needs to know the interaction potential between impurity and impurity (i-i) and between atom and impurity (a-i). In this study we assumed that (i-i) interaction also is described by the Lennard-Jones potential with the same parameter ε_i as that of (a-a)ε_a and the parameter σ_i different from the σ_a. The parameter σ_i is a representation of the size of the impurities.

The parameters of the Lennard-Jones potential describing interaction between atom and impurity using the Berthelot and Lorentz [M72] rules are:

$$\epsilon_{ia} = (\epsilon_i \cdot \epsilon_a)^{1/2} = (\epsilon \cdot \epsilon)^{1/2} = \epsilon \qquad (7.1)$$

and

$$\sigma_{ia} = \frac{1}{2}(\sigma_i + \sigma_a) \qquad (7.2)$$

Then, interaction potentials between different entities in the system are:

$$(a\text{-}a) \qquad v(r) = 4\epsilon\left[\left(\frac{\sigma_a}{r}\right)^{12} - \left(\frac{\sigma_a}{r}\right)^{6}\right] \qquad (7.3)$$

$$(i-i) \qquad V(r) = 4\epsilon\left[\left(\frac{\sigma_i}{r}\right)^{12} - \left(\frac{\sigma_i}{r}\right)^{6}\right] \tag{7.4}$$

$$(a-i) \qquad V(r) = 4\epsilon\left[\left(\frac{\sigma_{ia}}{r}\right)^{12} - \left(\frac{\sigma_{ia}}{r}\right)^{6}\right] \tag{7.5}$$

The scaling of pressure and temperature were done using ϵ and σ_a as in Chapter 6.

As it might be expected the size of the impurity atom introduced in the system is one of the important factors which controls the behavior of the impurity in the grain boundary system. In order to study effects of this factor we considered impurities with three different sizes, namely:

i) Impurities with twice the size of atoms in the bicrystal.

ii) Impurities with half the size of atoms in the bicrystal.

iii) Impurities with a size much smaller than the size of atoms in the bicrystal.

In the following we have reported our observations of the above three categories of impurity size. In all simulations the hydrostatic pressure was kept zero.

Case (i): At the temperature of $T^* = .044$ the particle "42" and "13" were replaced by the impurities of the size $\sigma_i = 2\sigma_a$, as is shown in Fig. 7.1.a. When the simulation started, the grain boundary structure was destroyed and the system was divided into different clusters as is shown in Fig. 7.1. This clustering effect might be an artifact of the highly dense 2-dimensional system being used. In the 3-dimensional system this may not happen because there is more free volume in 3-dimensional system than in the 2-dimensional system used here.

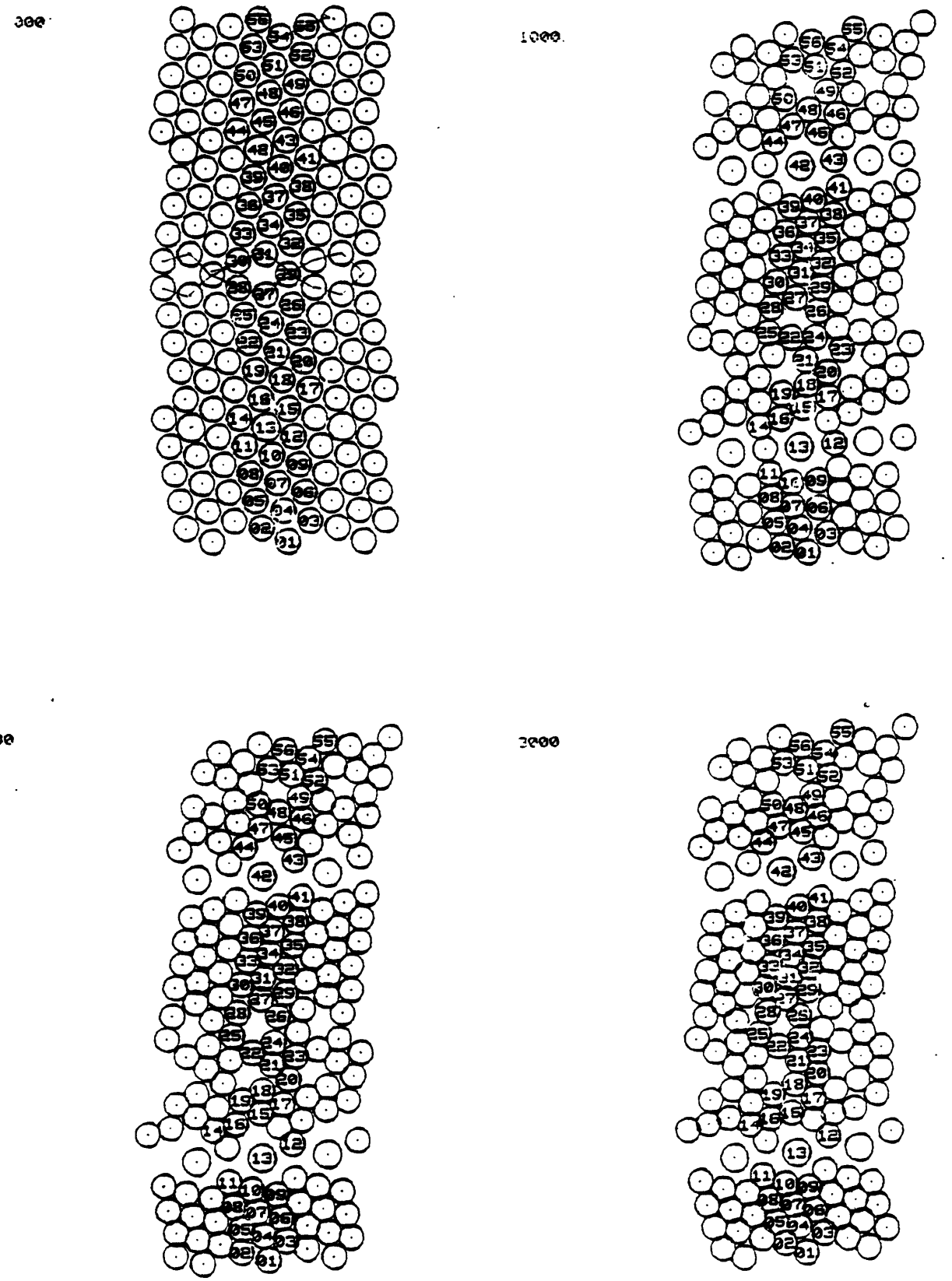

Fig. 7.1 Snapshots of the bicrystal with large impurities at sites #42 and #13 at 0,1000,2000,3000,4000 and 5000 step/particle (T^{*}=.044). Circles with numer are particles and without number their images in x direction.

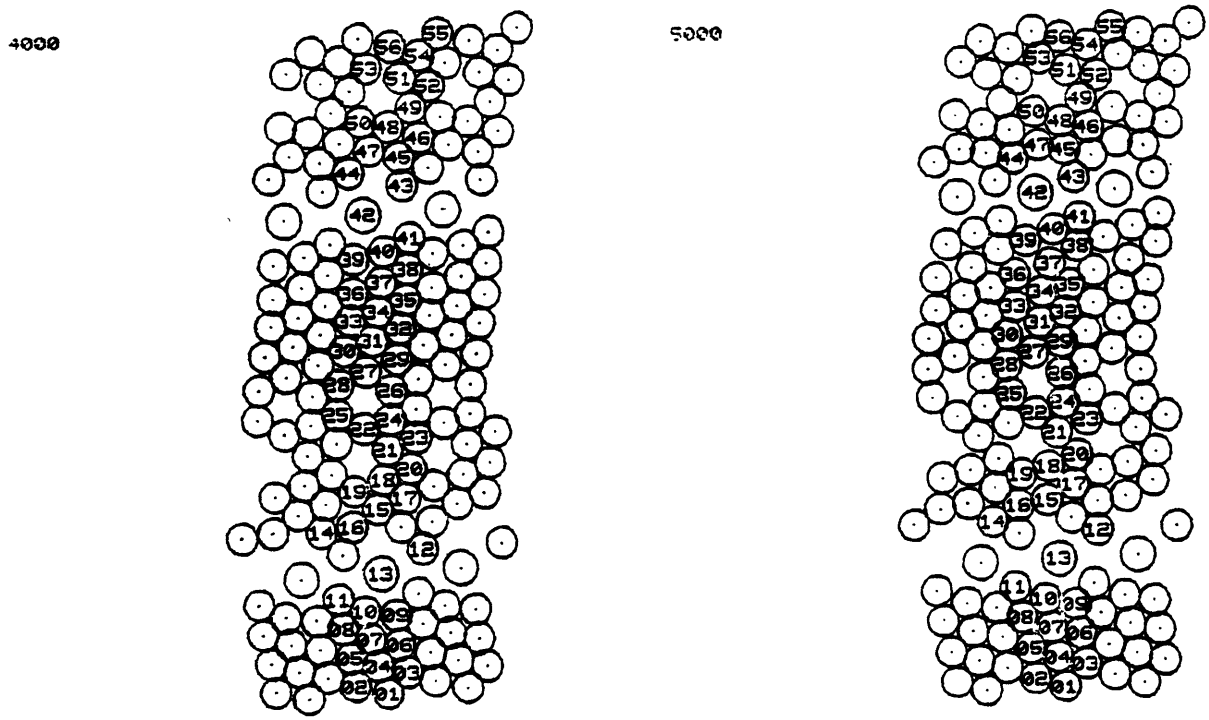

Fig. 7.1 (cont'd)

Case (ii): At the temperature of $T^* = .044$ the particles "42" and "13" were replaced by impurities with the size of $\sigma_i = \frac{1}{2}\sigma_a$, as it is shown in Fig. 7.2a. After 5000 steps/particles neither the impurities nor the boundaries moved. Then the temperature was raised to $T^* = 0.11$ and the simulation proceeded. At this temperature the grain boundaries started moving toward the impurities as shown by the snapshots in Fig. 7.2 and finally they absorbed the impurities and did not move any more. The absorption of the impurities changed the potential energy of the bicrystal from -158ε by 4.25%. Thus, this size of impurity could be absorbed by grain boundary when the temperature is high enough to initiate the grain boundary motion or possibly by putting impurities closer to grain boundaries.

Case (iii): At the temperature of $T^* = .044$ the particles "36" and "7" were replaced by impurities with the size of $\sigma_i = \frac{1}{10}\sigma_a$. Considering the cut off range used there would be no impurity-impurity interaction. The parameter $\sigma_{ai} = \frac{1.1}{2}\sigma_a$ would be $\frac{1}{2}\sigma_a$ when the size of the impurity goes to zero. Therefore any impurity size less than $\frac{1}{10}\sigma_a$ will have similar behavior as the impurities studied here. As the simulation started the impurities were absorbed by boundaries, as it is shown in Fig. 7.3. The absorption position of the impurities were next to the boundaries whereas in case (ii) they were inside the boundaries.

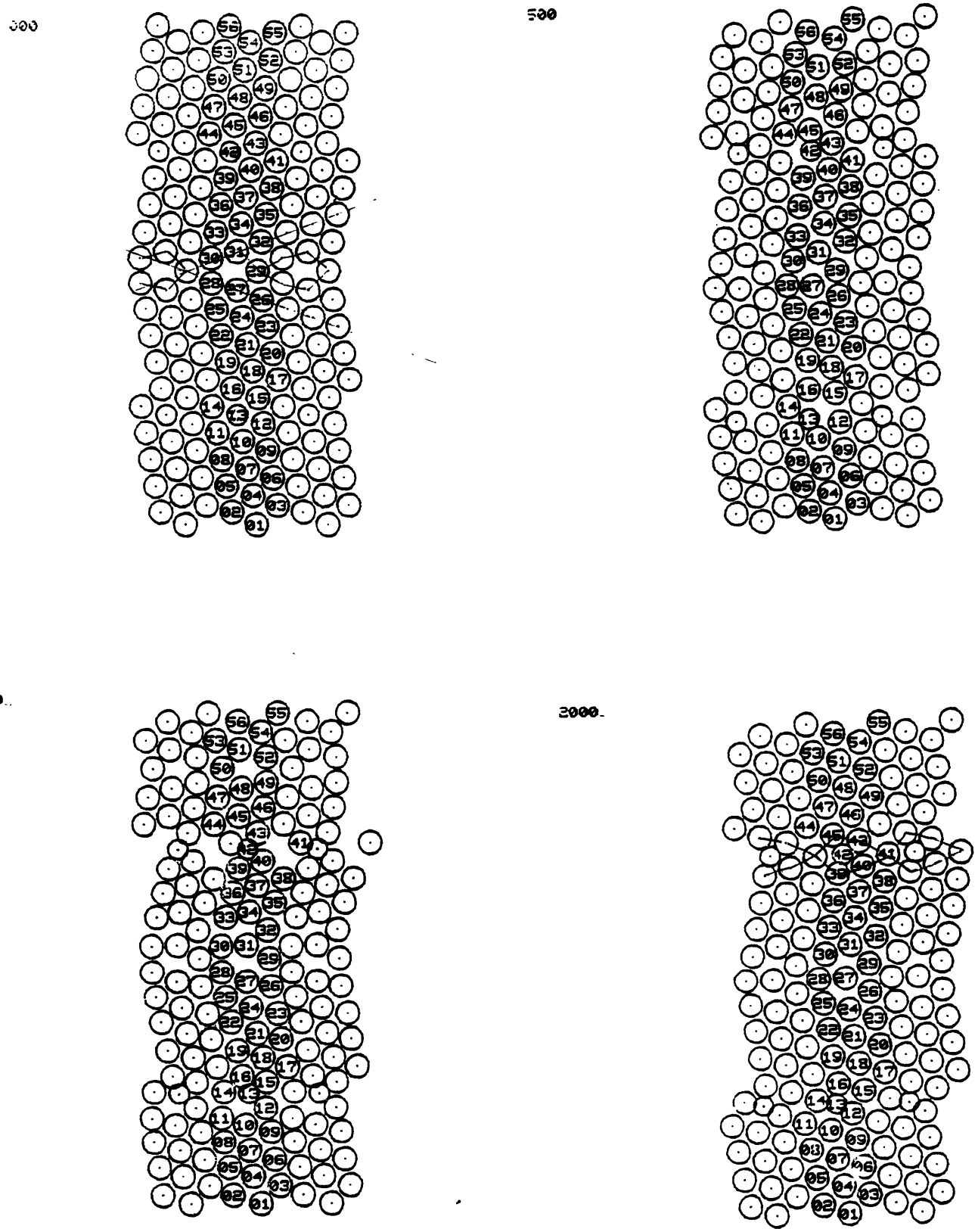

Fig. 7.2 Snapshots of the bicrystal with impurity half the size of host atom at 0,500,1000,2000,2500,3000,4000 and 5000 step/particle (T^{*}=.11). At 2000 step/particle impurity #42 and at 3000 step/particle impurity # 13 is absorbed by the grain boundaries.

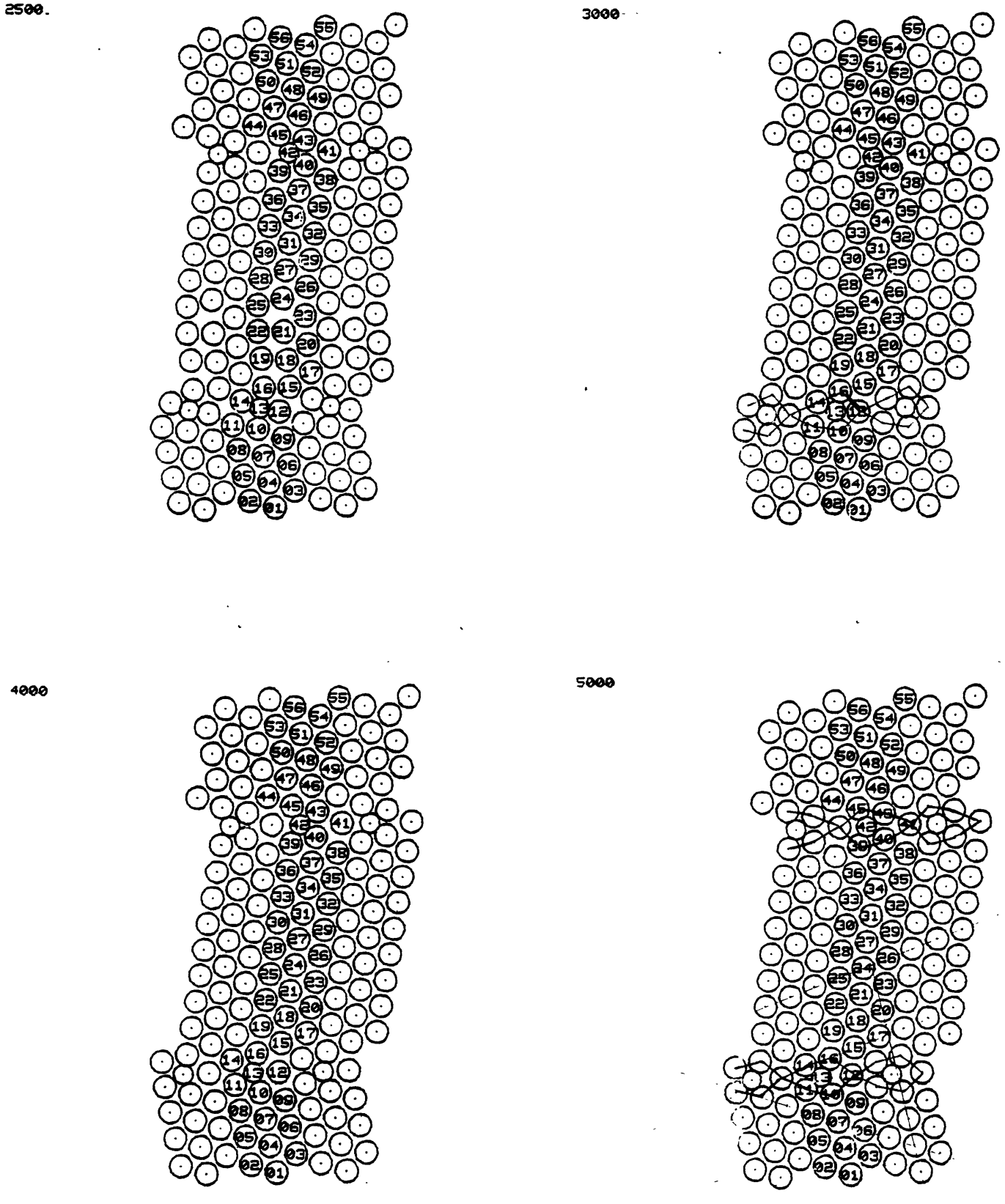

Fig. 7.2 (cont'd)

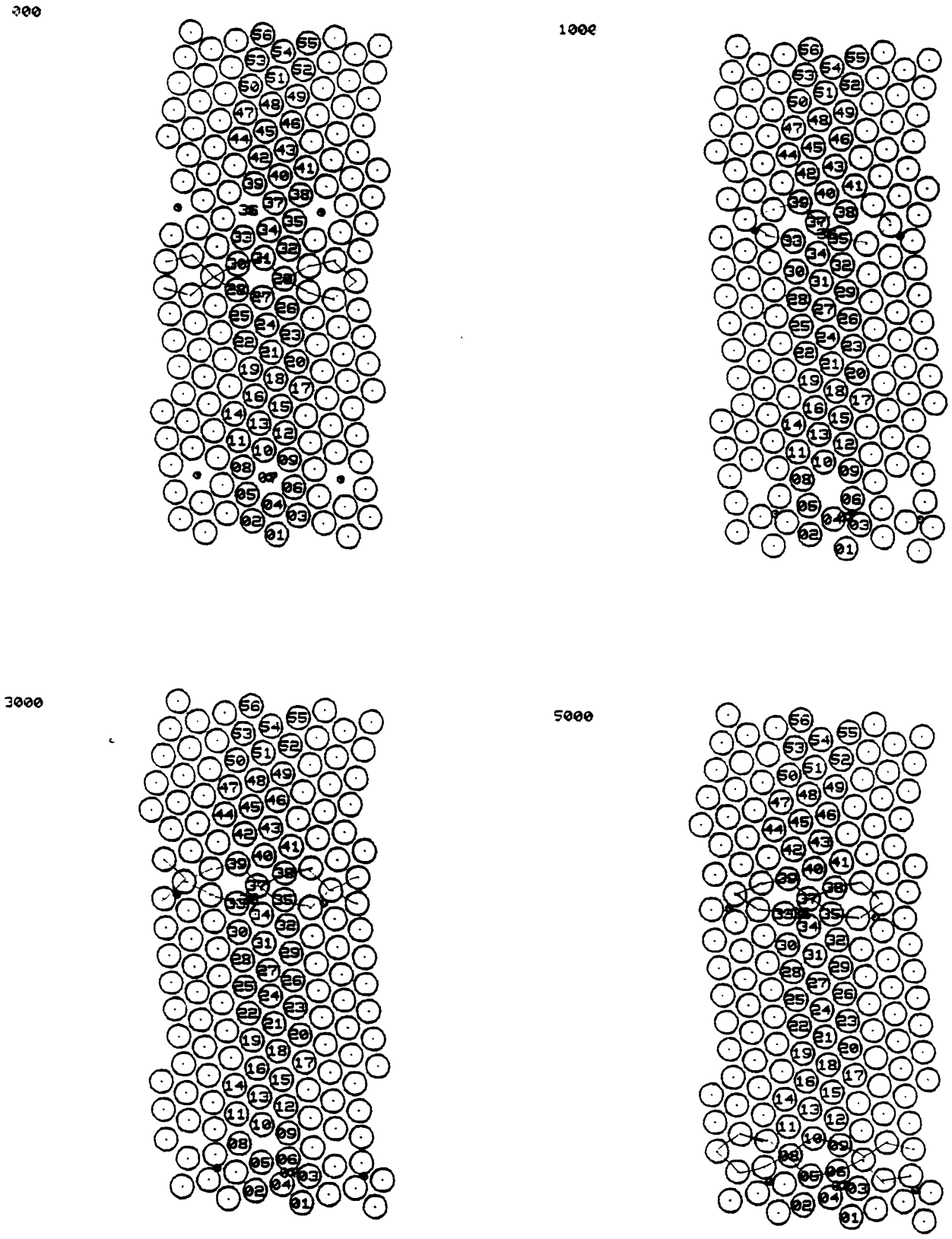

Fig. 7.3 Snapshots of the bicrystal with small impurities at site #36 and #7 at 0,1000,2000,3000 and 5000 step/particle (T^{*}=.044). At 1000 step/particle impurity #36 and at 3000 step/particle impurity #7 is absorbed by the grain boundaries.

7.3 Vacancy in Bicrystal

A vacancy was placed at three different locations in the 56 particle bicrystal to monitor its behavior and also to make an estimate of the range of interaction between the grain boundary and the vacancy. The following three simulations were carried out at the temperature of $T^* = .044$ and zero pressure:

i) The particle #36 was removed and the simulation was continued. After about 1000 steps/particle the grain boundary moved toward the vacancy and absorbed it. The initial and final configurations are shown in Fig. 7.4.

ii) The particles #37 was removed and the simulation was continued. After about 4000 steps/particle the grain boundary annihilated the vacancy, as it is shown in Fig. 7.5.

In the above two cases the excess free area was removed from the simulation cell by changing its dimensions and the grain boundary kept its kite shaped structure.

iii) The particle #38 was removed and the simulation was continued for 10,000 steps/particle and nothing was observed. Therefore at the temperature of $T^* = .044$ the interaction between vacancy and grain boundary was not enough to initiate the grain boundary movement. It seems not only the distance between the vacancy and the grain boundary is an important factor in the vacancy being absorbed but the vacancy site is also an important factor.

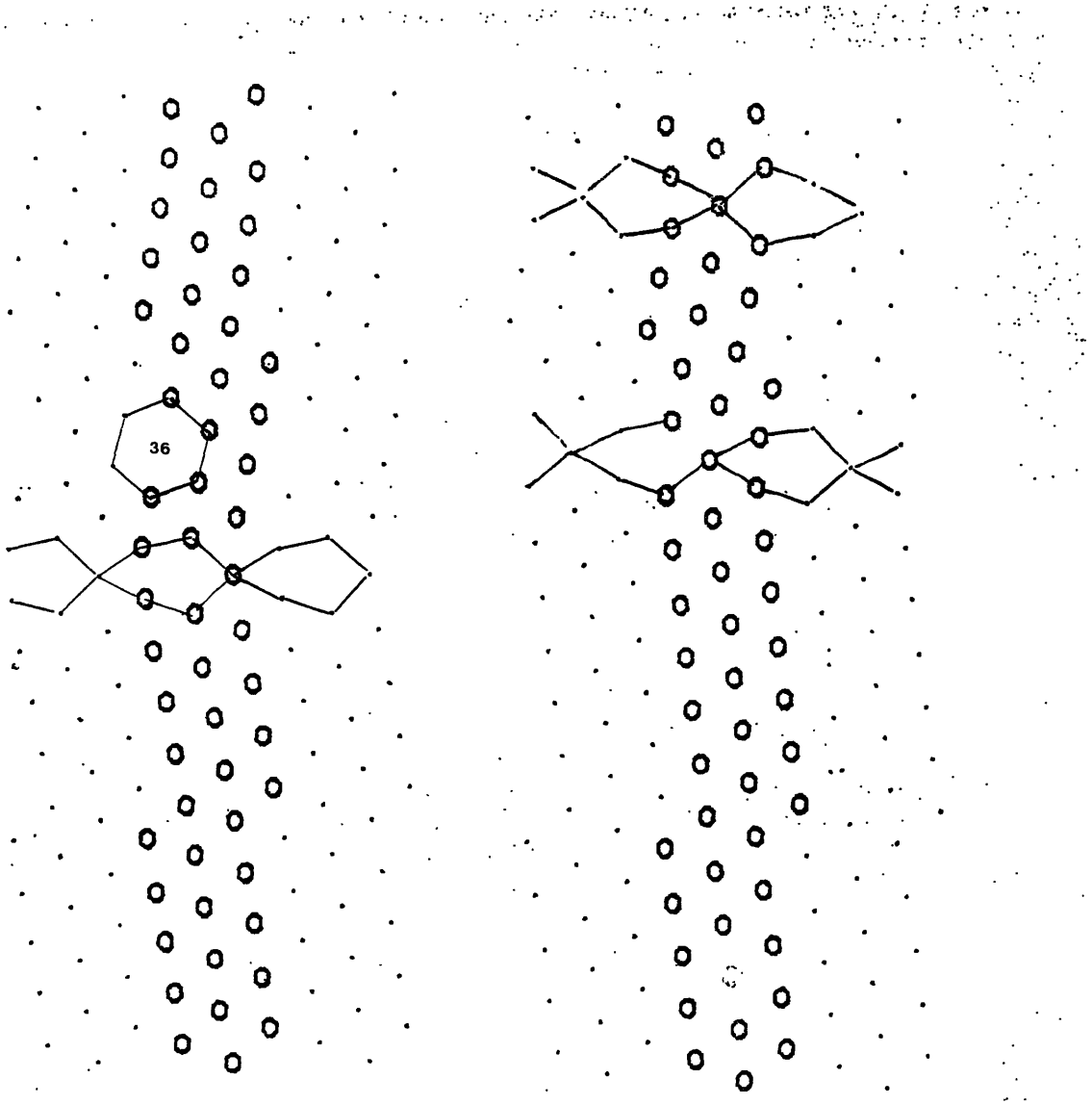

Fig. 7.4 Initial (a) and final (b) snapshots of the bicrystal with the vacancy at site # 36 for T^{*}=.044 . (b) shows vacancy annihilation by the grain boundary. Circles are particles and dots are their images in x direction.

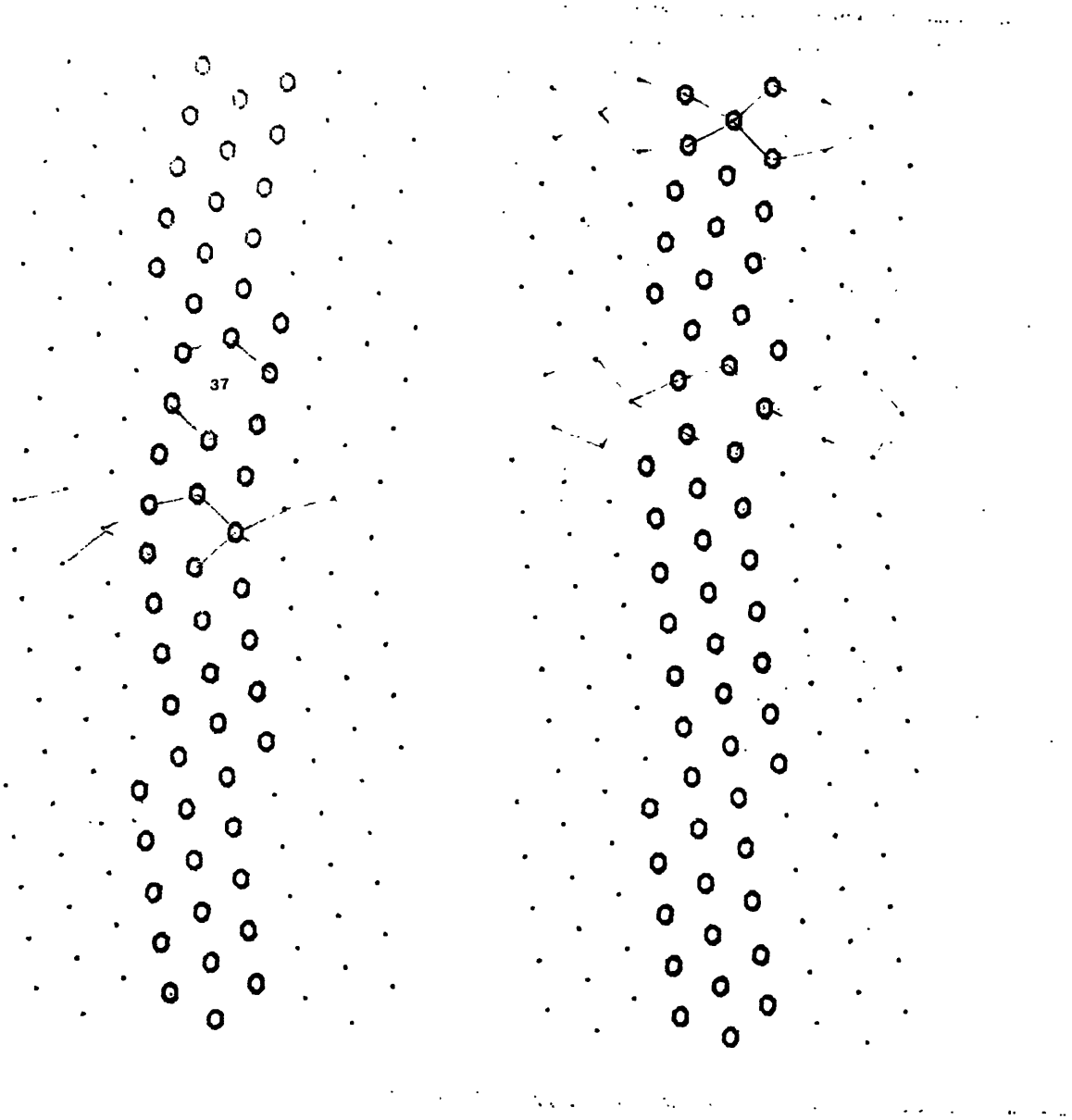

Fig. 7.5

Initial (a) and final (b) snapshots of the bicrystal with the vacancy at site # 37 for T^{*}=.044 . (b) shows vacancy annihilation by grain boundary. Circles are particles and dots are their images in x direction.

Chapter 8

Conclusions and Discussions

The Monte Carlo simulation technique has been improved so that it can be used to simulate a system of a finite number of particles which are interacting through a given pairwise potential at thermal and mechanical equilibrium with its surroundings in a general way. Previously the Monte Carlo technique could be used to simulate a system at thermal and hydrostatic pressure equilibrium only, whereas the improved method can be used to simulate a system under arbitrary externally applied stresses. The improved technique can be used to investigate many interesting phenomena which are induced either by externally applied stresses or by a combination of stresses and temperature. Such phenomena include : different structural transformations, theoretical strength calculation of materials at different temperatures, effects of defects on the mechanical responses of different systems.

The improved Monte Carlo technique is applied to a system of 32 particles which are interacting through the Lennard-Jones potential with the given parameters for argon [H64]. The stress-strain curve of the system at the temperature of 40°K (the melting temperature is about 110°K) for loads along the [001] direction is calculated. The comparison between the stress-strain curve at 40°K and the corresponding curve calculated by static method (0°K) and also the published static results [M 72b] suggests that the temperature effect is insignificant at low stresses (<100 bar) but becomes more pronounced as the stress increases beyond the value of 100 bar. Thus the static calculation is a good approximation to the stress-strain curve at low stresses and it will underestimate the strain

at high stresses for the system at finite temperatures.

At the temperature of 40°K the system fails under a tensile load of 600 bar applied along the [001] direction while the static calculation of theoretical tensile strength is about 2100 bar. The factor of 3.5 drop in the strength is mainly due to the thermal motion of particles. At the compressive load of 350 bar the deformed fcc structure is transformed to a deformed hcp structure where the [0001] axis of the hcp is along the [100] direction of the fcc structure. The transformation mechanism is a simultaneous large contraction in the [001] direction (load direction) and sliding of the adjacent (010) planes. This transformation can not be predicted by static method because it involves not only homogeneous deformation but also inhomogeneous particle displacement. The same transformation of fcc→hcp under compression has been also observed in the nickel system by the molecular dynamics method [P81]. Simulation results on a system with 108 particles reveal that the number dependence effect on the properties studied here is insignificant.

The stress-strain curves of α-iron are calculated using Morse [G53] and Johnson I [J64] potential to represent interatomic interaction by the static method. From the fact that the experimental tensile strength of whisker α-iron [B56b] is about $13*10^{10}$ dyn/cm^2 and the corresponding values of the static calculation are $1.2*10^{10}$ and $9*10^{10}$ for Morse and Johnson I potential respectively, one concludes that Johnson I potential is a more realistic one to be used to simulate mechanical property of α-iron. Still the Johnson I potential does not give the theoretical strength greater than the experimental

value that one would expect.

Martensitic transformations (bcc→fcc) and (fcc→bcc) are observed under stress at the relatively low temperature of 70°K (experimental melting temperature of α-iron is ∿ 1850°K) using the improved Monte Carlo technique. Such transformations were theoretically predicted [B24] and have been experimentally observed [Z65] when γ-iron is quenched. It is believed that Martensitic transformation [081] could occur through either a classical or a non-classical path. Martensitic transformations observed here are through the non-classical path. It is shown that at the tensile load of $6*10^{10}$ dyn/cm^2 the bcc→fcc transition occurs and at the compressive load of $5.5*10^{10}$ dyn/cm^2 the fcc→bcc transition occurs. It is also shown that at the critical loadings the parent structures become mechanically unstable. The simulated stress-strain curve at 70°K is in good agreement with static calculations.

More extensive simulation runs are needed to investigate the effect of temperature. It is also useful to carry out simulations using Johnson II potential because the Johnson I potential over-estimates the lattice constant in the fcc phase by 4.2% when the transformation takes place. This corresponds to an underestimation of the density in the fcc phase by 11.3%.

The mechanical properties of a two dimensional coincidence site lattice bicrystal with Σ=7 are investigated. The bicrystal is composed of 56 particles interacting through the Lennard-Jones potential. The stress-strain curve of the bicrystal is calculated when a load normal to the grain boundary plane (line) is applied. The comparison

between the calculated stress-strain curve and the corresponding curve for a single crystal with the same crystallographic orientation of the top component of the bicrystal shows that the effect of the grain boundary is to increase strain along the load direction. To our knowledge this is the first computer study of the grain boundary effect on the stress-strain curve of a bicrystal. Further studies could be carried out on a 3-dimensional system using a realistic potential to investigate the effects under different loading conditions.

Grain boundary sliding and migration under shear loading is observed in the bicrystal when the shear stress exceeded the critical valud of σ^*_{xy} = .2 (dimensionless unit) at the reduced temperature of T^*=0.044. The critical shear should vary with the grain boundary surface (length); additional simulations using a larger system are needed to find out this grain boundary surface dependence.

In this thesis we have also explored behavior of impurity atoms and vacancies in the bicrystal. It is demonstrated that small impurity atoms will be absorbed by the grain boundary if the temperature is high enough to initiate grain boundary motion. An impurity atom twice the host particle size appears to cause clustering. This behavior may be an artifact of the two dimensional bicrystal used, because the system is highly densed and also the simulation cell is rather thin. This may not occur in a three dimensional system. The absorption of impurity atoms by the grain boundary is a first step to understand the segregation phenomenon in materials because the grain boundaries are sources and sinks of defects. Further studies are needed to establish the defect-grain boundary interaction by correlating the

relative position of the defect with respect to the grain boundary and the potential energy of the bicrystal.

REFERENCES:

A80 Abraham, F.F., Phys. Rev. Lett., 44, 463 (1980).

A75 Anderson, M.S. and Swenson, C.A., J. Phys. Chem. Solids, 36, 145 (1975).

B24 Bain, E.C., Trans. Amer. Inst. Min. (Metall.) Engrs., 70, 25 (1924).

B79[a] Baluffi, R.W., ASM Seminar on Interfacial Segregation, p193, Johnson, W.C. and Blakely, J.M., eds. (1979).

B76[a] Barker, J.A. in Rare Gas Solids, Chap. 4, Klein, M.L. and Venables, J.A., eds. Academic Press (1976).

B81[a] Barker, J.A., Henderson, D. and Abraham, F.F., Physica 106A, 226 (1981).

B73 Barker, J.A. and Klein, M.L., Phys. Rev. B, 7, 4707 (1973).

B71 Barker, J.A., Fisher, R.A. and Watts, R.O., Mol. Phys., 21, 657 (1971).

B76 Bennett, C.H., J. Comp. Phys., 22, 245 (1976).

B56[a] Bilby, B.A. and Christain, J.W., The Mechanism of Phase Transformations in Metals, Institute of Metals, London (1956).

B80[a] Binder, K., Phys. Rev. Lett., 45, 811 (1980).

B79[b] Binder, K. ed. Monte Carlo Methods in Statistical Physics (Springer, Berlin-Heidelberg-New York, 1979).

B76[c] Binder, K., in Phase Transition and Critical Phenomena, vol. 5B (Domb and Green, ds.),(1976).

B65 Biot, M.A., Mechanics of Incremental Deformations ,John Wily(1965)

B82[a] Bishop, G.H., et al, J. Appl. Phys., 53, 5596 (1982).

B82[b] Bishop, G.H., et al, J. Appl. Phys. 53,5609 (1982).

B54 Born, M. and Huang, K., Dynamical Theory of Crystal Lattice, Oxford University Press, 1954.

B56[b] Brenner, S.S., J. Appl. Phys. 27, 1484 (1956).

B80[b] Bristowe, P.D., et al, Scripta Met., 14, 943 (1980).

B81[b] Brokman, A., Bristowe, P.D. and Balluffi, R.W., J. Appl. Phys., 52, 6116 (1981).

C82 Carrion, F.J., M.S. Thesis, MIT (1982).

C81 Chang, H.K., Lee, J.K. and Stein, D.F.

C80 Chang, R., Scripta Met., 14, 779 (1980).

C65 Christain, J.W., The Theory of Transformations in Metals and Alloys, (Pergamon Press) 1965.

C64 Clark, M. and Hansen, K.F., Numerical Method of Reactor Analysis, Chap. 6, Academic Press (1964).

D75 Deutsch, O.L, Ph.D. Thesis, MIT (1975).

D53 Doob, J.L., Stochastic Processes, Wiley, N.Y., p. 221 (1953).

F72 Fisher, R.A. and Watts, R.O., Mol. Phys. 22, 1051 (1972).

G53 Girifalco, L.A. and Weizer, V.G., J. Phys. Chem. Solids, 12, 260 (1953).

H81 Hahn, W. and Gleiter, H., Acta Met., 29, 601 (1981).

H69 Hansen, J.P. and Verlet, L., Phys. Rev. 184, 151 (1969).

H76 Harrison, R.J., Bruggeman, G.A. and Bishop, G.H., Grain Boundary Structure and Properties, Chadwick, G.A. and Smith, D.A., eds, (Academic Press, London) (1976).

H52 Hildebrand, F.B., Methods of Applied Mathematics (Prentice-Hall, Englewood Cliffs) (1952).

H77 Hill, R. and Milstein, F., Phys. Rev. B, 15, 3087 (1977).

H56 Hill, T.L., Statistical Mechanics, McGraw-Hill, Inc. (1956).

H64 Hirshfelder, J.O., Curtiss, C.F. and Bird, R.B., Molecular Theory of Gases and Liquids (John Wiley, 1964).

H72 Hirth, J.P., Met. Trans., 3, 3047 (1972).

H70 Holt, A.C., Hoover, W.G. and Shortle, D.R., Physica 49, 61 (1970).

J80 Jacucci, G. and Ronchetti, M., Sol. State Comm., 33, 35 (1980).

J70 Johannesson, T. and Tholen, A., Phil. Mag., 21, 1223 (1970).

J64 Johnson, R.A., Phys. Rev., 134, A1329 (1964).

K78 Kwok, T.Y., M.S. Thesis, MIT (1978).

L59 Landau, L.D. and Lifshitz, E.M., Theory of Elasticity, (Pergamon, Oxford), (1959).

L80 Lee, C.Y. and Scott, H.L, J. Chem. Phys., 73, 4591 (1980).

L77 Lee, T.D. and Margolin, H., Scripta Met., 11, 713 (1977).

L61 Leibfried, G. and Ludwig, Solid State Physics, Vol. 12, 307 (1961).

L74 Lewis, W.F., et al, J. Phys. Chem. Solids, 35, 383 (1974).

L61 Lyman, T., ed., Metals Handbook, vol. 1, 8th Ed., American Society for Metals (1961).

M72[a] McDonald, I.R., Mol. Phys., 23, 41 (1972).

M72[b] Macmillan, N.H. and Kelly, A., Proc. R. Soc. Lond., A330, 291 (1972).

M72[c] Macmillan, N.H. and Kelly, A., Proc. R. Soc. London, A330, 309, (1972).

M53 Metropolis, N., et al, J. Chem. Phys., 21, 1087 (1953).

M25 Milne, E.A., Phil. Mag., 50, 409 (1925).

M80 Milstein, F. and Farber, B., Phys. Rev. Lett., 44, 277 (1980).

M71 Milstein, F., Phys. Rev. B. 3, 1130 (1971).

N82 Nakanishi, K., et al, J. Chem. Phys., 76, 629 (1982).

O82 Olson, G.B. and Cohen, M., Proc. Intl. Conf., Martensitic Transformations, ICOMAT82, Leuven, Belgium, 1982.

O81 Olson, G.B. and Cohen, M., Proc. Intl. Conf., Solid-Solid Phase Transformations, Cambridge (1981).

P75 Pande, C.S. and Chon, Y.T., in Treatise on Materials Science and Technology, vol. 8, Herman, H., ed. (1975).

P81 Parrinello, M. and Rahman, A., J. Appl. Phys. 52, 7182 (1981).

P65 Peterson, O.G., Batchelder, D.N. and Simmons, R.O., Phil. Mag. 12, 1193 (1965).

P80 Phani, M.K., Lebowitz, J.L. and Kalos, M.H., Phys. Rev. B, 21, 4027 (1980).

P76 Pollock, E.L., J. Phys. C: Solid State Phys., 9, 1129 (1976).

R74 Raveche, H.J., Mountain, R.D. and Streett, W.B., J. Chem. Phys., 61 1970 (1974).

S69[a] Squire, D.R. and Hoover, W.G., J. Chem. Phys., 50, 701 (1969).

S69[b] Squire, D.R., Holt, A.C. and Hoover, W.G., Physica 42, 388 (1969).

T82 Tobochnik, J. and Chester, G.V., Phys. Rev. B, 25, 6778 (1982).

T77[a] Torrie, G.M. and Valleau, J.P. , J. Chem. Phys., 66, 1402 (1977).

T77[b] Torrie, G.M. and Valleau, J.P., J. Comp. Phys., 23, 187 (1977).

T78 Toxvaerd, S., J. Chem. Phys., 69, 4750 (1978).

V77 Valleau, J.P. and Whittington, S.G. in Statistical Mechanics A, Berne, B.J., ed. (Plenum Press) (1977).

V80 Vitek, V., et al, Grain Boundary Structure and Kinetics, Balluffi, R.W., ed., ASM, Cleveland, Ohio (1980).

W71 Weins, M.J., Gleiter, H. and Chalmers, B., J. Appl. Phys., 42, 2639 (1971).

W76 Wood, W.W. and Erpenbeck, J.J., Ann. Rev. Phys. Chem. (1976).

W68 Wood, W.W. in Physics of Simple Liquids (H.N.V. Temperly, J.S. Rowlinson, and G.S. Rushbrooke, eds.) North-Holland, Amsterdam, 1968, Ch. 5.

Z65 Zerwekh, R.P. and Wayman, C.M., Acta Met., 13, 99 (1965).

Z79 Zubov, V.I. , Izvestiya Vyyshikh Uchebnykh Zavedeni(Trans.) no.3 ,275(1979).